Density functional theory study of (110) β-MnO_2, β-TiO_2 and β-VO_2 surface in metal-air batteries

by

KHOMOTSO PORTIA MAENETJA

THESIS

Submitted in fulfilment of the requirements for the degree of

DOCTOR OF PHILOSOPHY (PhD)

in

Physics

in the

FACULTY OF SCIENCES & AGRICULTURE

(School of Physical & Mineral Sciences)

at the

UNIVERSITY OF LIMPOPO

SUPERVISOR: Prof. P.E. Ngoepe

2017

ABSTRACT

Density functional theory (DFT) study is employed in order to investigate the surfaces of, β-MnO_2, β-TiO_2 and β-VO_2 (β-MO_2) which act as catalysts in Li/Na-air batteries. Adsorption and co-adsorption of metal (Li/Na) and oxygen on (110) β-MO_2 surface is investigated, which is important in the discharging and charging of Li/Na–air batteries. Due of the size of the supercell, and assuming that oxygen atoms occupy bulk-like positions around the surface metal atoms, only five values of (gamma) Γ are possible if constraint to a maximum of 1 monolayer (ML) of adatoms or vacancies: Γ= 0 surface is the stoichiometric surface, Γ= 1, 2 are the partially and totally oxidised surfaces, and Γ=-1, -2 are the partially and totally reduced surfaces. The manganyl, titanyl and vanadyl terminated surface is not the only surface that can be formed with Γ= +2. Oxygen can be adsorbed also as peroxo species $(O_2)^{2-}$, with less electron transfer from the surface vanadium atoms to the adatoms than in the case of manganyl and titanyl formation. The redox properties of the (110) surfaces are investigated by calculating the relative surface free energies of the non-stoichiometric compositions as a function of oxygen chemical potential. Increasing the temperature and lowering the pressure (i.e. more reducing conditions) we find the stoichiometric surface reduces first partially and then entirely at higher temperatures. The lithium orientation between two bridging oxygen and in-plane oxygen (bbi) orientation is much more stable for the three metal oxides, thus lithium generally prefers to adsorb where it will be triply coordinated to two bridging oxygens and one in-plane oxygen atom. However, sodium prefers to orientate itself on the bridging oxygen on the surface, but a triple coordination on sodium is also favourable. Oxygen adsorption on Li/MO_2 was simulated and it was found that in all

the metal oxides (MnO_2, TiO_2 and VO_2) the most stable orientation is the dissociated composition where there is an oxygen atom on the “bulk-like” positions on top of each of the M cations. The surface lithium peroxide for MO_2 simulated produces clusters with oxygen - oxygen bond lengths that are comparable to the calculated bulk and monomer discharge products reported in literature. Adsorption of oxygen on Na/MO_2 was investigated and it was observed that the catalysts used encourage formation of the discharge product reported in literature, i.e. NaO_2. The surface NaO_2 appears to have comparable bond lengths to the calculated bulk and monomer NaO_2.

DECLARATION

I declare that the thesis hereby submitted to the University of Limpopo for the degree of Doctor of Philosophy in Physics has not been previously submitted by me for a degree at this or any other university; that it is my work in design and execution, and that all material contained therein has been duly acknowledged.

Khomotso Portia Maenetja

Date:

ACKNOWLEDGMENTS

I express my sincere gratitude to my advisor, supervisor and mentor, Prof P. E. Ngoepe for constantly giving me support and excellent supervision.

I wish to thank Dr T. Mellan and Dr R. Grau-Crespo for their contributions especially on redox properties of MnO_2; Li and O adsorption and co-adsorption on (110) MnO_2 surface respectively.

I wish to acknowledge National Research Foundation, South African Research Chair Initiative of the Department of Science Technology and Department of Energy storage Programme for financial assistance. Many thanks go to Prof C.R. A. Catlow for hosting me during my visit at University College London in the United Kingdom, London. I also extend my gratitude to Dr S. M. Woodley for the technical support and the time he provided in order to run my calculations on HECToR, the UK's national high performance computing service. I acknowledge the Materials Modelling Centre (MMC) and Center for High Performance Computing (CHPC) for computing resources.

I also want to thank members of the Materials Modelling Centre for their contribution. The support of Mamogo Masenya, it goes beyond words because it has been constant. In the book of Phillipians 4:13, the bible says that I can do all things through Christ who strengthens me, thus, It is not by power nor by might but by the spirit of the Lord, I therefore, above all, give thanks to God.

DEDICATION

This work is dedicated to:

My Son

Thato

My Parents

Jan and Queen

My Siblings

Milos, Kholofelo, Katlego, Khutso and Thabang.

Table of Contents

List of Figure

List of Tables

Chapter 1: Introduction

1.1 Rationale

A high energy demand as a result of a growth in living standards and population has stimulated the efforts to develop high energy density power sources. Even though there have been improvements in Li-ion battery technology developments, this developments have not kept pace with the development of portable devices, leaving a so-called “power gap” that is broadly anticipated to grow in coming years. Nevertheless, even when fully developed, the highest energy densities Li-ion batteries are unable to deliver sufficient energy to meet the demands. In this regard, reaching beyond Li-ion batteries appears to be an alarming challenge which requires the exploration of new technologies of storing energy which is more robust than the Li-ion batteries.

As an alternative, metal air batteries are gaining a lot attention due to their ability to deliver high theoretical specific energies, which are almost 6–10 times Li-ion batteries [1-3]. In particular, the lithium air battery use free oxygen from the air and react with lithium ions on the surface of the air electrode, which is less heavy than cathodes used in Li-ion batteries.

However, the fundamental challenge that limits the use of Li/Na air battery technology is the ability to find a catalyst that will catalyse the formation and decomposition of Li_2O_2 during charging and discharging cycle i.e. oxygen reduction reaction (ORR) and oxygen evolution reaction (OER).

1.2 Structural aspects

Bulk structure is a primitive tetragonal with space group $P4_2/mnm$ [2]; it is characterized by an octahedrally coordinated M atom. As shown in figure 1.3 the three metal oxides are isostructural, therefore, the co-ordinates shown in table 1.2 represents all three metal oxide atom coordinates. The distance between atoms in figure 1.3 also applies for MnO_2, TiO_2 and VO_2 which is shown in table 1.3 below.

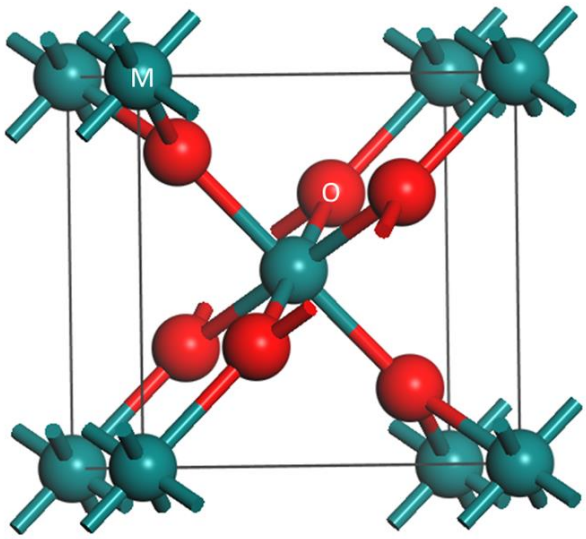

Figure 1.1: Primitive tetragonal structure for rutile MO_2, with green spheres representing the metal atom (Mn, Ti and/or V) and red spheres representing the oxygen atom

Table 1.1: Lattice parameters of the MnO_2, TiO_2 and VO_2 bulk structure

Structure	a (Å)		c (Å)		V (Å^3)
β-MnO_2	4.366	4.410 [4]	2.961	2.887 [5]	56.44
β-TiO_2	4.627	4.954 [6]	3.008	2.959 [4]	64.40
β-VO_2	4.617	4.554 [4]	2.774	2.857 [5]	59.13

Table 1.2: Atoms existing in the bulk structure for the metal oxides with positions of atoms.

MnO_2		TiO_2		VO_2	
Atoms	Distance	Atoms	Distance	Atoms	Distance
Mn-O	1.8834	Ti-O	1.9553	V-O	1.9007
Mn-O	1.8834	Ti-O	1.9553	V-O	1.9621
Mn-O	1.8933	Ti-O	1.9823	O-O	2.5133
Mn-O	1.8933	Ti-O	1.9823	O-O	2.7318
Mn-Mn	2.8873	Ti-Ti	2.9635	O-O	2.8520
Mn-O	3.3304	Ti-O	3.4989	O-O	3.2951
Mn-Mn	3.4224	Ti-O	3.4989	V-O	3.4554
Mn-O	3.4527	Ti-O	3.5654	V-O	3.4617
Mn-O	3.4527	Ti-O	3.5654	O-O	3.8014
Mn-O	3.9112	Ti-Ti	3.5792	O-O	3.9242

Table 1.3: Coordinates of atoms in the bulk structure for the metal oxides (rutile MnO_2, TiO_2 and VO_2)

Site	Wyckoff position	Element	X	Y	Z	Occupancy
MnO_2						
Mn1	2a	Mn	0.00000	0.00000	0.00000	1.0
O1	4f	O	0.30200	0.30200	0.00000	1.0
TiO_2						
Ti1	2a	Ti	0.00000	0.00000	0.00000	1.0
O1	4f	O	0.30540	0.30540	0.00000	1.0
VO_2						
V1	2a	V	0.00000	0.00000	0.00000	1.0
O1	4f	O	0.30479	0.30479	0.00000	1.0

The lattice parameters shown in table 1.2 are for the relaxed bulk structures and those with references are the experimental lattice parameters.

1.3 Literature review

1.3.1 Structural properties

Pyrolusite and ramsdellite are known to be a crystalline polymorph of manganese dioxide [7] and they have related structures due to the similarity of their oxygen frameworks.

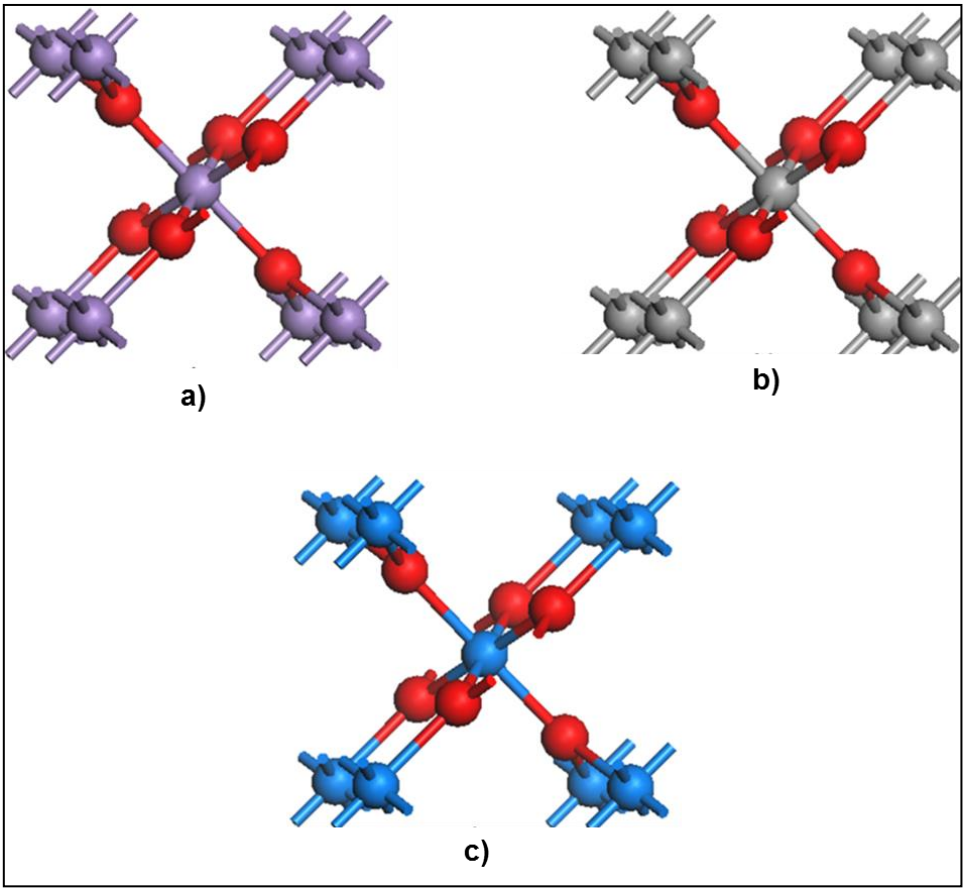

Figure 1.2: Polymorphs of MnO_2, (a) rutile β-MnO_2, (b) rutile β-TiO_2 with the same and (c) structure of β-VO_2 with space group with space group $P4_2/mnm$. Have oxygen represented by red atoms, manganese represented by green atoms and titanium represented by grey atoms and vanadium in blue atoms.

The rutile structure may be described as infinite single chains of edge sharing octahedral which are connected by corners to the other chains whereas the ramsdellite structure contains double chains [7-10]. Rutile has a tetragonal lattice with space group $P4_2/mnm$ as shown for β-MO_2,TiO_2 and VO_2 in figure 1.2 and their oxygen are characterized by a primitive tetragonal packing [10].

Manganese dioxide (MnO_2) has been widely scrutinized as a cathode material in lithium-ion batteries, due to their Li intercalation capacity (forming Li_xMnO_2 phases),

low toxicity, and relative low cost compared to other metal oxides [11-14]. Several MnO_2 polymorphs have been studied in the context of Li-ion cells, including α-MnO_2 (hollandite), β-MnO_2 (pyrolusite), ϒ-MnO_2 (nsutite) and R-MnO_2 (ramsdellite) [11]. Comparing with other polymorphs, the rutile phase (β-MnO_2) does not seem to be able to intercalate Li in the bulk, whereas mesoporous samples of the same polymorph do show a high Li uptake [15].

1.3.2 Surface structure and properties

Other studies used *ab-initio* thermodynamics to study the stable β-MO_2 surfaces and their redox behaviour. The estimated stability of the (110), (100), and (101) stoichiometric surfaces follows the trends previously obtained for rutile TiO_2 and rutile-type SnO_2: (110) > (100) > (101) [16]. Generally, the stoichiometric surfaces are predicted to be observed under environmentally favourable conditions, which are consistent with experiments that reported a manganese valence of 4.0 at the β-MnO_2 surface [17].

Understanding adsorption behaviors of oxygen on the model system of the reduced rutile TiO_2 (110)-1×1 surface is of great importance for an atomistic understanding of many chemical processes. Oxygen molecule can only physisorb weakly on fully oxidised TiO_2 (110) surface [18] but chemisorbs strongly at oxygen vacancy at the bridge oxygen row. In an early temperature programmed desorption (TPD) experiment [19]. Henderson *et al.* predicted that each oxygen vacancy can adsorb at most three O_2 molecules. On the basis of first-principles calculations, Pillay *et al.* suggested that the chemistry of O_2 on the surface is coverage dependent [20].

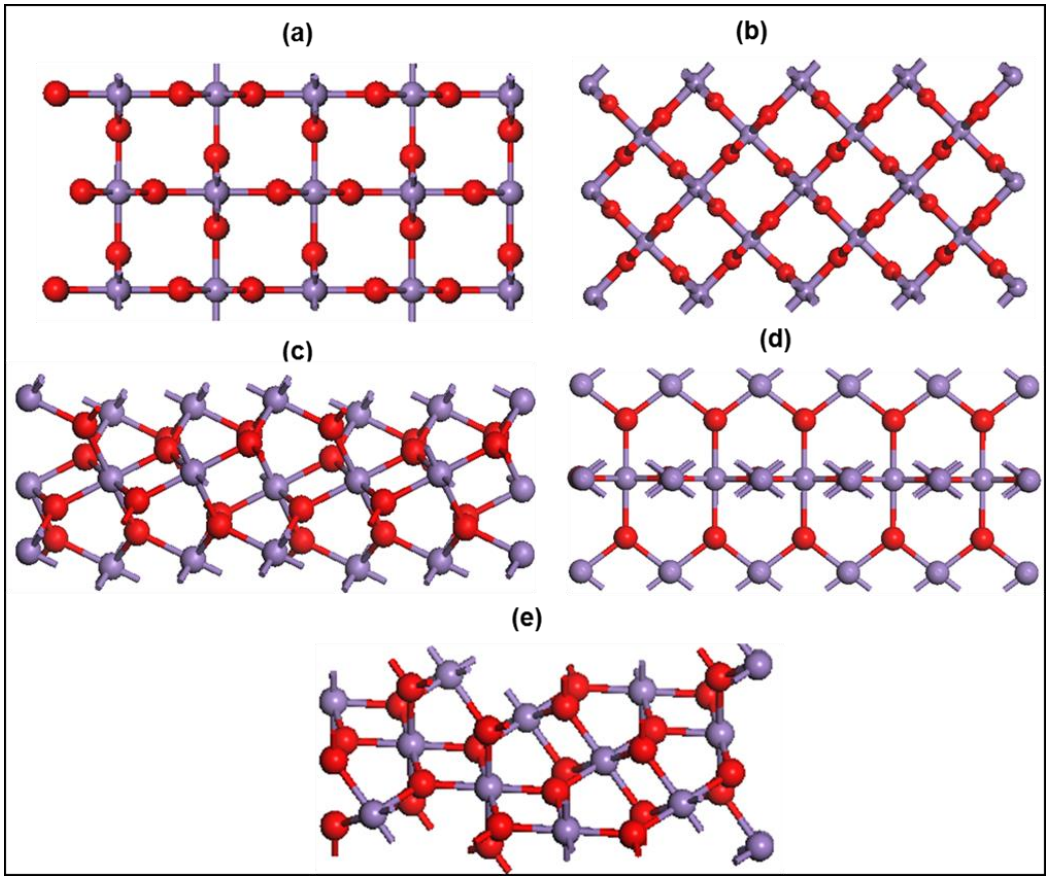

Figure 1.3: β-MnO_2 surfaces. (a) (110), (b) (100), (c) (101), d) (001) and (e) (111) according to their stability trend, red atoms are the oxygen and the purple atoms are the manganese [16].

They also proposed a tetra-oxygen species [21] which was claimed to be confirmed by Kimmel *et al.* [22]; also provided evidence that oxygen vacancy only chemisorb at most two oxygen molecules which will change to tetra oxygen at temperature between 200-400 K, below 200 K, one oxygen molecule was suggested to be adsorbed at oxygen vacancy and the other on the Ti row as superoxide (O_2^-) [22].

At a temperature *T*c ≈341 K, a reversible first-order metal-semiconductor phase transition occurs in pure vanadium dioxide, VO_2 [23]. The abrupt change in electrical resistivity is accompanied by a geometric distortion i.e. in the state above *T*c the oxide has a tetragonal rutile-like structure (VO_2 (R)), while it becomes monoclinic

(VO_2 (M1)) below *T*c. The mechanism of the transition has been discussed for decades, and no clear answer has emerged yet, with some authors arguing that it is dominated by correlation effects and others that it is driven by the structural reconstruction or a combination of the two mechanisms [24-27]

Simulation studies are of great importance in attempts to thoroughly understand surface structures and properties of metal oxides. Surface studies of MnO_2 are not as many as those of TiO_2 [28-30] Adsorption of molecules such as H_2O, CO and O_2 has been of great interest in the surface study field of metals and metal oxides. Oxygen reduction has been extensively studied in catalyst, fuel cell and corrosion [31, 32]

Stoichiometric and defective terminations of the β-MnO_2 (110), (100), and (101) surfaces have been investigated as a function of oxygen partial pressure and temperature using *ab-initio* thermodynamics [16]. In agreement with studies on other rutile-type minerals, the (110) surface is predicted to be the most stable surface, followed by the (100) surface and then the (101) surface.

1.3.3 Catalysts in metal-air battery

It is reported by Abraham *et al.* [33] that rechargeable Li-air cell is composed of a Li anode, a polyacrylonitrile-based gel polymer electrolyte and a porous carbon cathode, Li_2O_2 was identified as the stable discharge product. The formation of Li_2O_2 was consistent with the open circuit voltage of about 2.9 V measured, some of the discharge products are shown in equations 1-3 below:

$Li + O_2 \rightarrow Li_2O_2$; ($E^o = 3.1V$), 1.1

$4Li + O_2 \rightarrow 2Li_2O$; ($E^o = 2.91V$), 1.2

$Li + O_2 \rightarrow LiO_2$; ($E^o = 3.0V$). 1.3

Equations 1-3 reveal that two other products besides Li_2O_2 can be formed from the oxygen reduction reaction (ORR) [33]. In the presence of tetra-butyl ammonium cation, Bu_4N^+, the super oxides, Bu_4NO_2 is extremely stable and withstands further reduction to O_2^{2-} or O^{2-}. In the presence of Li ions, the super oxides, Li_2O_2 is unstable with the half-life of only about 5-10 minutes and decomposes to Li and O_2 [34]. It has been noticed that in the absence of a catalyst the recharge occurs at about 4 V, which is a large hysteresis between charge and discharge voltages. The hysteresis was lowered and the charge/discharge efficiency increased with a catalyst [34].

The schematic of a non-aqueous lithium-air battery is shown in Figure 2-6. It consists of a lithium metal as anode, an air electrode as cathode and a non-aqueous electrolyte. According to Abraham *et al.* [35] reaction mechanisms, which are also given above, are as follows: An oxidation reaction of lithium metal occurs in the anode during discharge. Lithium ions, the product of the oxidation reaction, are transported to the cathode by electrolyte. At the same time, electrons flow through an external circuit to the cathode. In the cathode, oxygen taken from the ambient air is reduced by lithium ions and electrons to Li_2O_2. By calculating the thermodynamics of reactions, the discharge potential generated is 2.96 V. Since the reaction products, lithium oxides are insoluble in the electrolyte, they are stored in the pores of the carbon electrode, and the discharge of the cell theoretically ends when these pores are completely filled with the oxides. Some authors have reported that the production of Li_2O_2 is also possible [36, 37]

Since two lithium atoms per oxygen are required for Li_2O, it will increase the energy stored. If an external voltage, which is higher than 2.96 V, is applied to the cell, the discharge reaction can be reversed. Some studies have been done to observe whether Li_2O_2 deposits dissolve during the charging process or not. Results show that Li_2O_2 dissolves and there is an oxygen evolution at the cathode during charging [35, 38]. Hence, researchers do believe that lithium-air batteries are rechargeable. Moreover, the lithium anode which is in contact with the electrolyte can form a stable solid electrolyte interface (SEI) [39]. SEI makes the electrolyte-lithium metal interface stable that is good for the battery performance.

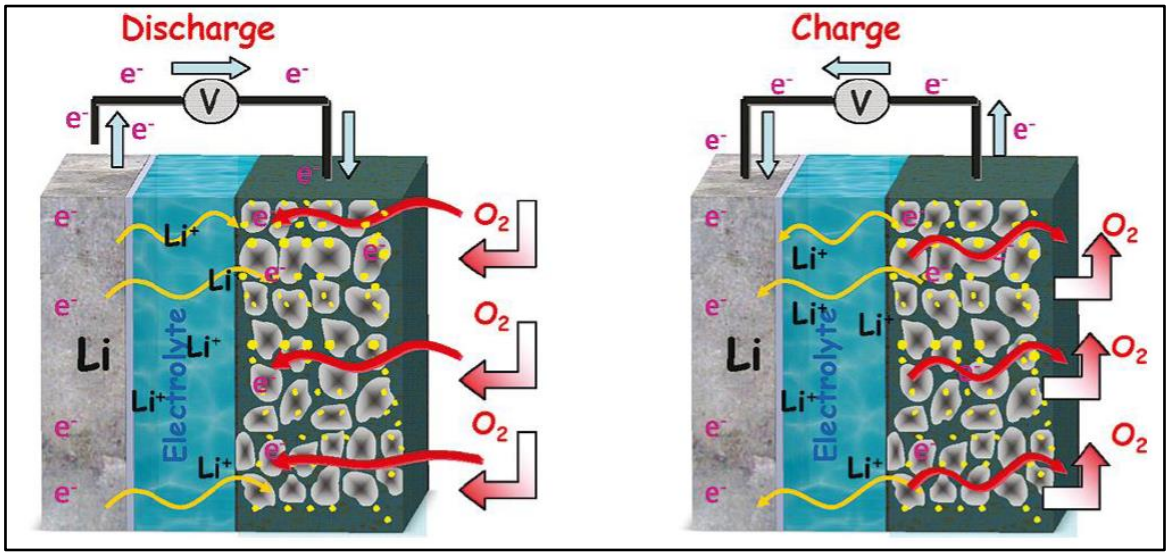

Figure 1.4: Schematic representation of Li air battery showing the discharging and charging cycles.

Catalytic materials have been proposed and synthesized to promote the oxygen reduction reactions and oxygen evolution reactions ORR/OER process, which can be mainly classified into three groups: carbon-based materials [40-43], noble metal/metal oxides [44-50], and transition metal oxides [51-56]. These catalytic materials show notable strengths and weaknesses, e.g. although noble metals/metal oxides, such as Ru/RuO_2 [46, 57-59], could significantly decrease the ORR/OER

overpotentials, their high cost greatly hinders the practical application. In addition, some metal oxides have appeared to cause the decomposition of electrolytes [60].

Several studies have reported the use of noble metals and metal oxides as a catalyst for Li air batteries [61-65]. Transition metal oxides such as Co, Mn oxides have also been considered as potential candidate electrocatalysts for bi-functional oxygen electrodes due to their high catalytic activity and good corrosion stability for Li air batteries [66-69].

Carbon materials are widely used as cathode materials due to their low cost, and good electronic conductivity, while instability still needs to be overcame [70-72]. However, transition metals have attracted much attention as catalysts due to their relatively low cost, moderate catalytic activity for (ORR/OER), and good stability.

Among transition metal oxides, manganese dioxides have been widely investigated as the catalyst for the ORR/OER in non-aqueous lithium-oxygen batteries [33, 34, 73], due to the low cost, environmental friendliness, and easy preparation [74, 75, 76]. Charge voltages of these un-catalysed cells are similar to those of the MnO_2 catalysed cells while both of these exhibits higher charge voltages than the cobalt-catalysed cells [77].

SnO_2 and SnO_2@C have been investigated experimentally, as cathode catalysts of Li-air batteries. They were found to be efficient toward the oxygen reduction reactions, but the carbon coated material of SnO_2@C has shown a better performance, including lower overpotential, larger discharge capacity, and enhanced cycling performance [78].

Song *et al.* demonstrated that the relatively large amount of Mn (III) exposed on the MnO_2 surface can improve the catalytic activity of MnO_2, enabling homogeneous discharge product distribution which will lead to a higher capacity, good rate performance, and lower overpotential [79]. Hu *et al.* prepared a carbon- and binder-free $MnO_{1.957}$/Ni foam electrode by annealing the MnO_2/Ni foam electrode at 350^{o}C for 60 h [80]. Their results also demonstrated that more Mn(III) and oxygen vacancies in MnO_2 can improve the catalytic activity. However, in these reported results, Mn(III) and oxygen vacancy were generated by a calcination method [80, 81], while the high-temperature treatment will seriously lead to the surface oxidation of the substrate [82] and the collapse of MnO_{2-x} nanosheets, which decrease the conductivity of substrate and the active surface areas of MnO_{2-x}.

Among various types of metal oxides, mixed transition metal oxides with a spinel structure are of interest as an electrocatalyst for ORR and OER due to their low cost, good stability, high activity, low toxicity, simple preparation etc. [83-86]. It is well known that the spinel compounds with general formula AB_2O_4 (A, B= Metal) are built around a closely packed array of O^{2-} ions, with A^{2+} and B^{3+} cations occupying part or all of the tetrahedral and octahedral sites, respectively. More importantly, in this structure the solid-state redox couples A^{3+}/A^{2+} and B^{3+}/B^{2+} are easily formed, which makes the spinel materials potentially suitable for electro-catalysis in OER and ORR. In addition, spinel materials anchored on carbon supports have been explored as an oxygen electrode material in Li-O_2 batteries [86-88]. However, as mentioned above, the parasitic reaction of the carbon support with Li_2O_2 results in the limited cycle life for Li-O_2 cells containing spinel catalysts [87]. Hence, to reduce side reactions due to carbon, a free-standing type oxygen electrode without carbon support or substrate needs to be developed and tested.

Catalytic studies in Li air batteries that have been conducted from all types of catalysts (carbon based material, noble metals and metal oxide) both experimentally and computationally demonstrate how they improve performance of Li air battery, specifically the ORR/OER. These studies do not quantify the energetics of the catalyst hence the focus of our project; in this work all the energetics are clearly shown mainly focusing on the ORR which will also help predict the OER.

It is well known that Na-air has lower energy density compared to Li-air batteries [89-91], thus will look at the effect of a catalyst in the formation of NaO_2. The known discharge products in Na-air batteries are shown in the equations that follow:

$Na + O_2 \rightarrow LiO_2$; ($E^o = 2.27V$), 1.4

$Na + O_2 \rightarrow Na_2O_2$; ($E^o = 2.33V$). 1.5

Conversely, in a Na air, the formation of NaO_2 during discharge competes with Na_2O_2 owing to their close equilibrium potentials (2.27 V and 2.33 V, respectively) shown in e. Importantly, Kang *et al*. concluded from computation that Na_2O_2 is a stable bulk phase, whereas NaO_2 is more stable at the nanoscale [92]. Although both the peroxide [93, 94] and superoxide [95, 96] have been reported as the discharge products of a $Na–O_2$ cell, which of these is favoured is not understood. The formation of NaO_2 may be kinetically preferred due to the requirement of only a 1 e- transfer (compared to two for Na_2O_2).

Porous $CaMnO_3$ microsphere is reported to be a new cathode electro-catalyst in the rechargeable Na-air batteries. This catalyst delivers a high specific capacity of 9560 $mAhg^{-1}$, a high rate capacity (1940 $mAhg^{-1}$ and an enhanced cyclability of up to 80 cycles. The micro-nano structure of this catalyst provide active sites for bifunctional oxygen reduction reaction (ORR) and oxygen evolution reaction (OER) and

constructive margin for accommodation of discharge product (NaO_2 and Na_2O_2) of Na-air batteries [97].

1.4 Intentions of the study

Metal-air batteries are attractive for applications where weight is a primary concern, such as in mobile devices. Since oxygen doesn't need to be stored in the battery, the cathode is much lighter than that of a lithium-ion battery, which gives lithium-air batteries their high energy density. The metal-air battery has a potential of providing energy densities up to three times that of the conventional lithium-ion batteries found in just about every portable consumer electronics device (not to mention the incoming wave of electric vehicles) [33]. The performance of this metal-air battery has now raised great interest amongst researchers hence, it is studied extensively. The performance also depends on the choice of a catalyst which will best improve the capacity of these batteries. Compared with noble metal/metal oxides and carbon-based materials, transition metal oxides have attracted much attention as catalysts for cathodes of such batteries due to their relatively low cost, moderate catalytic activity for ORR/OER, and good stability.

Among transition metal oxides, manganese dioxides (MnO_2) have been widely investigated as the catalyst for the ORR/OER in non-aqueous lithium-oxygen batteries, mainly due to environmental friendliness and easy of preparation [74-76]. A question has always been posed why MnO_2 is a preferred metal oxide catalyst in Li-air batteries. In order to elucidate and gain a deeper understanding of this observation, it is necessary to unravel how such compound, together with other related metal oxides play a role in the promotion or inhibition on the growth of

dominant discharge products, such as Li_2O_2 or LiO_2 in Li-air batteries or NaO_2 and Na_2O_2 in Na-air batteries.

In the study the following approach will be followed. Morphologies of the rutile type metal oxides, i.e. MnO_2, TiO_2 and VO_2 will be investigated and reviewed in order to identify the most stable surfaces. Redox properties of MO_2 will be studied where oxygen atoms and molecules will be added to the surface (adsorption), at different orientations i.e. bridging, mononuclear, at some instances an oxygen atom will be added on top of the manganese atoms on the surface followed by the adsorption with oxygen molecule. This will enable the calculation of the adsorption energy on the non-stoichiometric surface. From the adsorbed surfaces, we will determine which metal oxide oxidise better and to what extent and for the surfaces with vacancies, will determine how stable the surface is when partial reduction compare with full reduction.

Lithium and sodium adsorption on clean surfaces will be investigated by placing Li/Na atoms at different positions in order to find the most stable position on the (110) surface of the three metal oxides. This is performed in order to mimic cycling of the metal air batteries. Furthermore, co-adsorption of oxygen on lithium and sodium adsorbed surfaces will be carried out where oxygen atoms are placed in bulk-like composition and oxygen molecule located in a peroxo form on Li/Na-MO_2. Co-adsorption of oxygen is performed in order to imitate discharge cycle of the metal air battery where oxygen molecules from the atmosphere will combine with Li/Na from the anode to form discharge products of metal-air batteries.

A comparative surface adsorption study on the metal oxides will highlight which of the metal oxide will make a better catalyst, based on whether the catalyst

encourages formation or inhibition of discharge products reported in literature for both Li and Na air batteries.

1.5 Outline of the study

Chapter one gives an introduction, literature review, structural aspect of MnO_2, TiO_2 and VO_2 systems and intentions of the study are given.

Chapter two gives a theoretical background of the methods used in the study, which are the density functional theory and Hartree-Fock approach. A detailed description of the approximation used in this study, i.e. the generalised gradient approximation (GGA) and the local density approximation (LDA) will be given.

Chapter three focuses on validations of the cutoff and k-points for the metal oxides (MnO_2, TiO_2 and VO_2) and results and discussions on stability and redox properties on β-MO_2 (110) surfaces

Chapter four gives a detailed discussion on lithium adsorption on the clean (110) for (MnO_2, TiO_2 and VO_2) surface and charge transfer and adsorption of oxygen on lithiated metal oxides. The effect of the catalyst (MO_2) in the cathode in a Li-air battery is also discussed in this chapter.

Chapter five discussed sodium adsorption on the MnO_2, TiO_2 and VO_2 (110) surface in a similar way as chapter four.

Chapter six finally gives summary conclusion of the work, where the three metal oxides were compared looking at the similarities and differences when adsorbing and co adsorbing with lithium/sodium and oxygen. Future work and papers presented based on the study is also presented in this chapter.

Chapter 2: Computational methods

2.1 Introduction

In this chapter, a detailed description of the computational methods we have applied will be discussed. First principle density functional theory (DFT) study of MnO_2 TiO_2 and VO_2 is performed with the Vienna *Ab-initio* Simulation Package (VASP) code. The DFT approximations methods, plane wave pseudopotential methods and the implementation of the VASP code will be described.

2.2 *Ab-initio* methods

These methods are computational chemistry methods based on quantum chemistry [49]. In *ab-initio* methods, the model is done mathematically, based on Scrödinger equation. These methods are considered as the most accurate, as well as difficult, in all of the techniques in use in the field of molecular modelling [98].

An important reason for this is that, the *ab-initio* methods start from the very beginning. It starts with the molecular structure and few constants, one can calculate numerous chemical properties, make insights into the reactivity of a molecule, and observe the shapes of molecular orbitals. This means that the integrals involved in the Schröedinger equation for the system are explicitly solved without the use of empirical parameters. The starting point for the *ab-initio* methods is the optimized nuclear configuration, which can be obtained by using molecular mechanics method. However, these methods have some disadvantages: the most prominent disadvantage of these methods is that they have significant limitations on the size of the molecule.

The simplest type of *ab-initio* electronic calculation is the Hartree-Fork (HF) scheme, in which the instantaneous Coulombic electron-electron repulsion is not specifically taken into account. Only the average (mean field) effect is included in the calculation. Born-oppenheimer approximation, which reduces the Schröedinger equation for molecular system to only the electronic motion for a particular nuclear configuration is the first assumption to be made. The Hamiltonian for the molecular system with the Born-oppenheimer approximation is given by

$$\hat{H} = -\frac{1}{2}\sum_{a}^{electrons}\nabla_a^2 - \sum_{A}^{nuclei}\sum_{a}^{electrons}\frac{Z_A}{r_{Aa}} + \sum_{A>B}^{nuclei}\sum_{B}^{nuclei}\frac{Z_A Z_B}{R_{AB}} + \sum_{a>b}^{electrons}\sum_{b}^{electrons}\frac{1}{r_{ab}}, \qquad 2.1$$

where H is the Hamiltonian and the inter-nuclear distances (R_{AB}) are constant for a particular nuclear configuration, due to the Born-oppenheimer approximation [99]. Hence we express the Born-oppenheimer Hamiltonian as only the operator parts in terms of the electrons.

$$\hat{H}^{electrons}\psi^{electrons} = E^{electrons}\psi^{electrons}, \qquad 2.2$$

where ψ is the wavefunction and E is the energy of the molecule.

$$E = E^{electrons} + \sum_{A>B}^{nuclei}\sum_{B}^{nuclei}\frac{Z_A Z_B}{R_{AB}}. \qquad 2.3$$

The *ab-initio* methods include numerous methods such as DFT and Hartree-Fock.

2.2.1 Density functional theory

DFT is presently the most successful approach to compute the electronic structure of matter. Its applicability ranges from atoms, molecules and solids to nuclei and quantum and classical fluids quantum and classical fluids. Although DFT is based on the concept by Thomas and Fermi, it was developed by Kohn and Hohenberg

[100], Using two theorems (Kohn-Hohenberg theorems). The first theorem demonstrates that the ground states properties of many-electron system are uniquely determined by an electron density that depends only on 3 spatial coordinates. This first theorem lays the ground work for reducing many-body system by the use of functional of the electron density. The second theorem defines energy functional for the system and proves that the correct ground state electron density minimizes this energy functional.

DFT determines properties of many-electron systems using functionals, which is dependent to the density of electrons. The DFT is one of the most popular and versatile methods in condensed-matter physics, computational physics and computational chemistry. Over the past four decades, DFT has been the most popular and dominating method for calculations in solid state physics and quantum mechanical simulations of periodic systems. The DFT method was not recognized as accurate enough for quantum chemistry calculations until 90s, when the approximations involved in the method were improved to model the exchange and correlation interactions [101].

However, despite of these improvements, DFT still cannot properly describe intermolecular interactions, especially the Van der Waals forces; charge transfer excitations; transition states, global potential energy surfaces and some other strongly correlated systems; and in calculations of the band gap in semiconductors [102]. An important improvement in the calculation of the energy of electrons was done by Kohn and Sham. They proved that the properties of the total ground state of interacting electron gas may be described by introducing certain functional of the electron density $\rho(r)$, which depends on the positions of atoms [103].

$$E(\rho) = \int dr\rho(r)\upsilon_{ext}(r) + \iint drdr' \frac{\rho(r)\rho(r')}{|r - r'|} + G[\rho], \quad 2.4$$

where $\upsilon_{ext}(r)$ is the external field integrating the field of the nuclei; the functional $G(\rho)$ comprises the kinetic and exchange-correlation energy of the interacting electrons. $G(\rho)$ is universal and is independent of the external fields. Furthermore, this expression is a minimum for the correct density function $\rho(r)$. This allowed Kohn and Sham [104] to further develop the concept and suggested the form of $G(\rho)$

$$G(\rho) = T(\rho) + E_{xc}(\rho), \quad 2.5$$

where $T(\rho)$ is the kinetic energy of the non-interacting electrons with density $\rho(r)$ and the functional $E_{xc}(\rho)$ encompasses the many-electron effects of the exchange and the correlation. As the exact many-body and correlation interactions are unknown, there is an approximation that the exchange-correlation is taken from the known results of an interacting electron system of constant density (homogeneous electron gas) and it is assumed that exchange and correlation effects are not strongly dependent on inhomogenities of the electron density away from the reference point r. It is therefore necessary to determine the set of wavefunction ψ_i that minimizes the Kohn-Sham energy function. The electron density is written as follows;

$$\rho(r) = \sum_{i=1}^{N} |\psi_i(r)|^2, \quad 2.6$$

where N the number of electrons. The Kohn-Sham energy function is given by a self-consistent solution of the equation:

$$\left[-\nabla^2-\sum_I\frac{2Z_I}{|r-R_I|}+\int 2\frac{\rho(r')}{|r-r'|}dr'+V_{xc}(r)\right]\psi_i=\varepsilon_i\psi_i, \qquad 2.7$$

where R_I is the position of the nucleus I of charge Z_I; ε_i are the Lagrange factors. The exchange-correlation potential, V_{XC} is given by the functional derivative

$$V_{XC}(r)=\frac{\delta E_{XC}[\rho(r)]}{\delta\rho(r)}. \qquad 2.8$$

Though thoroughly applicable for ground state and the exchange-correlation energy, DFT is only known by approximation, the significance of this theory to practical uses can hardly be overemphasized. It reduces the many-electron problem to an essentially single-particle problem with the effective local potential

$$V(r)=\sum_I\frac{2Z_I}{|r-R_I|}+\int 2\frac{\rho(r')}{|r-r'|}dr'+V_{XC}(r). \qquad 2.9$$

The most important concern when applying DFT is the way in which the functional E_{xc} is defined. The energy functional, $E_{xc}(\rho)$ for inhomogeneous electron gas can be expressed as Coulomb interaction between the electron and its surrounding exchange-correlation hole [105, 106]

$$V_{xc}[\rho]=\frac{1}{2}\int dr\rho(r)\int dr'\frac{(r,r'-r)}{|r-r'|}. \qquad 2.10$$

As already stated above, the major problem with DFT is that the exact functional for exchange and correlation is not known except for the free electron gas. However, there are approximations that allow the performing of these calculations. There are two commonly used approximations: namely local density approximation (LDA) and generalized gradient approximation (GGA).

2.3 Approximation methods

2.3.1 Local density approximation

Local density approximations are class of approximations to the exchange correlation (XC) energy functional in the DFT that that are determined by the electronic density at each point in space. The LDA states that, for regions of a material where the charge density is slowly varying, the exchange correlation energy at that point can be considered the same as that for a locally uniform electron gas of the same charge density. This is the most widely used approximation, which locally substitutes the exchange-correlation energy density of an inhomogeneous system by that of an electron gas evaluated at local density. LDA rests upon two basic assumptions: first being that the exchange and correlation effects come predominantly from the immediate vicinity of point r and the second being that these exchange and correlation effects do not depend strongly on the variations of the electron density in the vicinity of r [107]. The fulfilment of these two conditions results same contribution from the volume element dr as if this volume element were surrounded by a constant electron density $\rho(r)$ of the same value as within dr. In this approximation, the exchange-correlation energy density of the homogeneous electron gas $E_{XC}^{\hom}(\rho_0)$ dependent on the homogeneous density ρ_0 and replaces this for the inhomogeneous system with density $\rho(r)$ by

$$E_{XC}^{LDA}(\rho(r)) = E_{XC}^{\hom}(\rho_0)\,|_{\rho_0} = \rho(r). \qquad 2.11$$

For spin-unpolarized system (where the functional depends only on the density) a local density approximation for the exchange-correlation energy is written as

$$E_{XC}^{LDA}[\rho] = \int p(r)\varepsilon_{XC}(\rho)dr \qquad 2.12$$

and

$$\frac{\delta E_{XC}(\rho(r))}{\delta\rho(r)} = \frac{\partial[\rho(r)\varepsilon_{XC}(r)]}{\partial\rho(r)} \qquad 2.13$$

where ρ is the electronic density and E_{XC} the exchange-correlation energy density. This approximation only work for systems with slowly varying densities, such as the weakly perturbed electron gas, and also works well even for systems which have very inhomogeneous electron densities such as atoms and molecules. When considering the xc-hole and the pair correlation function, we get a more detailed look on LDA

$$\rho_{Xc}^{LDA}(r_1, r_2) = \rho(r_1)[g^{\hom}([\rho]; | r_1 - r_2 |], \qquad 2.14$$

where $g^{\hom}[\rho]$ is the coupling constant integrated pair-correlation function of the homogeneous electron gas [108]. The exchange-correlation part of the pair-correlation function which is unaffected by the coupling constant integration is given by

$$g_{xc}^{LDA}([\rho]; r_1, r_2) = 1 - \frac{9}{2}\left[\frac{\sin(k_F(r_1) | r_1 - r_2 |) - k_F(r_1) | r_1 - r_2 | \cos(k_F(r_1) | r_1 - r_2 |)}{(k_F(r_1) | r_1 - r_2 |)^3}\right]^2, \qquad 2.15$$

where $k_F(r)$ is the local Fermi wave vector defined as;

$$k_F(r) = \left(\frac{3}{\pi}\right)^{\frac{1}{3}} \rho(r)^{\frac{1}{3}} \qquad 2.16$$

The exchange-correlation energy is decomposed into exchange and correlation terms linearly as,

$$E_{XC} = E_x + E_c, \tag{2.17}$$

where E_X represents the exchange energy and *Ec* is the correlation energy, respectively. The exchange term takes on an analytic form for the homogeneous electron gas (HEG). Exchange-energy density of a HEG is known analytically. The LDA for exchange employs this expression under the approximation that the exchange-energy in a system where the density in not homogeneous, is obtained by applying the HEG results pointwise, yielding the expression [109,110].

$$E_x^{LDA}[\rho] = -\frac{3}{4}\left(\frac{3}{\pi}\right)^{\frac{1}{3}} \int \rho(r)^{\frac{4}{3}} dr. \tag{2.18}$$

This equation satisfies the correct exchange scaling. There are corresponding equations for the correlation part of $g^{\text{hom}}[\rho]$ and for $E_C^{LDA}[\rho]$. The LDA xc-hole is spherical around the reference electron and is given as

$$\rho_{XC}^{LDA}(r_1, r_2) = \rho_{XC}(r_1, s) \tag{2.19}$$

where $s = | r_1 - r_2 |$ and it also satisfy the sum rule

$$\int \rho_{XC}^{LDA}(r_1, r_2) dr_2 = 4r \int_0^{\infty} \rho_{XC}^{LDA}(r_1, s) s^2 ds = -1. \tag{2.20}$$

Analytic expressions for the correlation energy of the HEG are not known except in the high-density and low-density limits corresponding to infinitely-weak and infinitely-strong correlation [109]. For a HEG with density *ρ*, the high-density limit of the correlation energy density is

$$\varepsilon_c = A\ln(r_s) + B + r_s(C\ln(r_s) + D), \tag{2.21}$$

and the lower limit is given as

$$\varepsilon_c = \frac{1}{2}\left(\frac{g_0}{r_s} + \frac{g_1}{r_s^{\frac{3}{2}}} + ... \right), \qquad 2.22$$

where the Wigner-Seitz radius is related to the density as;

$$\frac{4}{3}\pi r_s^3 = \frac{1}{\rho}. \qquad 2.23$$

LDA approximates the energy of the true density by the energy of a local constant density, and fails in situations where the density undergoes rapid changes such as in molecules. The Local Spin Density (LSD) also is not accurate enough for most chemical applications, which require determination of energy differences with considerable precision. The LSD has been used to calculate the electronic structure of in solid state physics for many years [111,112]. This approximation is given by

$$E_{XC}^{LSD}[\rho_\uparrow, \rho_\downarrow] = \int d^3 r \rho(r) \varepsilon_{XC}^{unif}[\rho_\uparrow(r), \rho_\downarrow(r)], \qquad 2.24$$

where $\varepsilon_{Xc}^{unif}(\rho_\uparrow, \rho_\downarrow)$ is the exchange-correlation energy per particle of a uniform electron gas [113-115].

2.3.2 Generalized gradient approximation

The GGA has been introduced as an improvement to the LDA; this is done by extending the exchange-correlation functional with terms containing gradients of the electron density. These gradients measure changes of the electron density and can be used to advance the local density approximation. The theory of most gradient functional developed is based upon the weakly varying electron gas [108]. These approximations are called Gradient Expansion Approximation (GEA), and can be written as

$$E_X^{GEA}[\rho] = E_X^{LDA}[\rho] + \beta \int \frac{(\nabla\rho)^2}{\rho^{\frac{4}{3}}} dr + ... \qquad 2.25$$

$$E_c^{GEA}[\rho] = E_C^{LDA}[\rho] + \int C(\rho)\frac{(\nabla\rho)^2}{\rho^{\frac{4}{3}}}dr + ... \qquad 2.26$$

where β is a constant and $C(\rho)$ is a function determined by response theory. However the GEA provides no improvement over the LDA since the ealistic densities in atoms and molecules do not vary slowly over space. When analysis of the gradient expansion of the xc-hole is done, they show that the short range part (near the reference electron) is improved, but the long range is made worse [116]. The corresponding approximations of the GEA are GGA.

The generalized gradient approximation can be written as;

$$E_{XC} = E_{XC}[\rho(r), \nabla\rho(r)]. \qquad 2.27$$

This can lead to a large improvement over LDA results with accuracy approaching that of correlated wavefunction methods. While there is only one LDA there are several different parameterizations of the GGA. Some of these are semi-empirical, in that experimental data (e.g. atomization energies) is used in their derivation. Others are found entirely from first-principles. A commonly used functional is the PW91 functional, due to Perdew and Yang [115-118]. But the newer Generalized Gradient Approximation which gradient-corrected functional is of the form

$$E_{XC}^{GGA}[\rho_\uparrow, \rho_\downarrow] = \int d^3 r f(\rho_\uparrow(r), \rho_\downarrow(r), \nabla\rho_\uparrow, \nabla\rho_\downarrow), \qquad 2.28$$

This expression was found to reduce LSD atomization energy errors by a factor of 5 [119]. The most widely used GGA's are the Becke GGA [120] for the exchange energy and the exchange- and correlation GGA's by Perdew [121] and Perdew and Wang [116,122-124]. The Becke GGA correction to the LDA is of the form

$$E_x^{GGA}[\rho_\uparrow, \rho_\downarrow] = E_X^{LDA} - \beta\int \sum_\sigma \frac{\rho_\sigma(r)^{\frac{4}{3}} x_\sigma^2}{1 + 6\beta x_\sigma \sinh^{-1} x_\sigma} d^3 r, \qquad 2.29$$

where

$$E_X^{LDA} = -C_{X\sigma} \sum \rho_\sigma^{\frac{4}{3}}(r) d^3(r), \qquad 2.30$$

$C_X = \frac{3}{2}\left(\frac{3}{4\pi}\right)$, $X_\sigma = \frac{|\nabla\rho|}{\rho_\sigma^{\frac{4}{3}}}$, σ denotes either $\uparrow or \downarrow$ electron spin. β (Constant) is a parameter to obtain the correct exchange energy for the noble gas. The following correlation functional as proposed by Perdew and Wang [122] predicts correlation energies of useful accuracy for an electron gas with slowly varying density:

$$E_X^{GGA}[\rho_\uparrow, \rho_\downarrow] = \int \rho(r)\varepsilon_C(\rho_\uparrow, \rho_\downarrow) d^3r + \int \frac{C_C(\rho)|\nabla\rho(r)|^2}{de^\phi \rho(r)^{\frac{4}{3}}} d^3r \qquad 2.31$$

where

$$d = 2^{\frac{1}{2}}\left[\left(\frac{1+\zeta}{2}\right)^{\frac{5}{3}} + \left(\frac{1-\zeta}{2}\right)^{\frac{5}{3}}\right], \qquad 2.32$$

$$\phi = 0.1929\left[\frac{C_C(\infty)}{C_C(\rho)}\right]\frac{|\nabla\rho|}{\rho^{\frac{7}{6}}}, \qquad 2.33$$

$\zeta = (\rho_\uparrow, \rho_\downarrow)/\rho$ and $C_C(\rho)$ is a rotational polynomial of the density that contains seven fitting parameters. The exchange functional, written by Perdew-Burke-Ernzerhof is explained in the form that contains an explicit enhancement fact over the local exchange factor, which is normally known as GGA-PBE

$$E_X^{PBE}[\rho_\uparrow, \rho_\downarrow] = \int \rho(r)\varepsilon_X^{LDA}[\rho(r)]F_{XC}(\rho, \xi, s)dr, \qquad 2.34$$

where ρ is the local density, ξ is the relative spin polarization, and $s = |\nabla\rho(r)|/(2k_F\rho)$, is the dimensionless density gradient. The factor in enhanced in the following way

$$\left(sF_X = \left(\frac{1}{k + s^2\mu}\left(k + s^2\mu + s^2 k\mu\right)\right)\right), \qquad 2.35$$

where $\mu = \beta\left(\frac{\pi^2}{3}\right) = 0.21951$ with $\beta = 0.066725.$ The correlation energy is

$$E_C^{PBE}[\rho_\uparrow, \rho_\downarrow] = \int \rho(r)\left[\varepsilon_C^{LDA}(\rho,\zeta) + H(\rho,\zeta,t)\right]dr, \quad 2.36$$

with

$$H(\rho,\zeta,t) = \left(\frac{e^2}{a_0}\right)\gamma\phi^3 \times \ln\left\{1 + \frac{\beta}{\gamma}t^2\left[\frac{1+At^2}{1+At^2+A^2t^4}\right]\right\}, \quad 2.37$$

where

$$A = \frac{\beta}{\gamma}\left[e^{\varepsilon_C^{LDA}[\rho]/\gamma\phi^3} - 1\right]^{-1}, \quad 2.38$$

$t = \left|\nabla\rho(r)/(2k_s\rho)\right|$ is the dimensionless density gradient,

$ks = \left(\frac{4k_F}{\pi}\right)^{\frac{1}{2}}$ is the Thomas-Fermi screening wave number and

$\phi(\zeta) = \left[(1+\zeta)^{\frac{2}{3}} + (1-\zeta)^{\frac{2}{3}}\right]$ is the spin-scaling factor.

Under uniform scaling to the high density limit, E_C^{GGA} tends to

$$-\frac{e^2}{a_0}\int d^3r n\gamma\phi^3 \times \ln\left[1 + \frac{1}{\chi s^2/\phi^2 + (\chi s^2/\phi^2)^2}\right], \quad 2.39$$

where $s = |\nabla n|/2k_F n = (r_s/a_0)^{1/2}\phi t/c$ is another dimensionless density gradient.

2.4 Plane –wave pseudopotential method

The plane wave pseudopotential method for the DFT is a technique used to calculate the variation self-consistent solution with accuracy. This method has been advanced and perfected to reliably predict the static and dynamic properties of molecules and crystalline solids [124]. The complicated many-body problem of strongly correlated electrons and nuclei has been mapped within the framework of the Born-

Oppenheimer approximation and the Density Functional Theory to a single-particle problem moving in an effective external potential for a set of fixed nuclei. The practical numerical scheme to solve the resulting single-particle Kohn-Sham equation for extended systems like crystalline solids or liquids is developed. And most common approach for solving this problem is to expand the wavefunctionof the single-particle eigenstates of the Kohn-Sham equations into a set of basis functions. Then, the Schrodinger equation transforms into an algebraic equation for the expansion coefficient solved by numerical perfected method. Basically, the Plane wave Pseudopotential Method deals with weak pseudopotentials and performs complete geometry optimization, more especially the relaxation of internal parameters. Plane wave pseudopotential method is also able to simulate the electronic ground states for metals, insulators and semiconductors.

2.4.1 Plane wave basis sets

The plane wave basis sets are abundantly used in the calculations involving boundary conditions. In addition to the localized basis sets, plane wave basis sets are also used in quantum-chemical calculations. Plane wave basis sets are usually coupled with an “effective core potential” or pseudopotential in practical performance, so that they (plane wave) are only used for valence charge density. The plane wave basis is more efficient than the Gaussian-type basis because is guaranteed to converge to the target wavefunction, while there is no such in the Gaussian-type. Since there is infinite number of electrons, a wavefunction is needed for each individual electron. However, the basis set required for the expansion of each wavefunction is also infinite. Bloch’s theorem, which starts with periodicity of the crystal lattice, can handle this problem. Bloch’s theorem defines the crystal

momentum k as good quantum number and also gives the boundary condition for the single particle wavefunction, φ_k. Bloch's theorem is often stated in an alternative form: the equation

$$\varphi_k(r + R_L) = e^{ik.R_L}\varphi_K(r), \quad 2.40$$

is equivalent to the statement that all eigenfunctions φ_{ki} of a single–particle Schrodinger equation with periodic potential can be written as a periodic function u_{ki} modulated by a plane wave vector *k* [125]. R_L is a direct lattice vector.

$$\varphi_{kj}(r) = e^{ikr}u_{kj}(r) \quad 2.41$$

Due to its periodicity u_{ki} can be expanded as a set of plane wave basis

$$u_{kj}(r) = \sum_G C_{j,G}\, e^{iG.r}, \quad 2.42$$

where G are reciprocal lattice vectors. The functions u_{ki} are periodic and can be expanded in a set of plane waves. Thus the electronic wavefunction with the exponential prefactor is

$$\varphi_{kj}(r) = \sum_G C_{j,k+G} e^{i(K+G)r}, \quad 2.43$$

where $C_{j,K+G}$ coefficient of the periodic plane waves. As it is the case with an infinite number of basis functions is needed to accurately recreate the real wavefunction. The number of wavefunctions used is controlled by the largest wave vector in the expansion in 2.44. This is equivalent to imposing a cutoff on the kinetic energy as the kinetic energy of an electron with wave vector *k* is given by

$$E_K = \frac{\hbar^2 |K+G|^2}{2m}, \quad 2.44$$

Thus only plane waves that obey

$$E_K = \frac{\hbar^2 |K+G|^2}{2m} < E_{cut}, \quad 2.45$$

are included in the basis. The plane wave basis set at finite cutoff energy will lead to an error in the computed total energy; hence the energy must be increased until the calculated energy has converged. It is highly advisable and wise to use much denser k points to reduce errors and ensure convergence. Before making use of the plane wave expansion of the wavefunction we write the Kohn-Sham equation of density fuctional theory in the following way [124]:

$$\sum \left[\frac{\hbar^2}{2m} |K+G|^2 \delta_{GG} + V_{eff}(r) \right] C_{j,K+G} = \varepsilon_j C_{j,K+G}, \quad 2.46$$

where the effective potential is written as,

$$V_{eff}(r) = V_{ext}(r) + V_H[\rho(r)] + V_{XC}[\rho(r)] \quad 2.47$$

where

$V_{ext}(r)$, $V_H[\rho(r)]$, and $V_{XC}[\rho(r)]$ are Fourier transforms of the external potential of the nuclei, Hartree and exchange-correlation potentials, respectively.

2.4.2 Pseudopotentials

Pseudopotential is used as an approximation of complex systems. They are applied in atomic physics and neutron scattering. Most physical and chemical properties depend on the distribution of valence electrons, while the core electrons don't participate in a chemical bonding. The core electrons are strongly localized around the nucleus, and their wavefunction overlap less with the core electron's wavefunction of the next neighbouring atoms. Hence, the distribution of core electrons is basically the same irrespective of which chemical environment the atom is in. Therefore, the core electrons are declared "frozen" and the core electron distribution is kept in the crystal environment. This is an advantage since few electrons have to be treated and few eigenstates of the Kohn-Sham equations have

to be calculated. Secondly, the total energy scale is largely reduced by the removal of core electrons from the calculation which makes the calculation of the energy differences between atomic configurations numerically much more stable. Hence the introduction of pseudopotential approximation is an attempt to eradicate the unsolvable complicated effects of the core electrons in motion and their nuclear with an effective potential, or pseudopotential [126-128]. Thus the Scrödinger equation now contains a modified effective potential term instead of the coulombic potential term for core electrons. In the pseudopotential approach, only valence electrons are dealt with explicitly [129-133].

The schematic figure 2.1 above explains these properties of the pseudopotential. Due to strong ionic potential, the valence wavefunctions oscillate rapidly in the region occupied by the core electrons. Hence, the orthogonality between the core electrons and valence electrons is maintained due to these oscillations. The pseudopotential is constructed such that the pseudo wavefunction has no radial nodes within the core region and that the pseudo wavefunctions and potential agree with the true wavefunction and potential outside some cutoff radius (r_{cut}). The pseudopotential also must preserve the atomic properties of the element, including phase shifts on scattering across the core.

In general the pseudopotential must be non-local, i.e. it must have projectors for the different angular momentum states. The general form of the pseudopotential is

$$V_{ion} = \sum |lm\rangle V_i \langle lm|, \qquad 2.48$$

where $|lm\rangle$ are spherical harmonics, and V_i is the pseudopotential for angular momentum (l) [125].

The majority of the pseudopotentials used in electronic structure are generated from all electron atomic calculations. Norm-conserving pseudopotential is the example of non-local pseudopotential and uses a different potential for each angular momentum components of the wavefunction. However, pseudopotential that uses the same potentials for all angular momentum components of the wavefunction is called local pseudopotential. Between the two pseudopotential, local pseudopotential is computationally efficient than non-local pseudopotential.

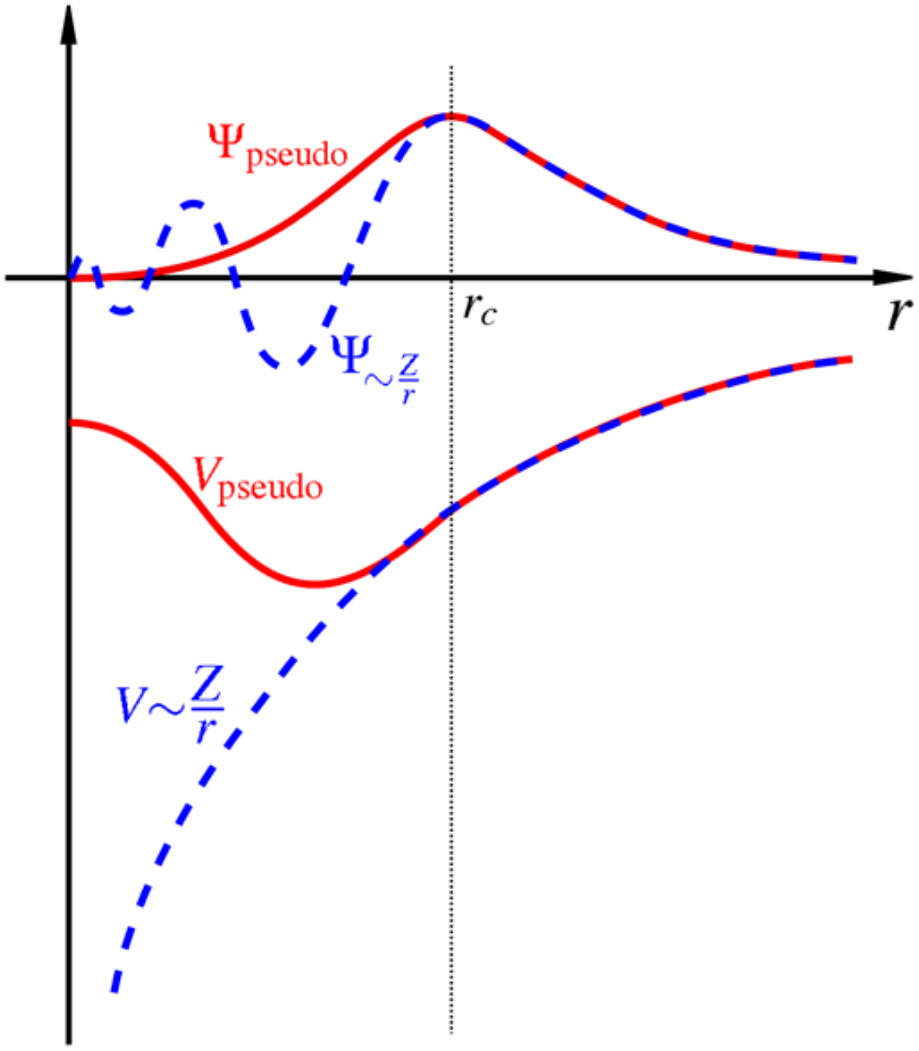

Figure 2.1: Schematic illustration of an atomic all-electron wavefunctionand the corresponding atomic pseudo wavefunctions [134].

2.4.3 Norm- conserving pseudopotentials

Pseudopotentials constitutes a possible way of avoid atomic core states in first-principles calculations of molecules and solids. The basic concept of the pseudopotential is a frozen core approximation which assumes that core states are insensitive to the neighbouring atomic configuration. Pseudopotentials simplify electronic structure calculations by eliminating these atomic core states and strong potentials responsible for binding them [135]. The need to avoid core states arises because of expensive work of taking into account all atomic states in such calculations, and that chemical bonds in molecules and solids involve valence states to a major extent. *Ab-initio* pseudopotential methods require electrons that move in the electric potential produced by the atomic nuclei together with core electrons. So the total effect (Coulomb and exchange-correlation interactions) of core electrons may be replaced by an adequate potential: the pseudopotential.

Hamann *et al*. [135] proposed a norm-conserving pseudopotential type which is completely non-empirical. This type of pseudopotential allows obtaining the pseudo wavefunctions which are identical to real wavefunctions beyond a chosen core radius, whose eigenvalue agree with the real eigenvalue. This property produces a correct description of bonding in pseudopotential calculations, and corrects self-consistent electrostatics and exchange-correlation potentials. Simultaneously, norm-conserving pseudopotentials produce the scattering power of the full atom potential correctly at energies away from the bound valence state energy to first order in the energy difference. Consequently, norm-conserving pseudopotentials reproduce all-electron electronic structure calculations with high degree of accuracy.

2.4.4 Projector augmented wave method

The method uses the project augmented wave (PAW) within the architecture of DFT, it has been observed to give reasonable results for electronic and structural properties of diverse solids. The PAW method is reliable and has been used a lot and works like pseudopotentials. Wavefunctions of materials have different trademarks in different regions of space; in the bonding region the wavefunction is smooth, while close to the nucleus the wavefunction oscillates swiftly as a result of large attractive potential of the nucleus. The strategy of the PAW has been to divide the wavefunction into parts: a partial-wave expansion within an atom-centered sphere and envelope functions outside the spheres [136]. This method is related to the ultrasoft pseudopotentials and allows the wavefunctions including the core electron wavefunctions to be calculated. In this method, the full wavefunctions is changed onto auxiliary wavefunctions. The auxiliary functions can be developed relatively easily in a plane wave basis, while the full wavefunctions are augmented with atomic wavefunctions. PAW method assumes the frozen-core approximation but is significantly more transferable than pseudopotentials [46].

2.4.5 Ultrasoft pseudopotentials

In 1990, Vanderbilt [137] developed a pseudopotential known as “ultrasoft pseudopotentials”. Many of the modern pseudopotential calculations use this generalization of the Kleinman-Bylander. This approach is a radical departure from norm-conserving pseudopotentials discussed above. Ulrasoft pseudoportentials attain much smoother pseudo wavefunctions as the name states. In this approach, the pseudo wavefunctions are required to be equal to all electron wavefunctions outside the radius, as with the norm-conserving pseudopotentials, but inside the

radius are allowed to be as soft as possible; the norm-conserving constraint is removed to accomplish this, but however, this introduces some complications. But, still the ultrasoft pseudopotential reduces the plane wave cutoff needed in calculations, particularly because large values of radius can be used in their scheme. The complications that result are two-fold. First of all, since the pseudo-wavefunctions are equal to the all-electron wavefunctions (and therefore have the same norm) in the interstitial, but do not have the same norm inside *TC* they are necessarily not normalized. Secondly, the pseudo charge density is not obtained by computing $\sum \varphi^* \varphi$ as with norm-conserving pseudopotentials; this will lead to the wrong total charge. A third, but less important, complication is that by relaxing the norm conservation, the resulting pseudopotentials can become less transferable. However, Vanderbilt pseudopotentials were proposed for use in large scale calculations, for which the cost of generating pseudopotentials is negligible compared with the cost of the calculations. The electron density is subdivided into a smooth part that extends throughout the unit cell and a hard part localized in the core region. Ultrasoft pseudopotentials have an advantage over the norm-conserving pseudopotential.

2.5 Implementation within VASP

VASP is a complex package designed to perform first principle, *ab-initio* quantum mechanical molecular dynamics (MD) simulations using pseudopotentials or the projector-augmented wave method and a wave basis set [138]. The approach implemented in VASP is based on the (finite temperature) local density approximation with the free energy as variational quantity and an exact evaluation of the instantaneous electronic ground state at each MD time step. VASP uses efficient

matrix diagonalisation schemes and efficient Pulay/Broyden charge density mixing. These technique is highly advanced that it also avoid all the problems possibly occurring in the original Car-Parrinello method, which is based on the simultaneous integration of electronic and ionic equations of motion. The interaction between ions and electrons is described by ultra-soft Vanderbilt pseudopotential (US-PP) [137] or by the PAW method. Ultra-soft pseudopontentials and projector-augmented wave allow for a considerable reduction of the number of plane waves per atom for transition metals and first row elements. Forces and the full stress tensor can be calculated with VASP and used to relax atoms into their instantaneous ground state. Densities of states are also calculated using VASP code. VASP is based on a program initially written by M. Payne [116] at the MIT. Hence, VASP has same roots as the CASTEP/CETEP code, but branched from this root at very early stage.

DFT calculations were performed with the VASP code, [139,140], within the (GGA) in the form of PBE exchange correlation functional [141]. The number of plane waves was determined by a cutoff kinetic energy of 600 eV and the Brillouin zone sampling scheme of Monkhorst-Pack with 6x6x9 and 6x6x1 k-points mesh for the bulk and surface structures were used, respectively (Convergence graphs). As in previous DFT investigations of MnO_2(R) our calculations are spin polarized, and we approximate the experimentally determined non-collinear helical magnetic structure of β-MnO_2 with AFM type magnetic ordering, which allows this study to be done within the computationally simpler collinear magnetic formalism.

From figure 1 (density of states plotted over the valence electron energy range), we can see clearly that MnO_2 fails to open any gap at the Fermi level using standard PBEsol without extra corrections. However, if we include a static mean field correction through the addition of the ubiquitous “+U” term, which has the

approximate effect of lowering the energy of the occupied bands by U/2 whilst pushing the unoccupied bands up in energy by U/2, a satisfactory gap opens. For all calculations we use Liechtenstein's non-simplified rotationally invariant Hubbard correction with effective Coulomb parameter set U= 2.8 and exchange parameter J=1.2, in accordance with recent calculations by Cockayne and Li.

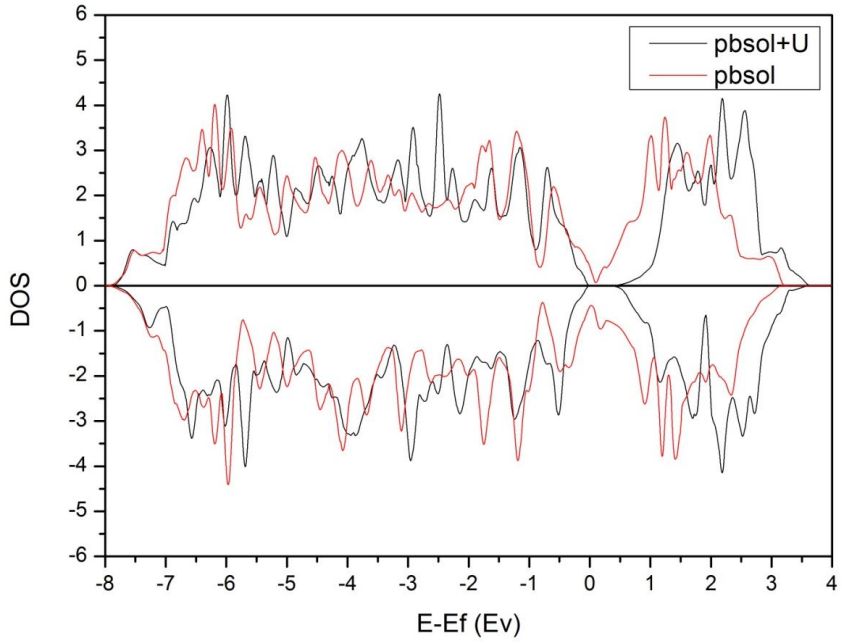

Figure 2.2: Electronic density of states (DOS) for the AFM (antiferromagnetic) MnO_2 bulk (a) without +U Coulomb correction term (red) and (b) with the +U correction (black)

2.5.1 Surface calculations

In surface simulations, all atoms in the slabs were fully relaxed, and the surface energies (Y) are obtained using the standard expression:

$$\gamma = \frac{E_{slab} - E_{bulk}}{2A}, \qquad 2.49$$

where E_{slab} is the energy per slab unit cell, E_{bulk} is the energy of the equivalent amount of bulk solid and A is the surface area.

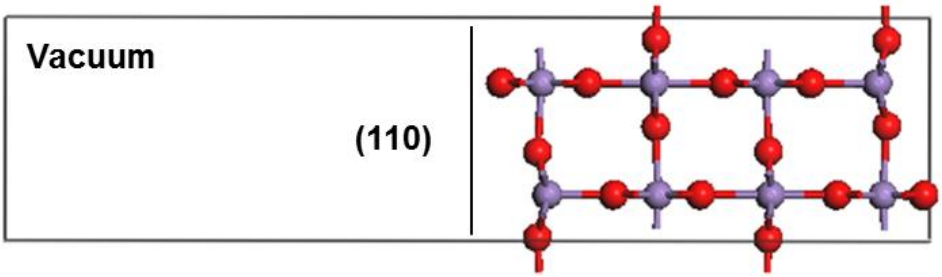

Figure 2.3: Slab model for the 110 surface of β-MnO_2

To further determine the stability of the surface, different composition of the surface has been carried out by adding and removing oxygen atoms from the stoichiometric surface to form a non-stoichiometric composition. In forming the non-stoichiometric surface, symmetrical equivalence has been preserved throughout. Stabilities of the non-stoichiometric surface is based on *ab-initio* thermodynamics introduced by Scheffler *et al*. [142]. Surface free energy was determined using the equation:

$$\sigma(T, p) = \frac{E_{slab} - E_{bulk}}{2} - \frac{\Gamma}{A}\mu_O(T, p), \quad 2.50$$

where

$$\Gamma = \frac{1}{2}(N_O - 2N_{Mn}), \quad 2.51$$

Is the number of extra oxygen on the surface at different composition N_O and N_{Mn} represent the number of O and Mn atoms in the slab. Assuming that the equilibrium with the gas phase is given by

$$\mu_0(T, p) = \frac{1}{2}(E[O_2] + \Delta g_{O2}(T, p_0) + k_B T \ln \frac{p}{p_0}) \quad 2.52$$

thus, chemical potential of oxygen is then expressed. The first term in the brackets is the density functional theory energy of the oxygen molecule, the second term is the difference in Gibbs free energy per oxygen molecule between o K and T at p_0 =1 bar,

the values can be obtained from the thermodynamics table [143] . The last term represents the change in free energy of oxygen gas when pressure changes from p_0 to p at constant temperature T, assuming ideal conditions. In following t the usual convention of expressing oxygen chemical potential with reference to half energy of oxygen molecule is:

$$\mu_0\left(T,\ p\right) = \frac{1}{2}\ (\mathrm{E}[\mathrm{O}_2] \rightarrow \mu_0\left(T,\ p\right), \qquad 2.53$$

thus the chemical potential now becomes independent of calculated quantities. In using this method, it is therefore possible to plot the surface free energy given by equation 2.50 for different surface composition (stoichiometric and non-stoichiometric) as a function of chemical potential and discuss oxidation and reduction of the surface.

Chapter 3: Oxidation and Reduction of MO_2 surfaces

3.1 Introduction

In this chapter, detailed discussions of the results obtained will be covered. Convergence tests for cutoff and k-points are also included in order to justify our choice of parameters. β- MnO_2, TiO_2 and VO_2 surfaces energies (110), (100), (101), (001) and (111) are calculated and compared. Energy results for the bulk, stoichiometric surface and the non-stoichiometric surfaces are discussed. Surface morphology for the three systems is investigated to determine the dominance of each surface and will be represented by the Wulff's construction of the equilibrium morphology. The redox properties are investigated by calculating the relative surface free energies of the non-stoichiometric compositions as a function of oxygen chemical potential. Will Investigate the interaction of the oxygen molecule with the (110) surfaces of MO_2 (M representing MnO_2, TiO_2 and VO_2) is investigated; in particular tendencies of oxygen reduction.

3.2 Convergence test for the energy cutoff and k-point sampling

3.2.1 Cutoff energy

In order to get the correct parameters for β- MO_2 series of calculations were performed in order to validate the cutoff energy. The cutoff energy was varied from 200eV to 900eV. In figures 3.1, 3.2 and 3.2 we show the curve of total energy per atom against cutoff energy, the energy cutoff 500 eV was chosen, since the energy gave a constant slope at that point and they yield energy differences of less than 3.00 meV.

Number of plane waves was determined by a cutoff kinetic energy of 500 eV throughout the study for the bulk structure for the systems. The VO_2 calculations were also performed from a previous study [144] and are in good agreement.

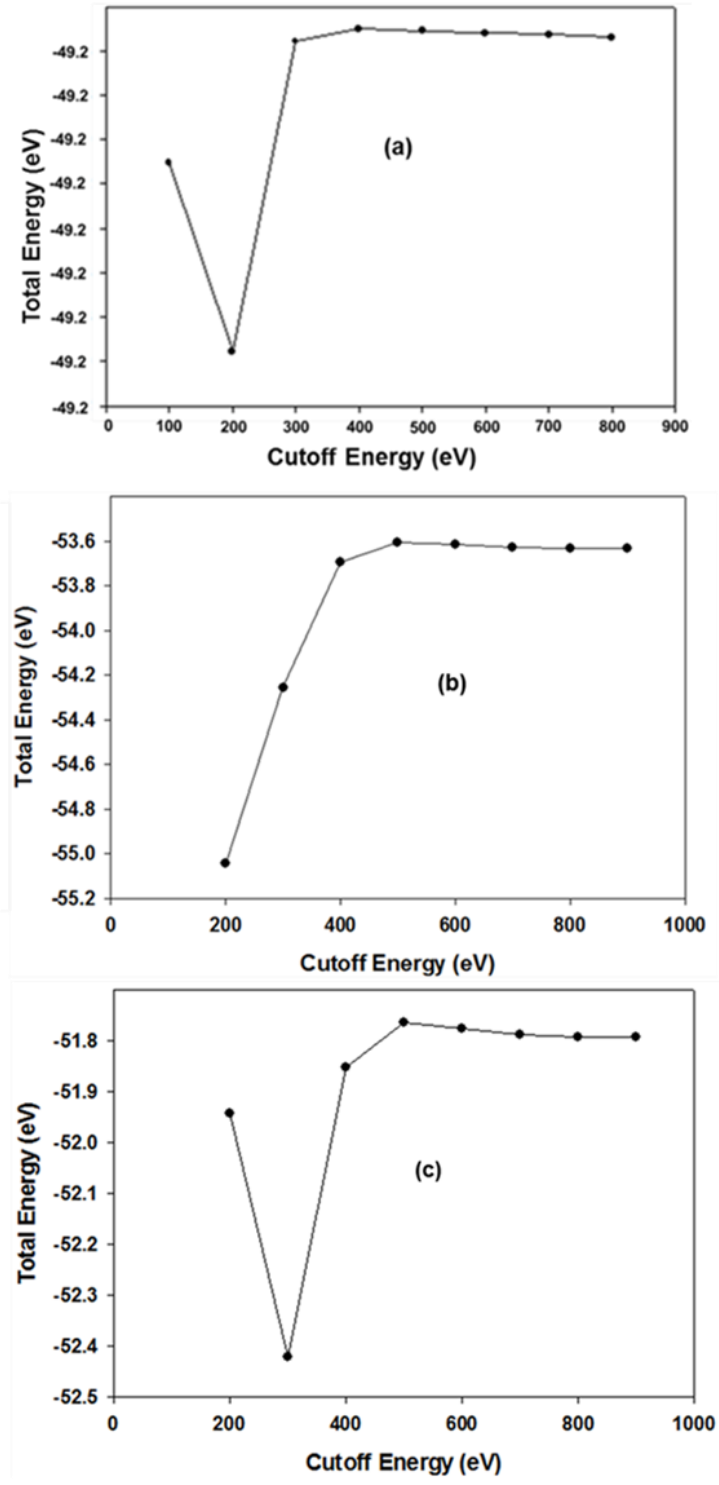

Figure 3.1: The graph of total energy (eV) versus cutoff energy (eV) for (a) MnO_2, (b) TiO_2 and (c) VO_2.

3.2.2 k-points mesh

A series of calculations were carried out in order to validate the k-points mesh which will optimize the total energy of the structures. The k-points at which the Brillouin zone is to be sampled during a self-consistent calculation to find the electronic ground state may be defined either by specifying a list of k-points in terms of the dimensions of the k-point mesh. At 5 k-point (6x6x9) the total energy is already converged to within 1meV/atom as shown in figure 3.4, 3.5 and 3.6 and thus the k mesh that was used to optimize the bulk structures for MnO_2 and TiO_2.

The same cutoff and k-points were used for all systems since the bulk structures converge within the same range of kinetic energy cutoff of 500 eV, and 6 x 6 x 9 mesh of k-points. For surface calculations, the number of k-points was adapted to achieve a similar sampling density in the reciprocal space.

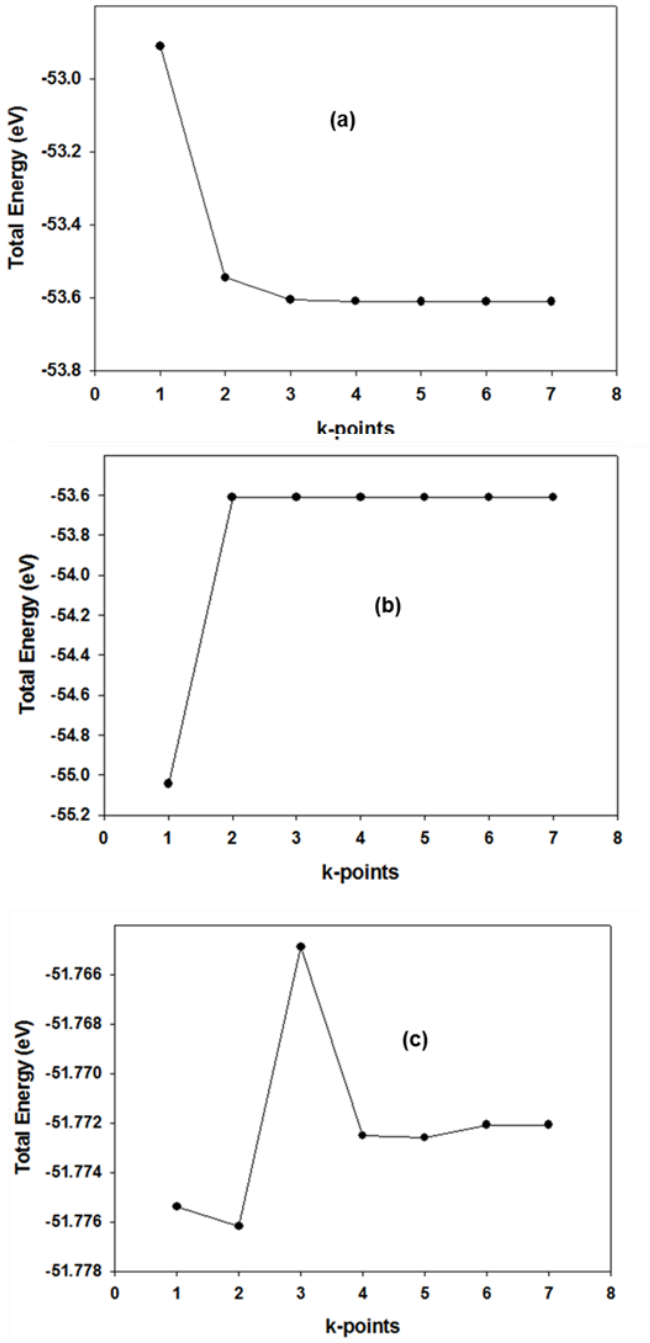

Figure 3.2: The graph of total energy (eV) versus k-points for (a) MnO_2, (b) TiO_2 and (c) VO_2.

3.2 Stability and redox thermodynamics of surfaces

The stabilities of low-index surface orientations ((110), (010), (001), (111) and (011)) of MnO_2, TiO_2 will be deduced by performing periodic calculations of slabs with

stoichiometric composition, thicknesses between 11 and 14 Å (depending on the orientation), and vacuum gaps of ~14 Å as shown in in figures 3.7, 3.8 3.9 respectively. The two surfaces of each slab are symmetrically equivalent and stoichiometric; in order to prevent the formation of electric dipole moment which can be associated with asymmetric slabs. The cell parameters of the surface are kept constant during calculations, based on the relaxed cell parameters of the bulk. Other studies show that MnO_2, TiO_2 and VO_2 have similar trends of surface energies trend of (110)> (010)> (001)> (111)> (011) [144].

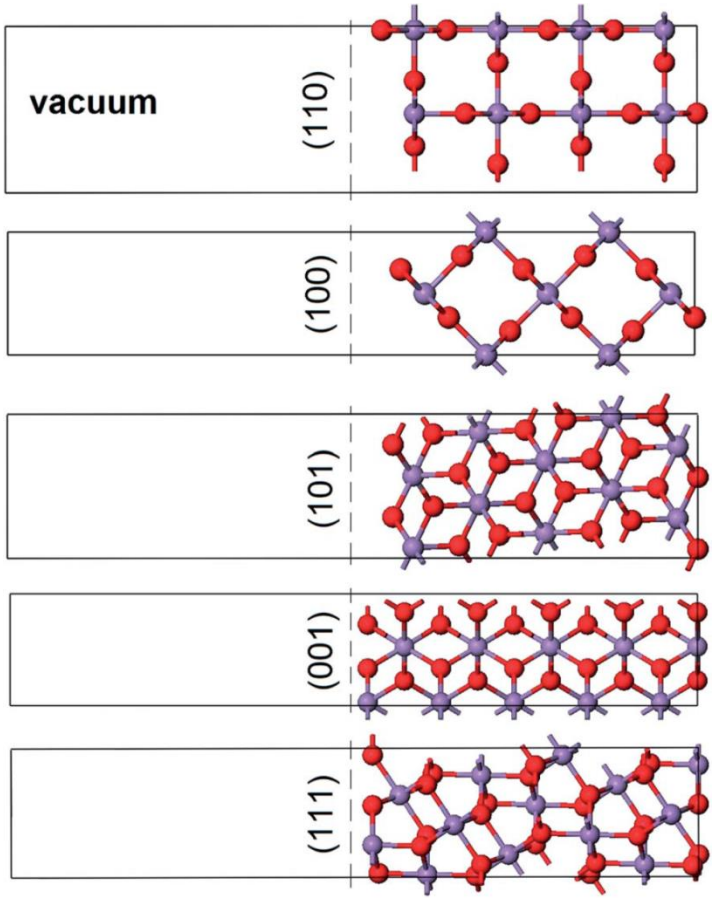

Figure 3.3: Unit cells containing the slabs used for modelling the low-index surfaces of rutile MnO_2.

Calculations are based on the relaxed cell parameters of the bulk. For MnO_2, the calculated unit cell parameters are a = 4.366 Å and c = 2.961 Å, which compare well with experimental values a_{exp} = 4.399 Å A and c_{exp} = 2.872 Å (deviations of -0.8% and +3.1% for a and c, respectively, and of 1.6% in the cell volume).

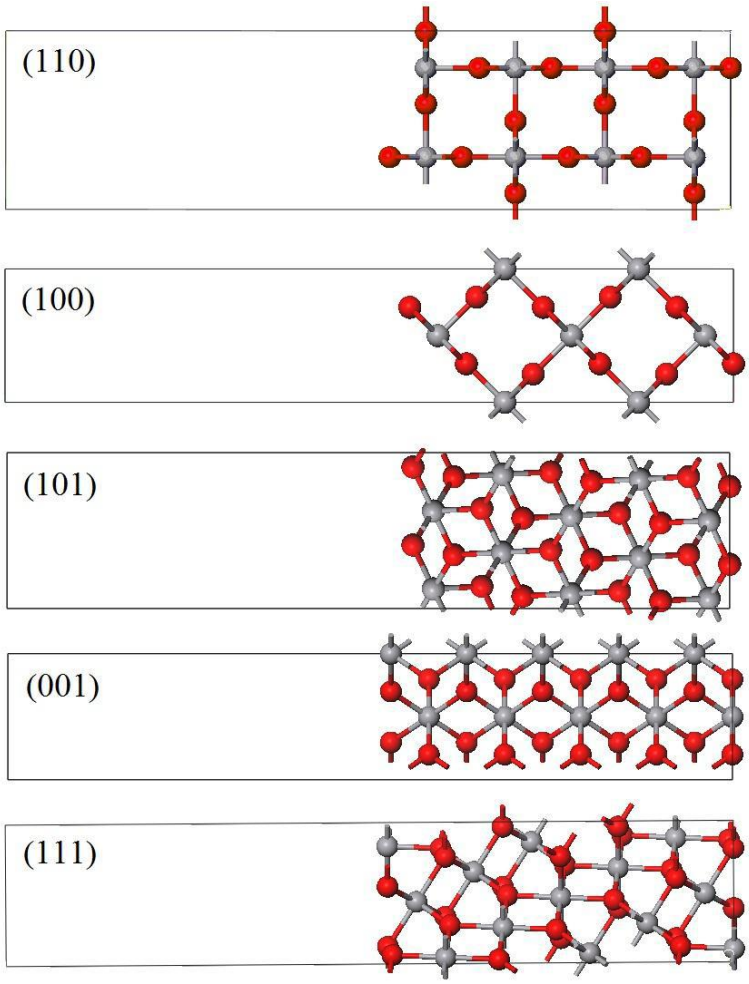

Figure 3.4: Unit cells containing the slabs used for modelling the low-index surfaces of rutile TiO_2.

The cell parameters of the slab are kept constant during the calculations, based on the relaxed cell parameters of the bulk: a= 4.627 Å and c= 3.008 Å, which are in reasonable agreement with experimental values a_{exp}= 4.594 Å and c_{exp}= 2.959 Å

(deviations of +0.8% and -3.1% for a and c, respectively, and of 1.6 % in the cell volume).

The cell parameters of the slab are kept constant during the calculations, based on the relaxed cell parameters of the bulk: a= 4.617Å and c= 2.774Å, which is in reasonable agreement with experimental values a_{exp}= 4.554Å and c_{exp}= 2.857Å (deviations of +1.4% and -2.9% for a and c, respectively, and of -0.1% in the cell volume) [145].

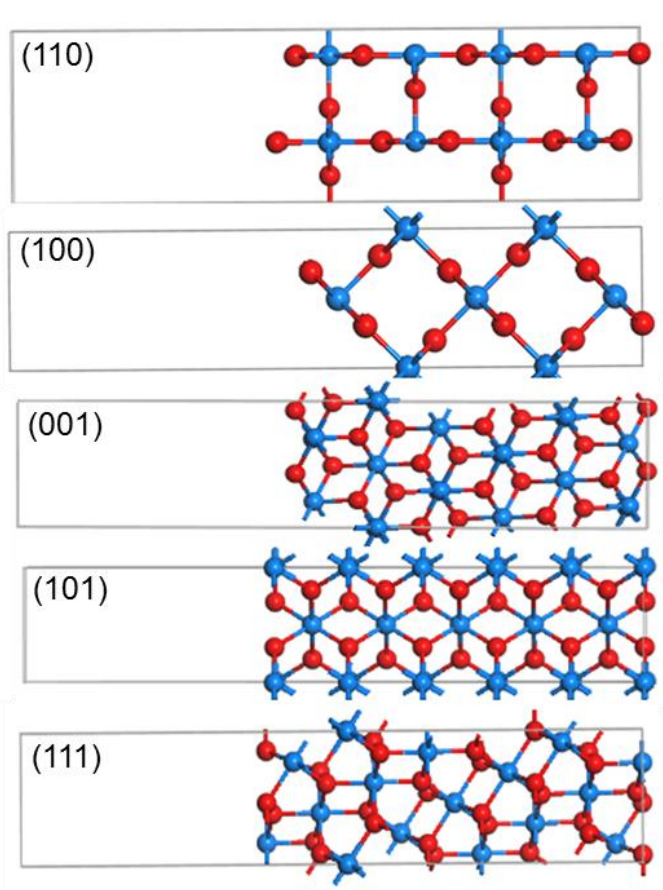

Figure 3.5: Unit cells containing the slabs used for modelling the low-index surfaces of rutile VO_2.

3.3 Surface stability and morphology for pure MnO_2, TiO_2 and VO_2

The surface energies for the five crystallographic planes shown in figure 3.7 and 3.8 are listed in Table 3.1. There is a similar trend in changes of surface energies for all three isostructural transitional metal oxides (MnO_2, TiO_2 and VO_2). The most stable surface is the (110) surface which was calculated using equation 2.49.

Table 3. 1: Surface energy for low miller index β-MO_2 surfaces.

Surface plane	Energy (J/m^2) MnO_2	Energy (J/m^2) TiO_2 [146]	Energy (J/m^2) VO_2 [144]
110	1.15	0.48	0.29
100	1.43	0.67	0.42
101	2.03	1.01	0.75
001	2.20	1.21	0.96
111	3.61	1.46	1.25

These surface energies were used to calculate the planes exposed to the equilibrium morphologies of MnO_2, TiO_2 and VO_2 shown in figure 3.9. The particle volume is largely bounded by the (110) and (101) planes. Morphologies of MnO_2 and TiO_2 show similarities in the reflection of the (100 and 001) planes whereas those of VO_2 shows only (101).

The morphology calculations were performed using metadise code (Minimum Energy Technique Applied to Dislocations, Interfaces and Surfaces Energies). The code has its own minimum energy optimiser based upon interatomic potentials or is well

integrated to use minimum energies calculated by external programs e.g. using Density Functional Theory codes.

Experimentally, the morphologies of the above systems is dependent on the synthesis conditions, but the observed tendency to form particles with large aspect ratio is consistent with the results obtained [147].

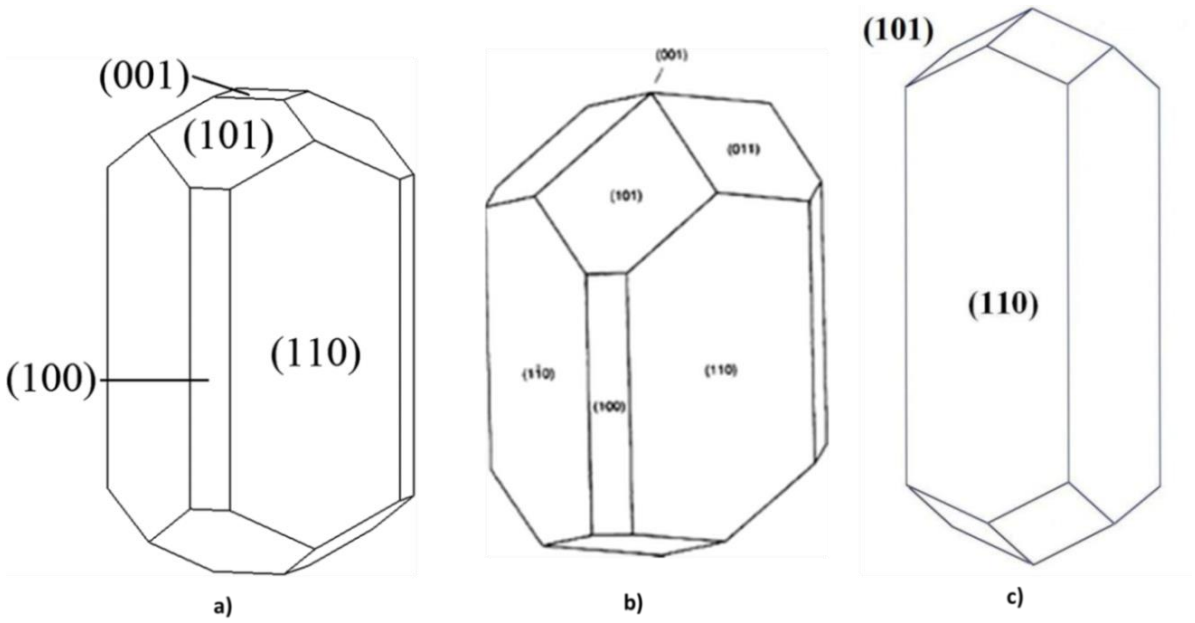

Figure 3.6: Wulff's construction of the equilibrium morphology for a) MnO_2, b) TiO_2 and c) VO_2.

The surface plane of fivefold Mn atoms ends up being ~0.30 Å below the plane of sixfold Mn atoms. This is again similar to the relaxed TiO_2 (110) surface, where the equivalent distance is 0.44 Å, according to low-energy electron diffraction experiments (and 0.39-0.42 Å in theoretical calculations, depending on the method) [147].

The main relaxation in MO_2 occurs perpendicularly to the surface (top view), similarly to TiO_2 and VO_2 as shown in figures 3.11, 3.12 and 3.13 respectively with the

fivefold-coordinated titanium atoms relaxing inward and the sixfold-coordinated titanium atoms and the in-plane oxygen atoms relaxing outward.

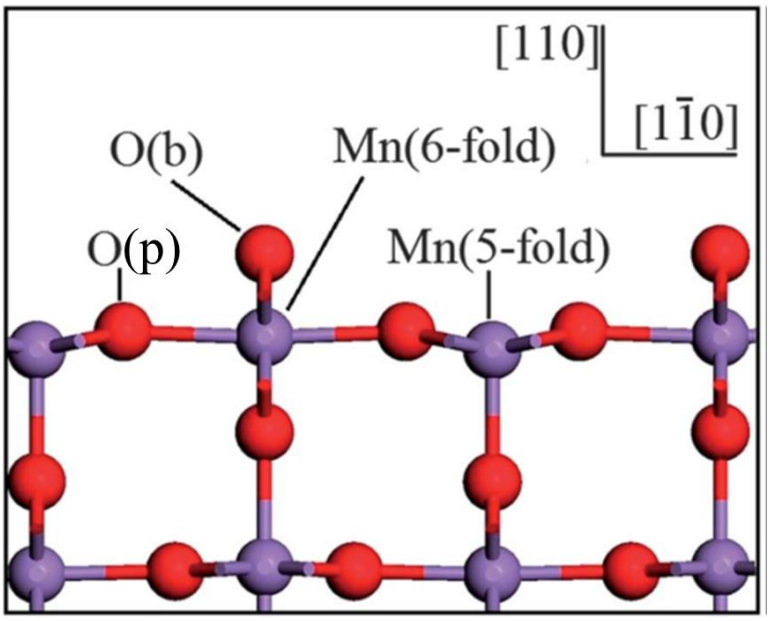

Figure 3.7: Lateral view of the relaxed MnO_2 (110) surface showing the notations for the surface atoms.

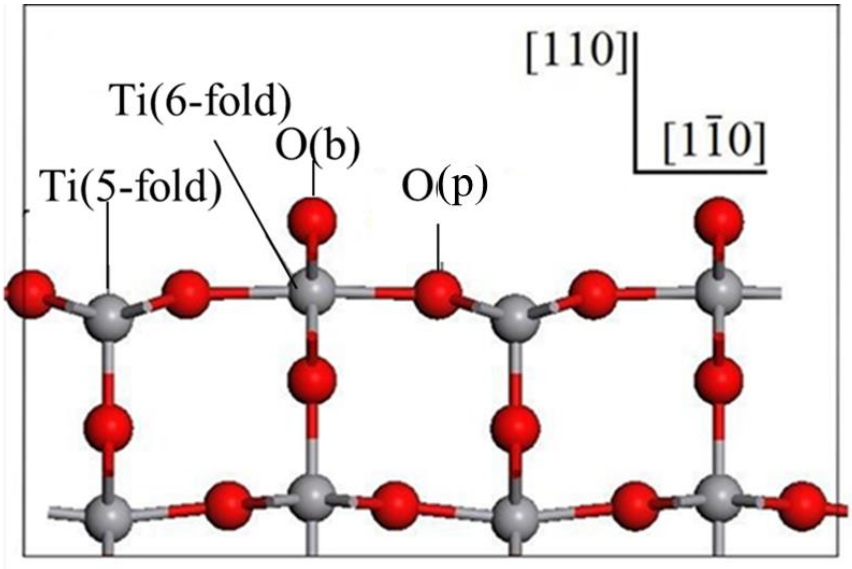

Figure 3.8: Lateral view of the relaxed TiO_2 (110) surface showing the notations for the surface atoms.

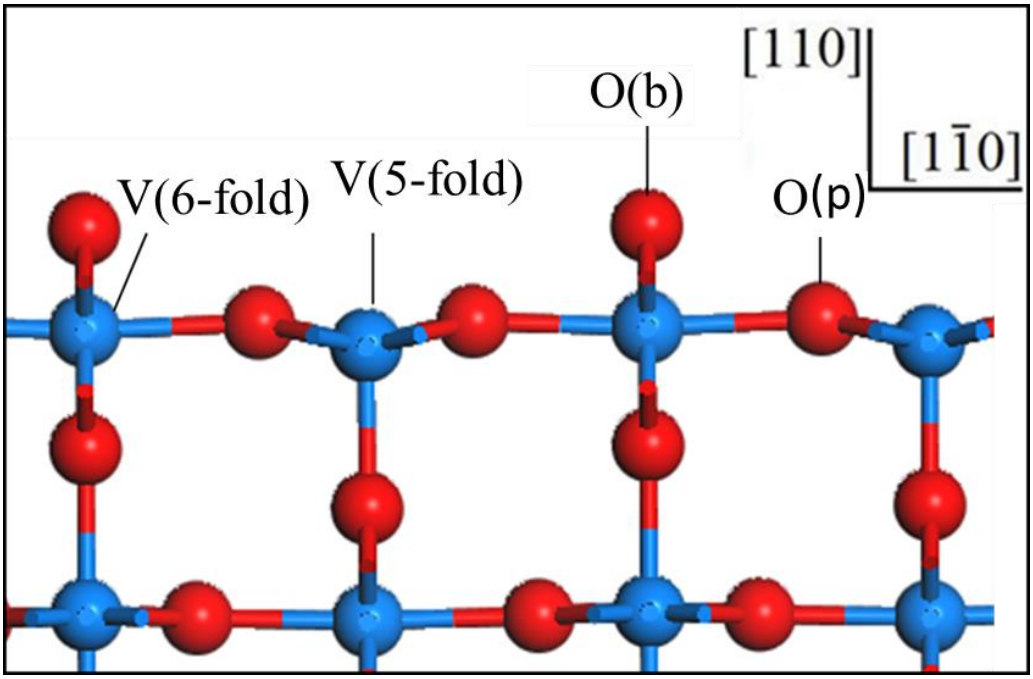

Figure 3.9: Lateral view of the relaxed VO_2 (110) surface showing the notations for the surface atoms.

3.4 Redox properties of pure MnO_2, TiO_2 and VO_2 (110) surfaces

We now discuss the redox properties of the (110) surface for MnO_2, TiO_2 and VO_2 by comparing the surface free energies corresponding to different oxygen to M (Mn, Ti and V) ratios at the surface. The number of M atoms in the slab is kept the same as in the stoichiometric surface, but the number of oxygen atoms at each surface is changed by Γ (given by equation 2.51). Owing to the size of our supercell, and assuming that oxygen atoms occupy bulk-like positions around the surface M atoms, only five values of Γ are possible if we constrain to a maximum of 1 monolayer (ML) of adatoms or vacancies: Γ= 0 surface is the stoichiometric surface, Γ= 1, 2 are the partially and totally oxidised surfaces, and Γ= -1, -2 are the partially and totally reduced surfaces as shown in figure 3.14, 3.15 and 3.16. Total reduction means the removal of the full top layer of bridging oxygen ions, while total oxidation means the

addition of a full layer of oxygen ions forming manganyl-like, titanyl and vanadyl terminations on top of the previously unsaturated M sites. Mono-peroxo" and "bridging-peroxo" (2(b) and 2(c)) modes of O_2 adsorption, where the molecule remains undissociated, are also considered, and these situations will be compared to the Γ= 2(a) manganyl, titanyl and vanadyl bulk-like termination. Intermediate degrees of oxidation and reduction could be also investigated by using a larger supercell and a configurational analysis of the distribution of excess oxygen/vacancies in order to get a more quantitative picture of the redox behavior, but we will see that the present "coarse-grained" picture already provides very useful information.

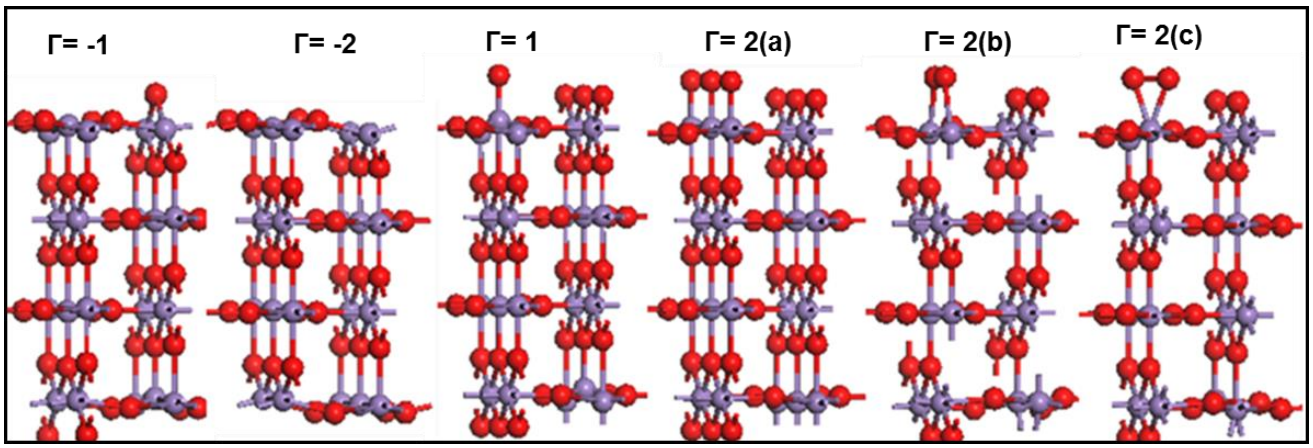

Figure 3.10: MnO_2 (110) with different amounts of surface oxygen. Γ = -1, -2 are the partially and totally reduced surfaces; Γ = 1, 2 are the partially and totally oxidised surfaces; the bridging and mononuclear peroxo compositions.

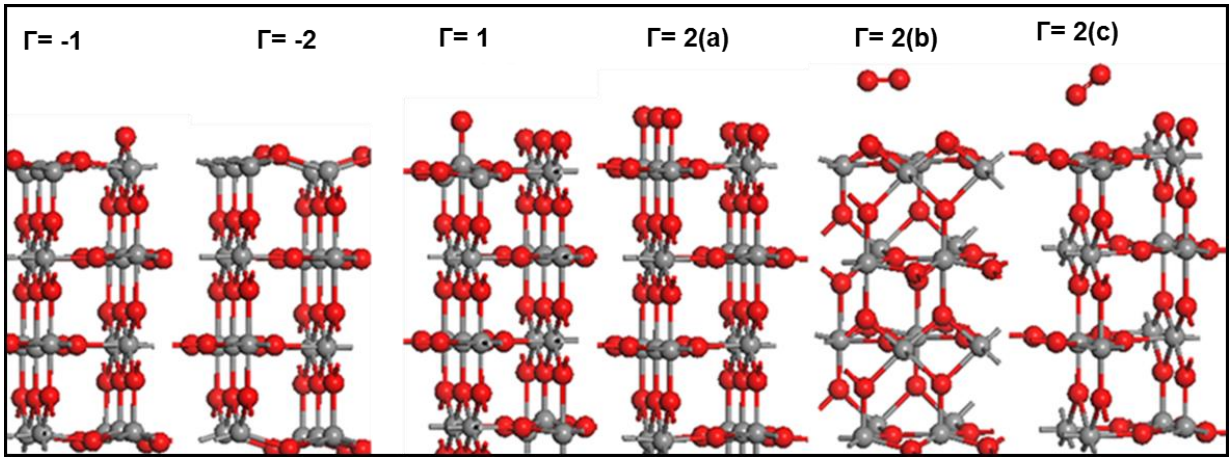

Figure 3.11: TiO_2 (110) with different amounts of surface oxygen. Γ = -1, -2 are the partially and totally reduced surfaces; Γ = 1, 2 are the partially and totally oxidised surfaces; the bridging and mononuclear peroxo compositions.

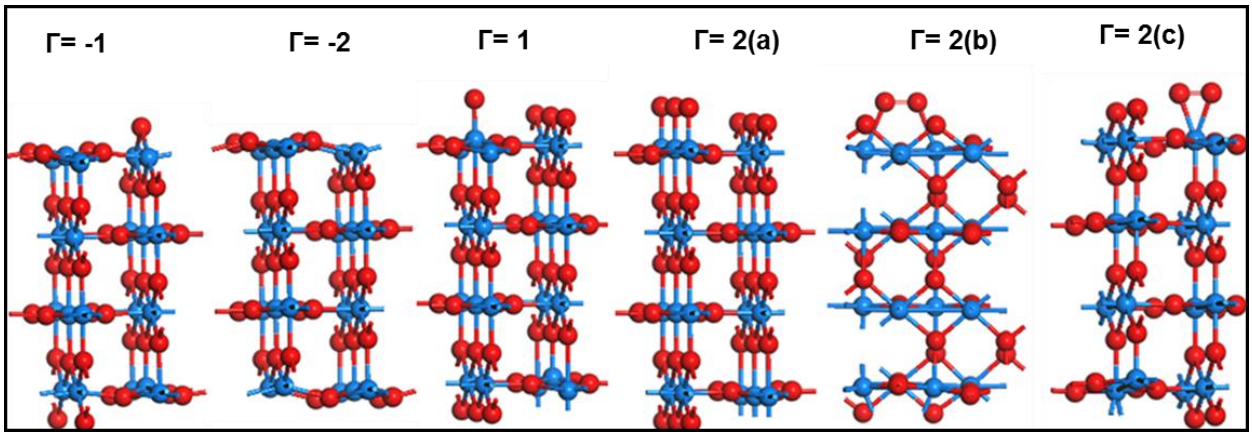

Figure 3.12: VO_2 (110) with different amounts of surface oxygen. Γ = -1, -2 are the partially and totally reduced surfaces; Γ = 1, 2 are the partially and totally oxidised surfaces; the bridging and mononuclear peroxo compositions.

From the above figures 3.14, 3.15 and 3.16 the similarities between the three metal oxides is the compositions for Γ = -1, -2 and Γ = 1, 2 all systems relax in a similar way maintaining the same morphology. The manganyl, titanyl and the vanadyl-

terminated surface is not the only surface that can be formed with Γ=+2. Oxygen can be adsorbed also as peroxo species $(O_2)^{2-}$, with less electron transfer from the surface metal (M) atoms to the adatoms than in the case of manganyl, titanyl and vanadyl formation. For vanadium dioxide the redox surface study behaves very similarly with MnO_2 and TiO_2 [144]. The presence of peroxo species has been investigated for other oxide surfaces, e.g. in the surfaces of alkaline-earth oxides [149].

The difference observed here is whether the oxygen molecules for the (bridging and mononuclear) perexo species adsorb on the surface or not. The oxygen molecule does adsorb to the surface Mn and V atoms for both peroxo species while the molecule floats on the surface for TiO_2 surface. The mononuclear peroxo species for TiO_2 disorientate the molecule from how it was initially place before relaxation, the molecule tilted for ~ 66^O which implies that TiO_2 has a special orientation for O_2 especially when the molecule is bonded to one Ti surface atom.

Table 3. 2: Table showing the bond lengths for the adsorbed oxygen and surface metal of the systems after relaxation

Bond	Bond length (after) (Å)		
Metal Oxide	MnO_2	TiO_2	VO_2 [144]
Γ= 2	1.63 (O-Mn)	1.60 (O-Ti)	1.610 (O-V)
Bridging	1.286 (O-O) 2.063 (O-Mn)	1.271 (O-O) 2.108 (O-Ti)	1.350 (O-O) 1.910 (O-V)
Mono-nuclear	1.308 (O-O) 1.899 (O-Mn)	1.227 (O-O) 1.899 (O-Ti)	1.410 (O-O) 1.820 (O-V)

There is a tendency of oxygen reduction in the systems the oxygen molecule was adsorbed in all three metal oxides; this is due to the bond length increase on oxygen molecule. Oxygen molecule bond length increases as captured in table 3.2 regardless of the orientation of the molecule but the mono-nuclear orientation shows more increase in the bond length of O_2 molecule. The bond length of the metal Ti to the adsorbed oxygen is larger those of surface Mn and V atoms, which supports what has been observed in figure 3.15 where the oxygen molecules are floating rather than adsorbing on the surface, hence the positive adsorption energies.

To correct for the poor PBEsol description of redox enthalpies, we adjusted the value of oxygen molecule energy, similar to the correction proposed by Wang *et al.* [150]. The value is determined such that when the PBEsol calculated energies for a number of metal oxide bulk are used to determine enthalpies of formation shown in figure 3.17. The correction in the case of MnO_2, TiO_2 and VO_2 should improve the poor description of molecules by PBEsol functional compared to standard PBE.

Now, we discuss the thermodynamics of surface reduction/oxidation as a function of temperature and oxygen partial pressure. Figure 3.14 - 3.16 show the variations of the surface free energies for different compositions with the chemical potential for MnO_2, TiO_2 and VO_2 respectively. The chemical potential is plotted in terms of temperature and partial pressure of O_2 in the graphs below, and given along abscissas for easy comparison with the top plot.

To put these chemical potentials in context, we draw a vertical line at the value below which bulk MnO_2 becomes stable with respect to bulk Mn_2O_3. This is approximately equal to the enthalpy of the reaction:

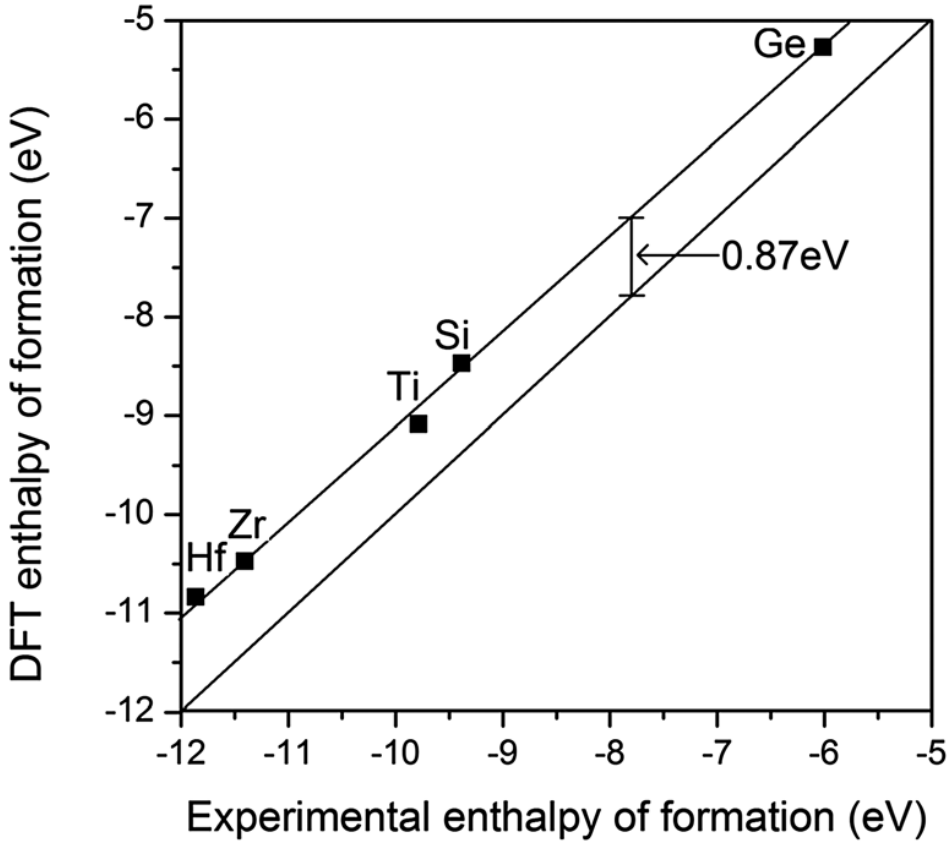

Figure 3.13: Effect of the correction (0.87 eV) required for the PBEsol O_2 energy to match the experimental values of oxide formation energies.

$$2Mn_2O_3 + O_2 \rightarrow 4MnO_2 \quad (3.1)$$

$$2Ti_2O_3 + O_2 \rightarrow 4TiO_2 \quad (3.2)$$

$$2VO_2 + 1/2O_2 \rightarrow V_2O_5 \quad (3.3)$$

ΔH= -1.68 eV*, ΔH*= -1.36 eV *and ΔH*= -1.36 eV; for MnO_2, TiO_2 and VO_2 respectively which we obtained from the experimental formation energies of the three metal oxides [151-153]. At the chemical potential $\mu_O=\Delta H$, the free energy of the above reaction changes sign (we are neglecting here the small contributions from the variation of enthalpies with temperature and from the difference in entropy between

the two oxides). The area to the left of the vertical line in the chemical potential plots, figure 3.17-3.19, thus corresponds to the conditions under which bulk Mn_2O_3 Ti_2O_3 and $V_2O_5$is thermodynamically stable with respect to bulk MnO_2, TiO_2 and VO_2. Under ambient conditions, for example, MnO_2, TiO_2 and V_2O_5 are the stable bulk phases.

Fig. 3.17 shows that the two reduced terminations, considered Γ = -2 and -1 are not stable under moderate T and p conditions. Complete reduction of the MnO_2 surface is not feasible for extremely reducing conditions where bulk Mn_2O_3 is more stable than bulk MnO_2 (*i.e.* the left of the vertical line in figure 3.13). Under mildly reducing conditions (approximately -1.7eV < μo < -0.6 eV) the Γ = 0 stoichiometry is always the most stable. Under oxidising conditions (lower temperatures and/or high oxygen partial pressures), although Γ = 1 oxidation is unfavourable, the specific bridging-peroxo Γ = 2 mode of oxidation is stable. The stoichiometric composition, moreover, becomes unstable with respect to the bridging-peroxo mode of Γ = 2 oxidation at approximately ambient temperature and pressure. The general trend towards a stoichiometric surface, or a surface with adsorbed oxygen, is consistent with the presence of some Mn^{5+} ions at the surface of MnO_2 films. XPS of MnO_2 microstructures gives a Mn to O ratio of 1: 2.12, which is evidence for a moderate oxidation of the oxide surfaces [154].

Other recent theoretical investigations present similar trends in oxidation/reduction, although with less stabilisation of surface oxidation [155]. This observation may be due to not considering the adsorption of the bridging peroxo where the adsorbate maintains its molecular form.

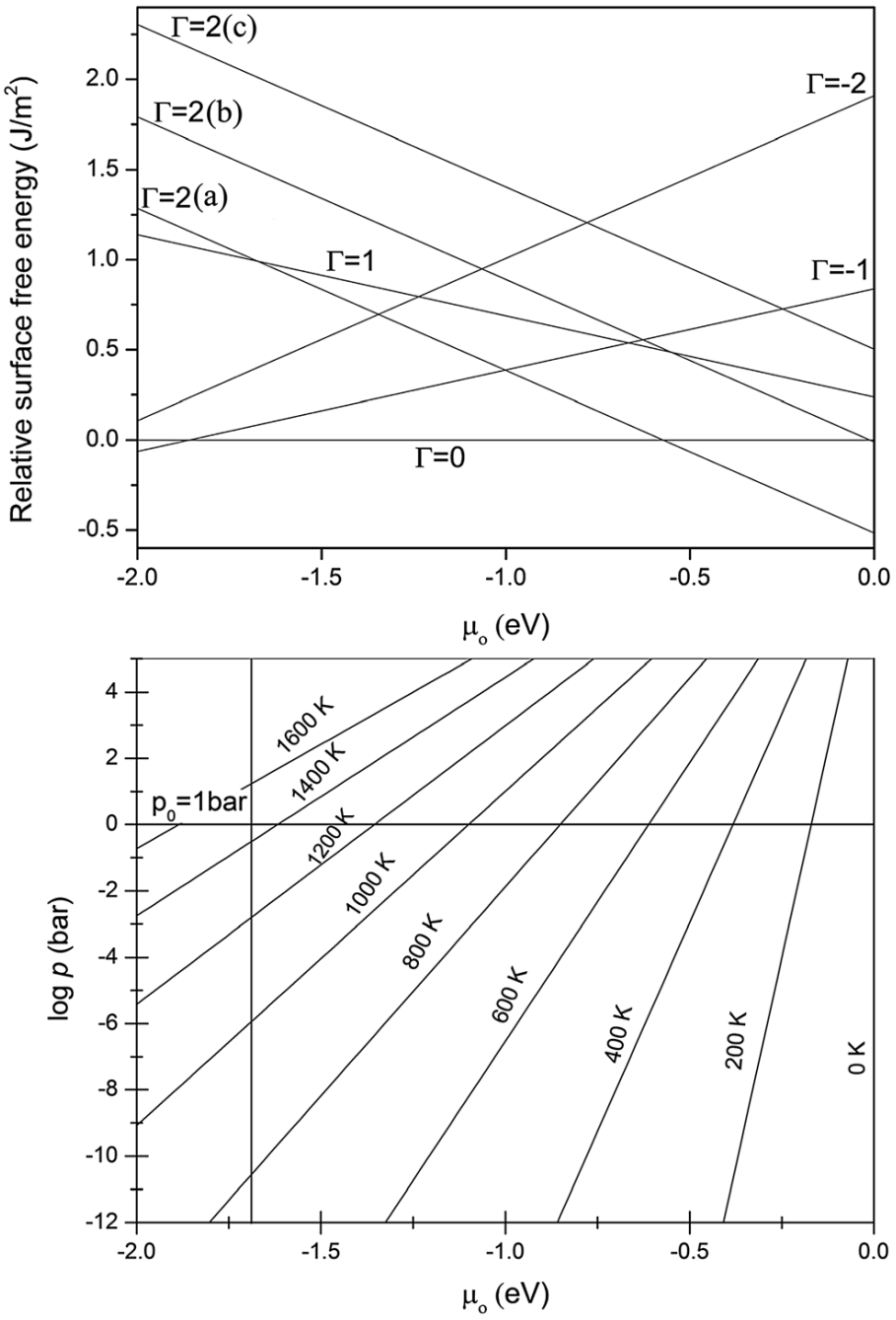

Figure 3.14: Top: relative surface free energies for different compositions of the MnO_2 surface as a function of oxygen chemical potential. The label (a), (b) and (c) for the Γ= 2 lines refer different configuration of adsorbed oxygen; bridging peroxo, mono-nuclear peroxo and manganyl, respectively. Bottom: chemical potential of oxygen in the gas phase as a function of temperature and oxygen partial pressure.

Reduction of the surface, which involves removing oxygen from the surface hence creating a partially reduced surface and further removing the second oxygen (totally reduced surface figure 3.14) is discussed by calculating vacancy formation energy (VFE).

$$E_{\text{vac}} = \frac{1}{2}(E[\mathrm{O}_2] = E[\Gamma = -1] - E[\Gamma = 0]) \quad 3.4$$

Vacancy formation energies were calculated using equation 3.4 from the energies of the Γ = -1 and Γ = -2 slabs. Bridging O vacancies have a formation energy of 1.87 eV, while it requires 4.25 eV to remove both bridging oxygen atoms, that is, reduction becomes more difficult with the removal of each bridging O (4.25/2 eV > 1.87 eV).

Adsorption energy was also calculated for the configurations outlined in figure 3.14. The following equation was used for the calculation of adsorption energy.

$$E_{\text{ads}} = \frac{1}{2}\,(E[\Gamma = \ +1] - E[\Gamma = 0] - E[\mathrm{O}_2]) \quad 3.5$$

The adsorption of an oxygen atom on a 5-fold coordinated Mn site yields the adsorption energy of 0.53 eV. The configuration where the oxygen added goes to the fivefold Mn, forming a manganyl species with Γ= 2, this configuration, there is enhanced electron transfer from the manganese atom to the adatom. The calculated adsorption energy of this configuration is +1.16 eV, which implies that oxidation of the -surface, is thermodynamically unfavourable. We further adsorbed oxygen as peroxo species $(O_2)^{-2}$, with less electron transfer from the surface manganese atom. For the mono-nuclear peroxo where an oxygen molecule is coordinated to one manganese surface atom and the bridging configuration, an oxygen molecule is coordinated to two Mn atoms forming a bridge shown in figure 3.14; the mononuclear configuration gives the adsorption energy of - 0.02 eV and the bridging configuration

gives -1.15 eV. The formation of manganyl species from adsorbed oxygen is a local minimum in the adsorption energy landscape, but is the least favourable configuration and is indeed thermodynamically unfavourable with respect to desorption. The bridging peroxo unit is probably the most favored because it is shared between two Mn surface cations and requires the least charge transfer per Mn cation of all possible oxidised species. Minimal charge transfer from Mn to O occurs as the Mn cations have already a formal oxidation state of +4 in MnO_2.

We now discuss the redox properties of the (110) surface of TiO_2, by comparing the surface free energies corresponding to different oxygen to manganese ratios at the surface. The number of titanium atoms in the slab is kept the same as in the stoichiometric surface, but the number of oxygen atoms at each surface is varied by Γ (shown in equation (2.51)). Owing to the size of our supercell, and assuming that oxygen atoms occupy bulk-like positions around the surface titanium atoms, only five values of Γ are possible if we constraint to a maximum of 1 monolayer (ML) of adatoms or vacancies: Γ= 0 surface is the stoichiometric surface, Γ= 1, 2 are the partially and totally oxidised surfaces, and Γ= -1, -2 are the partially and totally reduced surfaces shown in figure 4.5.

Oxygen positions other than the bulk-like sites will be considered in the case of the fully oxidised surface (i.e., “mono-nuclear peroxo, and bridging peroxo”). The peroxo group (mono-nuclear) is the type of peroxo coordinated to one Ti atom and peroxo group bridging between two Ti atoms. Reduction of the surface which involves removing oxygen from the surface creating a partially reduced surface and further removing the second oxygen (totally reduced surface) figure 4.5 is discussed by calculating vacancy formation energy (VFE).

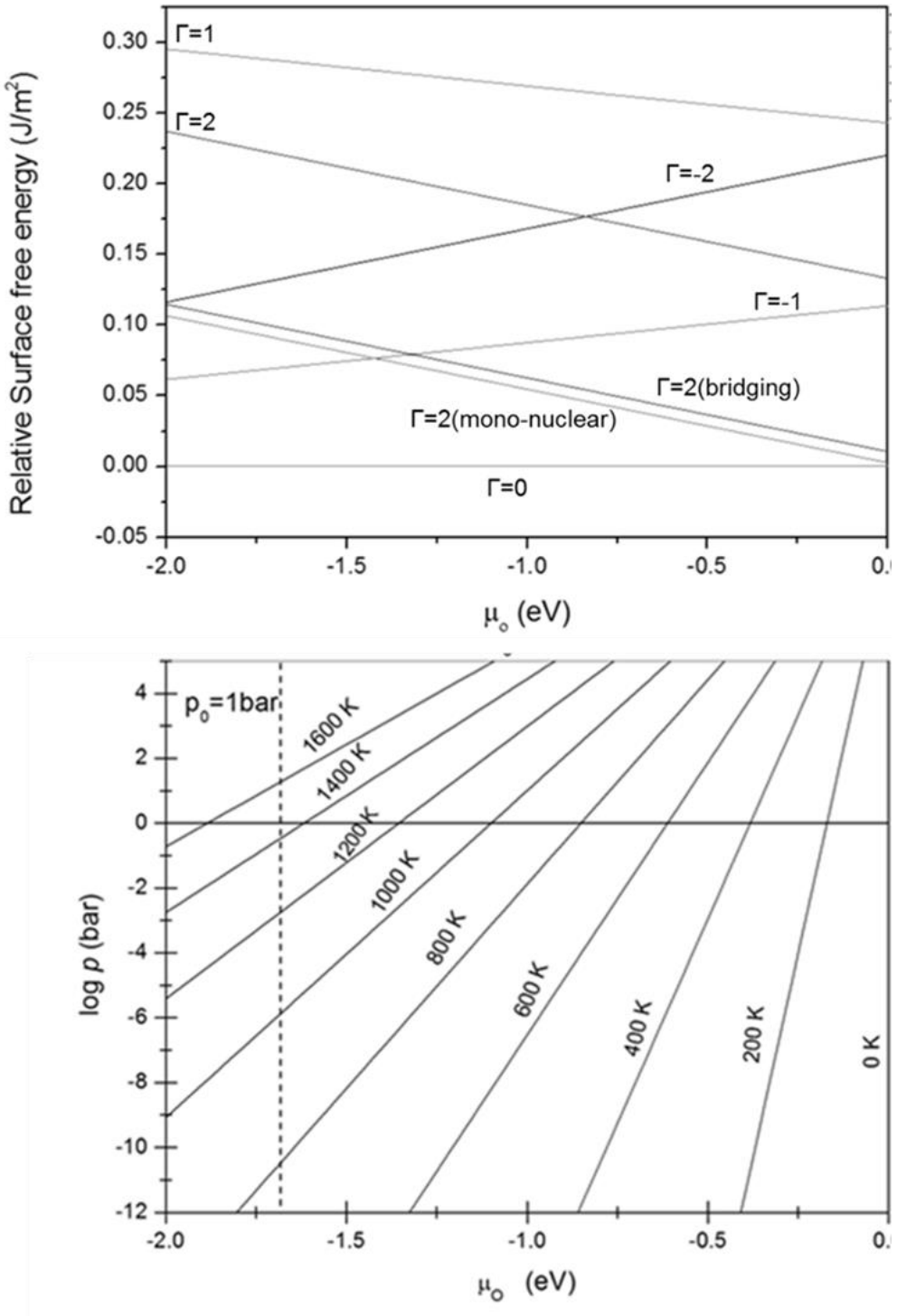

Figure 3.15: Top: Relative surface free energies for different surface terminations of the TiO_2 surface as a function of oxygen chemical potential. The labels Γ=2 (bridging and mononuclear) are the peroxo groups. Bottom: chemical potential of oxygen in the gas phase as a function of temperature and oxygen partial pressure.

Vacancy formation energies were calculated using equation 3.4 from the energies of the Γ = -1 and Γ = -2 slabs. Bridging O vacancies have formation energy of 3.89 eV; while it required 4.39 eV to remove both bridging oxygen atoms, that is, reduction becomes more difficult with the removal of each bridging O. This shows that it is more difficult to remove two bridging oxygen atoms and less energy is needed to remove one bridging oxygen atom [155]. This shows that the in-plane vacancies are created after the bridging oxygen atoms are totally removed from the surface [156-159].

The Oxygen molecule prefers to be adsorbed in a horizontal style (with its molecular axis parallel to the surface and perpendicular to the bridge oxygen row). This geometry was predicted by many theoretical calculations [31,160-163] and was confirmed by recent STM experiments [156,164]. Adsorption energy was also calculated using equation 3.5 for the configurations outlined in figure 3.15.

Adsorption of an oxygen atom on a 5-fold coordinated Ti site (Γ= 1) yielded adsorption energy of 2.41eV. The configuration with Γ= 2 has more electron transfer from the titanium atom to the adatom compared to other configurations. The calculated adsorption energy obtained in this configuration is 0.69eV and implies that oxidation of the surface has undergone an endothermic process hence it is thermodynamically unfavourable. We further adsorbed oxygen as bridging-peroxo unit (O_2^{2-}), shared between two Ti surface cations, which requires the least charge transfer per Ti cation of all oxidation possibilities. The mono-nuclear configuration gives the adsorption energy of 0.070eV and the bridging configuration gives 0.37V, these values show that the processes are endothermic which implies a non-spontaneous process. The mono-nuclear configuration is the most stable of the other two configurations in terms of energy. Adsorption energies are endothermic,

regardless of whether oxygen maintains its molecular character on the surface or not.

We first discuss the reduced surfaces. Removing one oxygen atom at each surface of the slab, leads to the surface with Γ=-1(0.5 ML of oxygen vacancies). The vacancy formation energy, calculated using equation 3.6 is 3.33 eV (3.85 eV after correction) for the bridging oxygen vacancies and 4.30 eV (4.83 eV after correction) for the in-plane oxygen vacancies. These values are very similar to those reported in GGA calculations of oxygen vacancies in the TiO_2 (110) surface [157-159]. The vacancy formation in the VO_2 bulk is 3.00 eV (3.53 eV after correction), which suggest that any surface vacancies will tend to migrate towards the bulk. This contrasts with TiO_2 rutile, where vacancies are significantly easier to create in the (110) surface (in bridging positions) than in the bulk [155]. Removing the rest of the bridging oxygen atoms from the partially reduced VO_2 (110) surface, forming the surface with Γ=-2, takes much more energy per vacancy (4.07 eV, or 4.60 eV after correction) than removing the first bridging oxygen atoms, but still less than removing in-plane oxygen atoms.

This indicates that in-plane oxygen vacancies are only created after all the bridging oxygen atoms have been removed from the surface. On the other hand, the adsorption of one oxygen atom at the surface, leading to 0.5 ML of adatoms (Γ=+1), involves the energy per adatom, which is -1.58eV (-2.10eV after correction). We are assuming here that each oxygen adatom goes on top of a fivefold coordinated V atom, forming a vanadyl species; other configurations will be discussed below.

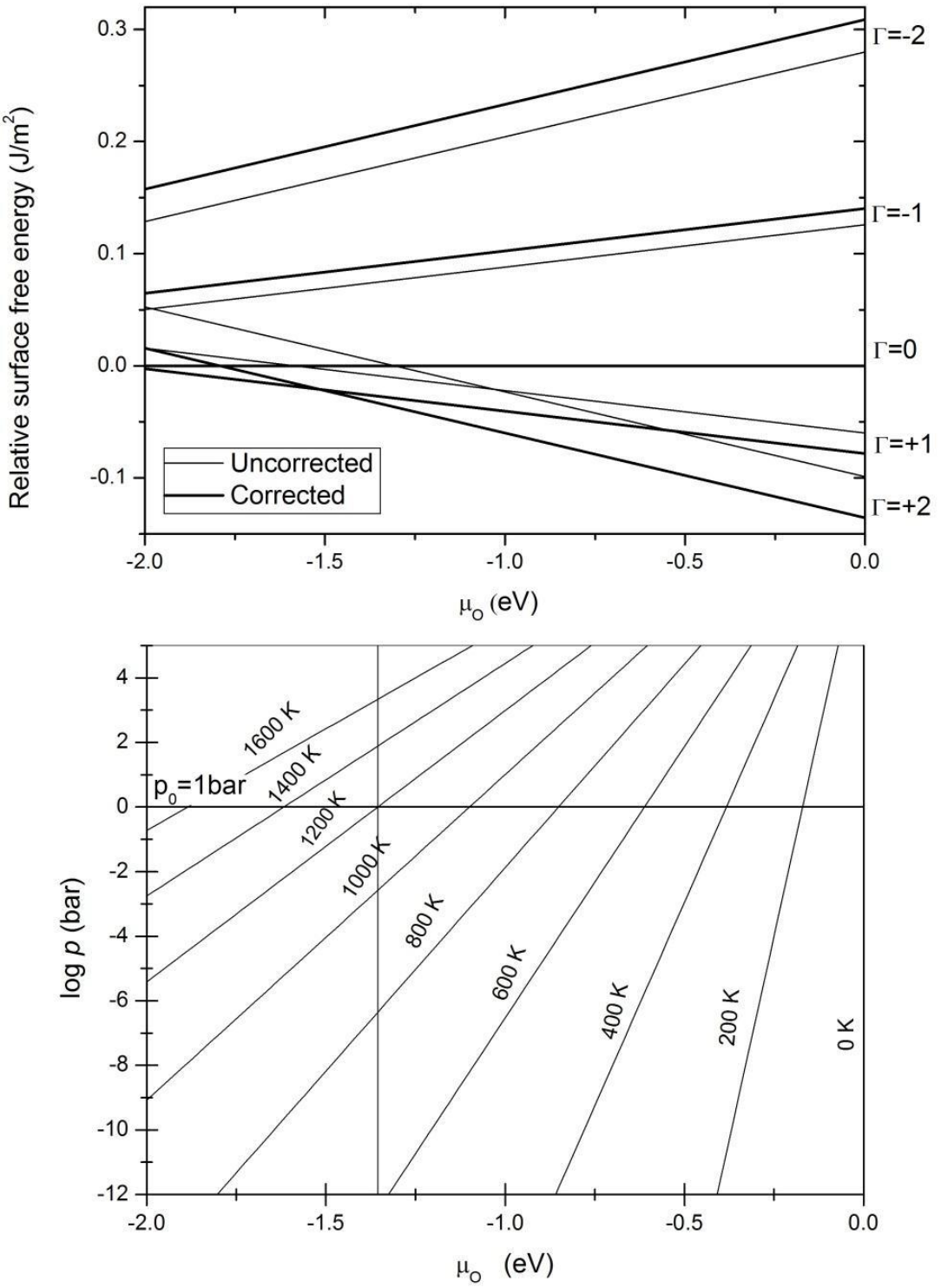

Figure 3.16: Top: relative surface free energies for different compositions of the VO_2 (110) surface as a function of oxygen chemical potential. Bottom: chemical potential of oxygen in the gas phase as a function of temperature and oxygen partial pressure.

The fact that oxygen adsorption from the gas phase is strongly exothermic already suggests that surface oxidation will be thermodynamically favourable, but a complete analysis requires consideration of the gas partial pressure in equilibrium with the surface. Completing 1 ML of vanadyl species (forming a surface with Γ=+2, from the surface with Γ=+1) is also an exothermic process, involving -1.03 eV (-1.56 eV after correction) per adatom. The above discussions for the redox properties were performed by Grau-Crespo *et al.* [144].

Chapter 4: Lithium and oxygen adsorption and co-adsorption on MO_2 surfaces

4.1 Introduction

In this chapter we discuss Li adsorption on the three metal oxides MO_2 (MnO_2, TiO_2 and VO_2) surfaces. It is important to understand charge transfer reactions that produce the potential difference in the battery from the Li adatom to the surface M (Mn, Ti and V) in order to have lithium-air batteries that are productive. Oxidation on the lithiated surfaces will be discussed where different and stable orientations will be studied, in order to observe the most stable orientation. We calculated the surface free energies for the most stable composition for the oxidation on the lithiated surfaces of the metal oxides (MnO_2, TiO_2 and VO_2).

4.2 Charge transfer from lithium adatom to the surface metal (M) cation

Understanding the surface behaviour of Li-doped MO_2 is important in the context of MO_2-based Li–air batteries. We now consider the mode of the transfer of an electron from a Li adatom to a surface M cation using bader analysis. The first step is to determine onto which surface site Li preferentially adsorbs. Different possible adsorption sites on the surface were systematically tested and the results are reported in Table 4.1. We find that Li adatoms are more stable in sites of high oxygen coordination. The site with lowest adsorption energy (-1.80 eV) is where Li is triply coordinated, bonded to two bridging and one in-plane oxygen atoms (bbi) for MnO_2, (-3.16 eV) for TiO_2 which is at high oxygen coordination and (-5.8 eV) for VO_2 at high oxygen coordination. Another adsorption site, with almost the same

adsorption energy, has Li coordinated to one bridging and two in-plane oxygen atoms (bpp). Sites with Li bonded to only two bridging oxygen (bb), or to one bridging oxygen (b) do not correspond to local minima of the potential energy landscape and can only be stabilised by symmetry constraints. Although the bbp position can provide the most stable configuration, within a specific site this depends strongly on where the electron given up by lithium is initially and finally localised.

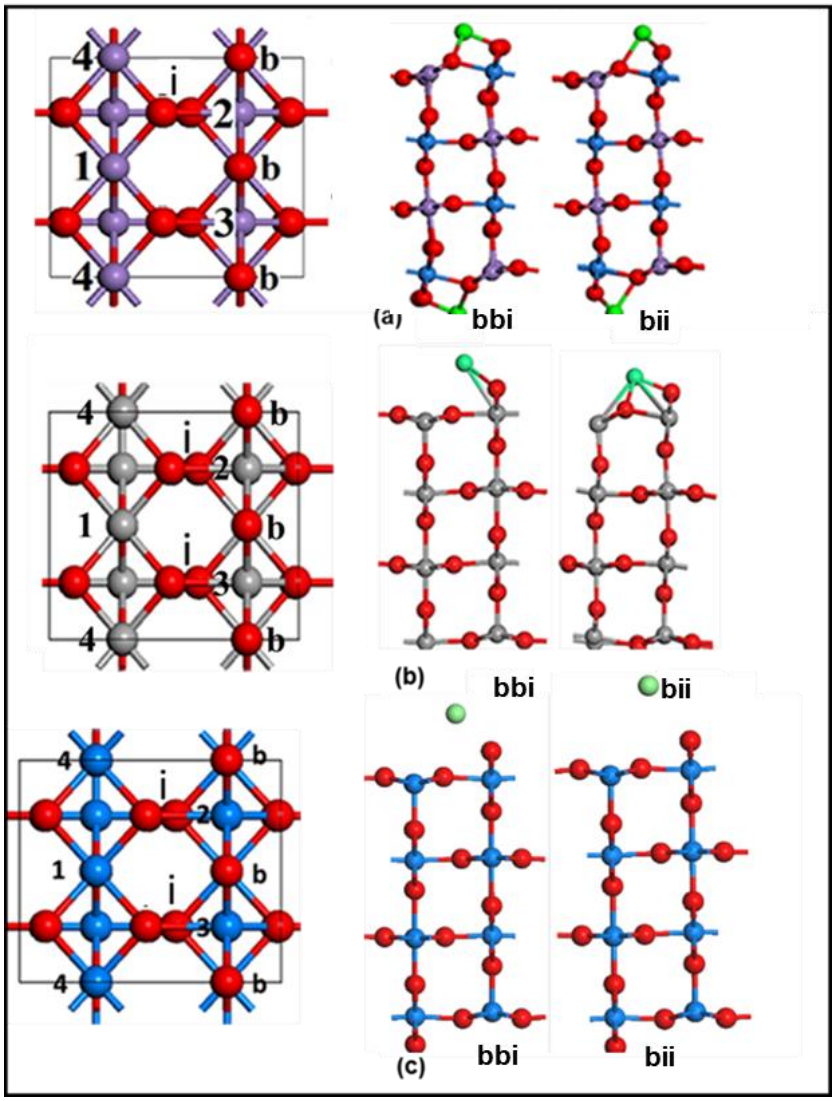

Figure 4.1: (Left to right) 'Bird's eye' view of stoichiometric (110) MO_2 surface with in-plane (i) and bridging (b) oxygens lettered and electron localisation sites numbered; lithium adsorption on relaxed (a) MnO_2, (b) TiO_2 and (c) VO_2 (110) surface.

Table 4. 1: Bader analysis for MO_2 surface with Li in the bbi position; O atoms are not considered.

Species	bbi (eV)	bbi μ ($_B$)	bbi (eV)	bbi (μ_B)
	Initial		Final	
Fe-M	5.358	3.569	5.227	-2.663
M	5.267	2.742	5.308	3.219
M	5.210	2.627	5.308	3.219
M	5.210	2.627	5.308	3.219
Li	0.122	-0.001	0.122	-0.001

Table 4. 2: Bader analysis for MO_2 surface with Li in the bii position; O atoms are not considered.

Species	bii (eV)	bii ($_B\mu$)	bii (eV)	bii (μ_B)
	Initial		Final	
Fe-M	5.383	3.527	5.337	3.618
M	5.269	2.773	5.294	2.715
M	5.213	2.630	5.210	2.644
M	5.213	2.630	5.294	2.715
Li	0.121	0.0007	0.125	-0.0003

The presented orientations are the stable orientations and the other unstable (relative to the adsorption energy landscape) are not shown in figure 4.1. In the case of lithium adsorption on VO_2, the Li atom moves very closer to the surface cation, thus the adsorption energies for VO_2 are much more negative than in TiO_2 and MnO_2. The bbi orientation is much more stable for the three metal oxides, thus lithium generally prefers to adsorb where it will be triply coordinated to two bridging oxygens and one in-plane oxygen atom.

Table 4.3: Adsorption energies for the MO_2 at different orientations.

Configuration	MnO_2 E_{ads} (eV)	TiO_2 E_{Ads} (eV)	VO_2 E_{Ads} (eV)
Bbi	-1.80	-3.12	-5.88
Bii	-1.76	-2.72	-5.60

Table 4.4: Bond lengths for the three different stable modes of adsorption for MnO_2.

Li adsorption site	d (Li-O_i) Å	d (Li-O_b) Å
Bbi	2.00	1.94 , 1.97
bii (nnn)	2.03 x2	1.80
bii (nn)	2.10 x 2	1.79

When the initial symmetry is broken the Li adatoms move away from these sites. We then examined the electron transfer from Li adatoms, in the bbi and bii sites, to the surface cations.

Table 4.5: Bond length for the different modes of adsorption for TiO_2

Li adsorption site	d (Li-O_i) Å	d (Li-O_b) Å
Bbp	1.97	1.99
Bii	1.97	2.07

Table 4.6: Bond length for the different modes of adsorption for VO_2

Li adsorption site	d (Li-O_i) Å	d (Li-O_b) Å
Bbi	1.94	1.93
Bii	1.97	1.79

A Bader analysis shows that in all cases the adsorbed Li adopts a positive charge (~+0.9|e|), which indicates that an electron has been donated to the surface. Clearly, this electron should go to the metal (Mn, Ti and V) cations, because the oxygen anions have a complete electron shell. In order to identify which M cations were reduced, we look at the integration of the spin density over the Mn/ Ti and V Bader volumes, which generally give a better indication of cation reduction than the charge density [165, 166]. For the reduced M cation we find a clear increase in the spin moment of approximately $0.99\mu_B$. For the bbi site, there are three symmetrically distinct possibilities for where the electron localises on the surface cations: one 5-fold M and two 6-fold M cations. Each of these is tested in turn, initially localising the electron on each site and then relaxing the electronic and geometric structure. The initial localisation was forced by using a computational “trick”: we temporarily substitute M by Fe in the site where we want to force localisation. Because Fe is more stable in the 3+ oxidation state than in the 4+, the geometry relaxation leads to a structural distortion favourable to the presence of a 3+ cation in that lattice site. When we put M back in that position, it tends to reduce preferably over those in other lattice positions. Following this procedure, we find that the M (6-fold) cations are not stable for localisation of the extra electron, that is, the transferred electron always goes to the M (5-fold) cation at the surface, regardless of the initial localization. For a bii lithium adatom, again there are three distinct possibilities for the localisation of the

transferred electron. Tables 5.1- 5.3 shows the changes in energy and charge localization when sodium is adsorbed on the surface, these tables only show the interaction of sodium with the surface metal. The localisation on the M (6-fold) cation is again found to be unstable. Electron localisation on the two different M (5-fold) cations (relative to the Li position) leads to different adsorption energies: the electron localises on the M (5-fold) cation that is the next-nearest neighbour (nnn) to the Li adatom. This behaviour, which arises from the higher elastic energy in accommodating the distortions produced by both the adatom and the reduced cation in very close positions, is the opposite of what is expected in terms of pure electrostatics: if the Coulomb effect was dominant, the nearest M cation would be reduced, in order to decrease the M–Li repulsion. The non-Coulombic charge localisation effect has been found in other cases of charge transfer between adatoms and oxide surfaces [166]. Furthermore, the bond length (Li-O_i and Li-O_b) of the relaxed systems where lithium has occupied its favourite position on the metal oxide surface is shown in table 4.2 - 4.4.

4.3 Oxygen adsorption at the Li/MO_2 (110) surface

We now examine the catalytic influence of metal oxide (110) surfaces, i.e. MnO_2, TiO_2 and VO_2, on the formation of discharge products in the Li-air batteries. Some of the prominent products that have been reported widely in literature are depicted in fig 4.2, and they are bulk Li_2O_2 peroxos and monomers both with O-O bond length of 1.55 Å.

We considered the adsorption of oxygen (two O atoms per surface cell, Γ =2) on the Li/MO_2 (110) surface. In order to investigate the stability of Li–O–O–Li species, which are known to be important in the Li–air battery, we also consider two Li atoms

per surface cell, assuming that they both occupy the most stable bbi sites. It should be noted that since there are only two bbi sites at each surface in our simulation cell, this structure corresponds to full coverage of the bbi sites at the surface, that is, a monolayer of Li adatoms. Therefore, based on the results discussed above, all the M (5-fold) surface cations can be expected to be reduced before oxygen adsorption, which has been confirmed using Bader analysis.

We investigate a number of oxygen adsorption configurations, in some cases keeping the molecular bond between the two oxygen atoms, and in others assuming dissociative adsorption. We found four different stable configurations, which are shown in figure 4.2. Some of the configurations initially considered were found to be unstable (in the sense of not being a minimum in the adsorption energy landscape).

For example, although a configuration with one oxygen atom directly on top of each Li is a stationary point, it is in fact unstable and relaxes (if the symmetry of the initial configuration is broken) to a peroxo configuration bridging between two Li atoms, as in figure 5.2 (iii). The oxygen adsorption energy in this Li-peroxo configuration is -1.81 eV/O_2, -2.23 eV/O_2, and -4.03eV/O_2 for MnO_2, TiO_2 and VO_2 respectively as shown in table 4.5 and Figure 4.2 iii). In this configuration, the calculated O-O bond lengths, associated with MnO_2 and TiO_2 catalysts, are around 1.55 Å and are consistent with those of the hexagonal bulk and monomer Li_2O_2 (1.55 Å).

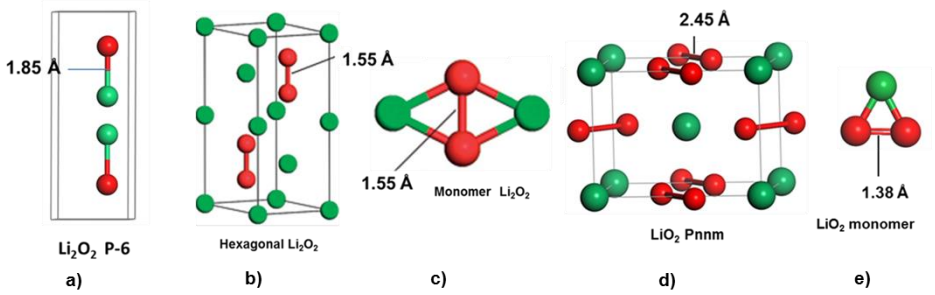

Figure 4.2: Discharge products in Li-air battery; structure of Li_2O_2 (a-c), P-6, hexagonal ($P6_3/mmc$) and a monomer respectively; structure of LiO_2 (d &e) Pnnm and its monomer respectively showing the relaxed O–O distances.

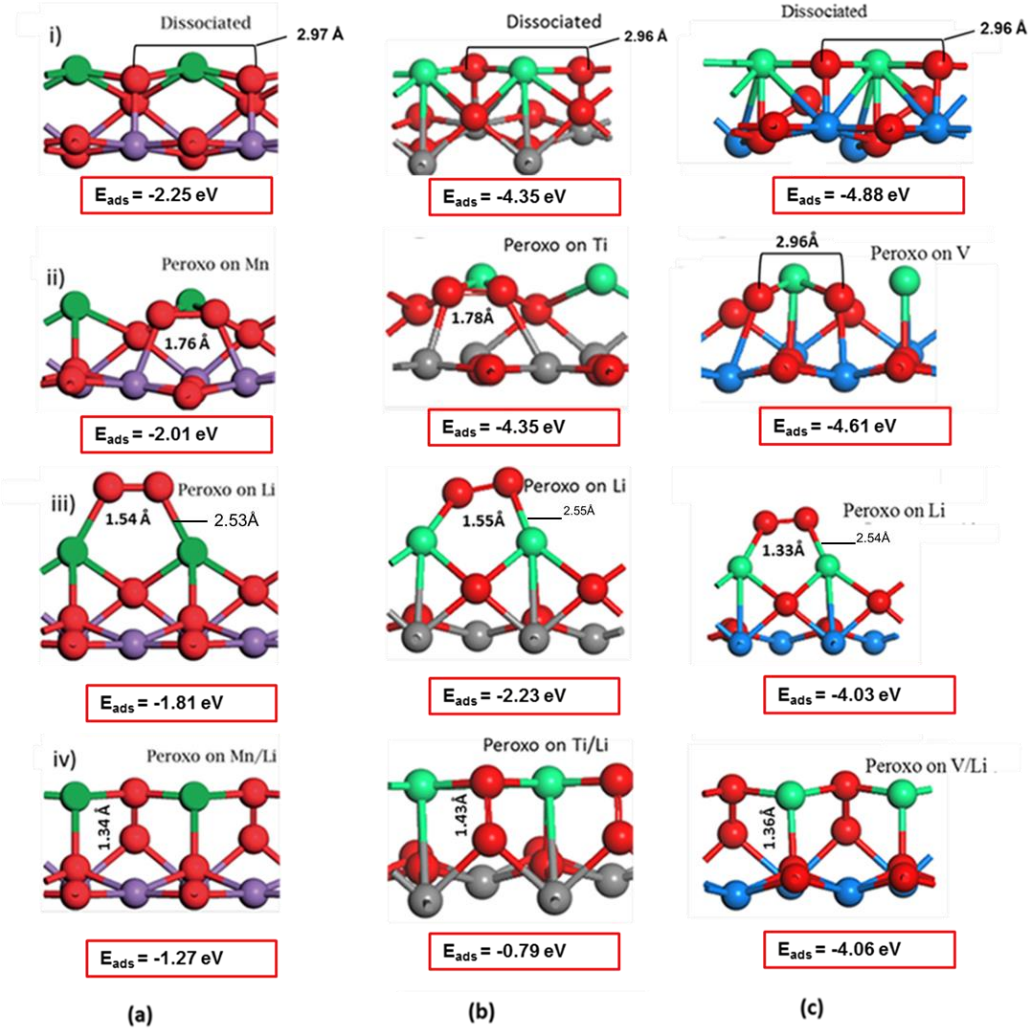

Figure 4.3: Stable adsorption configurations for two oxygen atoms at the (a) Li/MnO_2 (b) Li/TiO_2 and (c) Li/VO_2 (110) surface.

The O-O bond lengths of LiO_2 bulk and monomer forms are 2.45 Å and 1.38 Å respectively. Adsorption of oxygen, as atoms and molecules, on lithiated metal oxide surfaces will obviously yield discharge products of varying stability which will be attested to by corresponding adsorption energies. On the other hand VO_2 catalyst induces a compressed O-O bond length of 1.33 Å which is closer to 1.38 Å of the LiO_2 monomer.

The Li-peroxo is not the only stable peroxo adsorption configuration: a peroxo group bridging directly between the two previously unsaturated Mn and Ti cations, as in figure 4.2. ii) (E_{ads}= -2.01 eV/O_2, -4.35eV/O_2 for MnO_2 and TiO_2 respectively) is noted. It is further observed that the O-O separations are 1.76 and 1.78 Å for MnO_2 and TiO_2 respectively, which are relatively larger than those of the Li_2O_2 monomer and bulk hexagonal forms (1.55 Å). However, when oxygens are located directly above the V cations a peroxo bridging group is not formed, on the contrary, a dissociated configuration is stable with the adsorption energy of -4.61eV/O_2 for VO_2 and this is further confirmed by an extended the O-O bond length to 2.96 Å. Another stable peroxo configuration, which on the other hand is the least stable in figure 4.2, involves a peroxo perpendicular to the surface and binding to Li on one end and to M on the other end, as in figure 4.2.(iv) (E_{ads}= -1.27 eV/O_2, -0.79eV/O_2, --4.06eV/O_2 for MnO_2, TiO_2 and VO_2 respectively). Generally, the O-O bond lengths of the products, shown in figure 4.2 iv), are reduced relative to those of the bulk and monomer of Li_2O_2. Furthermore, the O-O bond length on the MnO_2 (1.34 Å) and VO_2 (1.36 Å) are closer to those of the LiO_2 monomer which has O-O bond length of 1.38 Å. However, the O-O bond length on the TiO_2 surface (1.43 Å), does not compare with that of any known discharge products, but lies between that of monomers for Li_2O_2 and LiO_2 .

The most stable configuration found was the dissociative adsorption where there is an oxygen atom on the “bulk-like” positions on top of each of the M cations, but with additional bonds formed with the Li adatoms, as in figure 4.2. i) (E_{ads} = -2.25 eV/O_2, -4.35eV/O_2 and -4.88eV/O_2). The dissociative configuration is further confirmed by large O-O bond lengths of approximately 2.96 Å in magnitude, for all metal oxides under study. The trend of stability is almost similar in all metal oxides, the dissociative adsorption configuration being the most stable, regardless of the type of metal oxide.

Table 4.7: Adsorption energies for oxidation of the lithiated MO_2 (MnO_2, TiO_2 and VO_2).

Configuration	MnO_2 Ads Energy (eV)	TiO_2 Ads Energy (eV)	VO_2 Ads Energy (eV)
Dissociative	-2.25	-4.35	-4.88
Peroxo on M	-2.01	-4.35	-4.61
Peroxo on Li	-1.81	-2.23	-4.03
Peroxo on M/Li	-1.27	-0.79	-4.06

These results show that, due to the presence of cation sites amenable to oxidation, oxygen adsorption on the Li/MnO_2 (110) surface is much more favourable than on the pure MnO_2 (110) surface. In figure 4.4 we show that the range of chemical potentials at which oxygen adsorption (at a coverage of two O atoms per cell) is stable with respect to the non-oxidised surface, extends beyond -1 eV, which is ~0.5 eV below the threshold in the Li-free surface, meaning that the Li/MnO_2 (110) surface will remain oxidised up to temperatures of ~1000 K at ambient oxygen

pressure. Figure 4.5 also shows that oxygen adsorption on the Li/TiO_2 (110) surface is also more favourable than on the pure TiO_2 (110) surface. It can be concluded that the range of chemical potentials at which oxygen adsorption is stable relative to the non-oxidised surface has been extended and the surface will remain oxidised up to 1400K for the peroxo on Li and beyond this temperature for the peroxo on Ti and dissociated configuration.

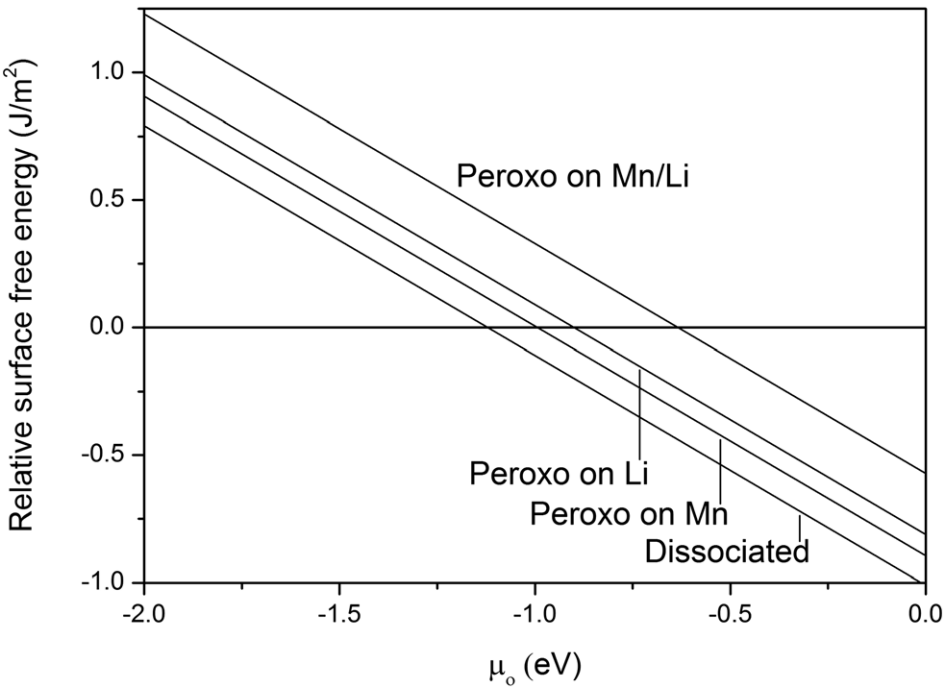

Figure 4.4: Surface free energies of the oxidised Li/MnO_2 (110) surfaces with respect to the non-oxidised termination.

Oxidation on Li/VO_2 is not stable relative to the Li free surface as shown in figure 4.5 that is reduced to -0.12 eV which is 0.80 eV above the threshold of the Li free surfaces. According to the order of the plots it is observed that the most stable configuration is the dissociated which is the same for other metal oxide catalysts (MnO_2 and TiO_2).

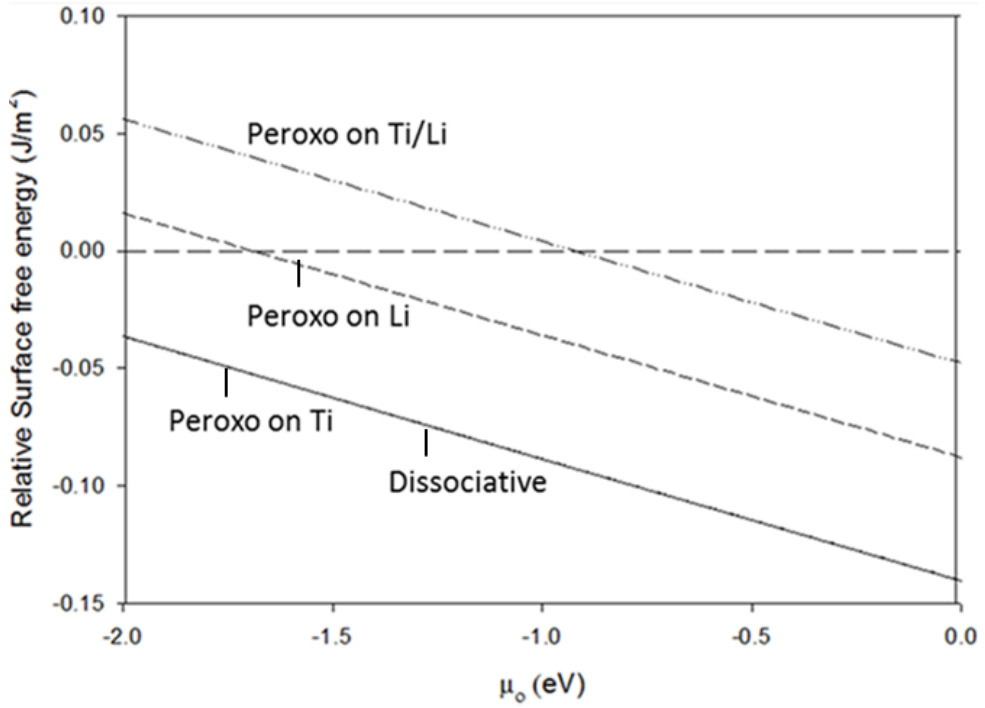

Figure 4. 5: Surface free energies of the oxidised Li/TiO_2 (110) surfaces with respect to the non-oxidised termination.

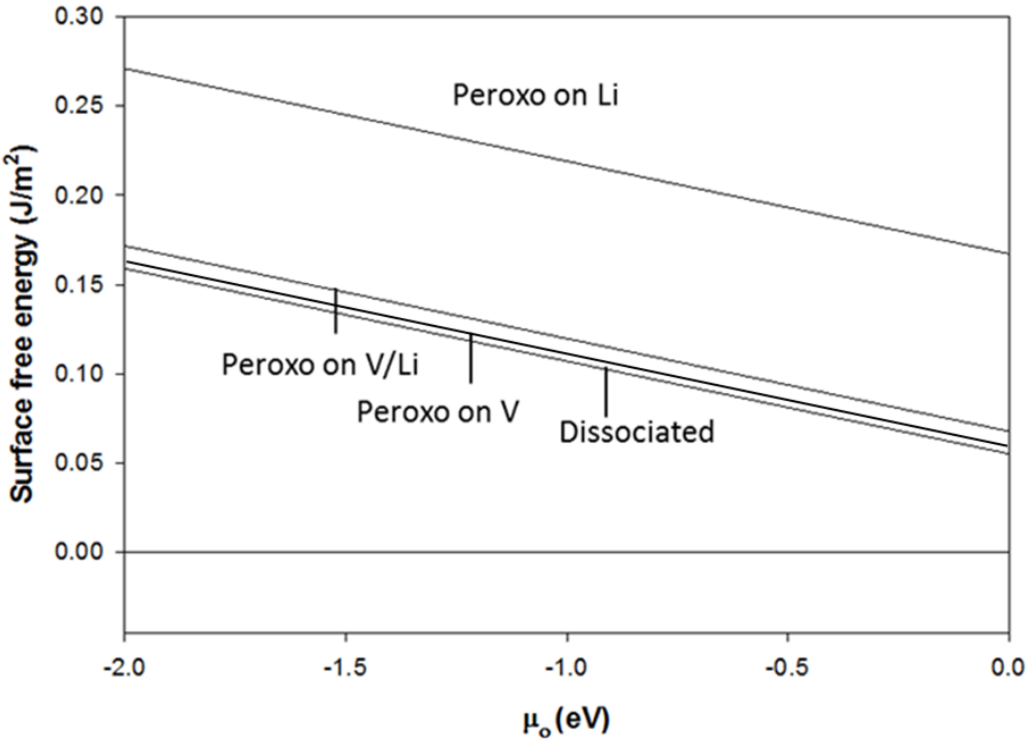

Figure 4.6: Surface free energies of the oxidised Li/VO_2 (110) surfaces with respect to the non-oxidised termination.

On the whole, it is observed that the dissociated configuration is the most stable relative to all configurations, for the three metal oxides, which is then followed by the peroxo on Mn configuration which is consistent with the calculated adsorption energies. The next less stable configuration is the peroxo on Li and the least is peroxo on M/Li relative to other configurations, where the last two are near equivalent for VO_2.

4.4 Effect of MO_2 in the cathode reaction in a Li–air battery

During the battery discharge process, molecular oxygen is reduced in the cathode, in the presence of Li cations and electrons, forming lithium peroxide (Li_2O_2) particles:

$$O_2 + 2Li^+ + 2e^- \rightarrow Li_2O_2. \quad 4.1$$

The essential prerequisite for the successful operation of a rechargeable Li air battery is the formation of Li_2O_2 as a reaction product during discharge and the decomposition of Li_2O_2 to Li and O_2 during charging. However, one of the critical problems in the non-aqueous Li air batteries employing carbon based oxygen electrode is the very large polarization that occurs during the discharge/charge process. The high cell polarization is mainly attributed to the low catalytic activity of carbon and to the high activation energies required for the formation of Li_2O_2 during discharge and the decomposition of the Li_2O_2 during charging. It has been confirmed that the discharge/charge efficiencies can be improved by the addition of catalytic materials to the carbon supported oxygen electrodes. The catalysts included in the oxygen electrode such as MO_2 can affect the discharge/charge potentials and determine the rechargeability of the cells [167]. Hence, the energetics associated with MnO_2, TiO_2 and VO_2 as catalysts and how they impact on the formation of Li_2O_2 as discharge products will be discussed.

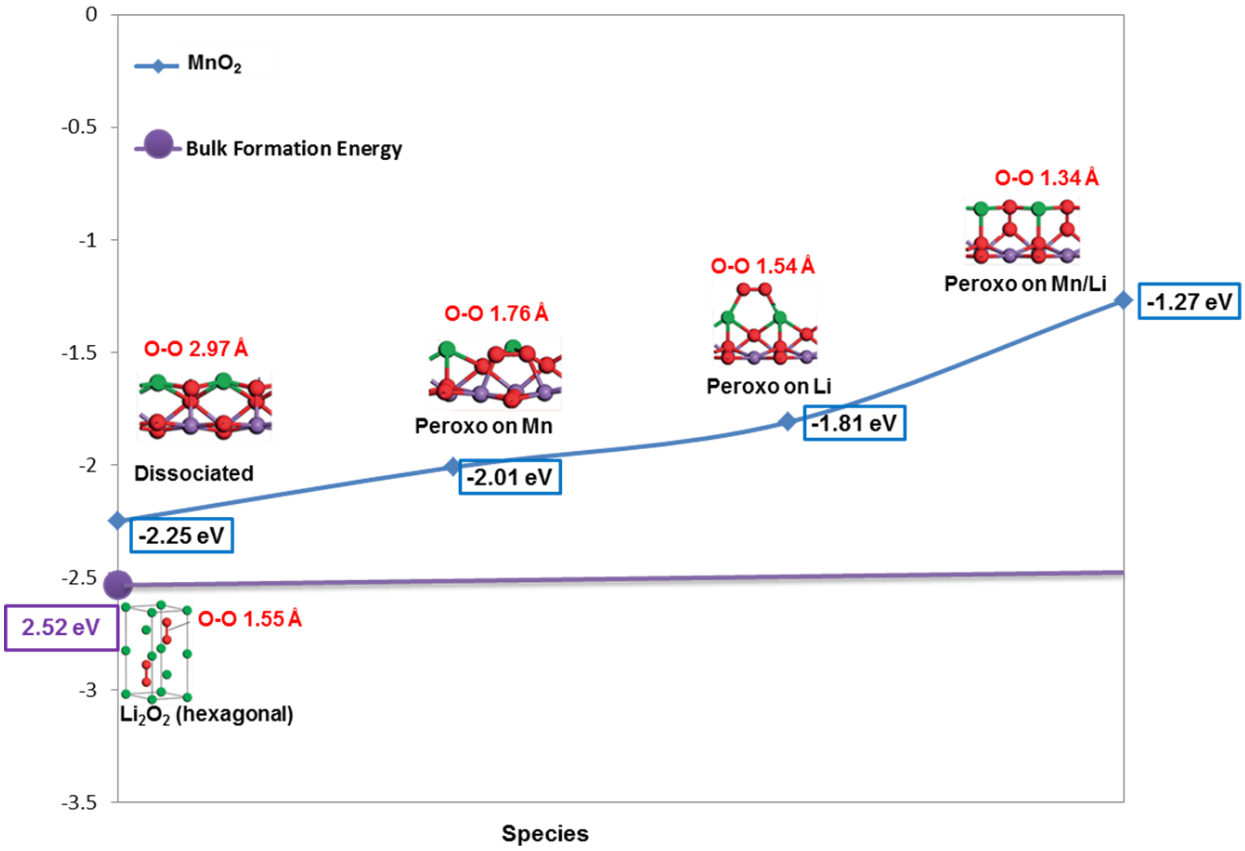

Figure 4.7: MnO_2 surface (110) adsorption and lithium peroxide bulk energetics.

Firstly, a comparison of the formation energy of the hexagonal bulk Li_2O_2, which is -2.52eV/Li [168], shown in figure 4.2 (b) and figure 4.7 with the energy of formation of the surface lithium oxide at MnO_2 (110) is insightful. The energy of formation for the bulk is lower by 1.25eV/Li relative to the least stable configuration for oxygen adsorption on lithiated surfaces figure 4.3 (a) iv) (peroxo on Mn/Li) and figure 4.7. Further comparisons of the bulk energy of formation to the most stable configuration of the surface lithium oxide figure 4.3 (a) i) (dissociated configuration) and figure 4.7 shows that the former is lower by 0.27ev/Li. This agrees with the experimental observation that Li_2O_2 is the main product of the cathode reaction in Li–air batteries (both in the presence and in the absence of MnO_2) [169]. The initial reduction of

oxygen in the cathode occurs more favorably via the dissociative adsorption of the oxygen molecule at the lithiated MnO_2 surface, forming the structures described in figure 4.2 (a), than via the formation of small unsupported Li_2O_2 clusters. Hence when the Li_2O_2 particles grow in contact with such MnO_2 surfaces, then the barrier for the formation of the lithium peroxide particles at the cathodes would be reduced.

We further consider the impact of TiO_2 as a catalyst on the growth of the Li_2O_2 product. The energy of formation for the bulk is lower by 0.29eV/Li for peroxo on Li (figure 4.3 (b) iii) and 1.73eV/Li for the peroxo on Ti/Li (figure 4.3 (b) iv), as also shown in figure 4.8.

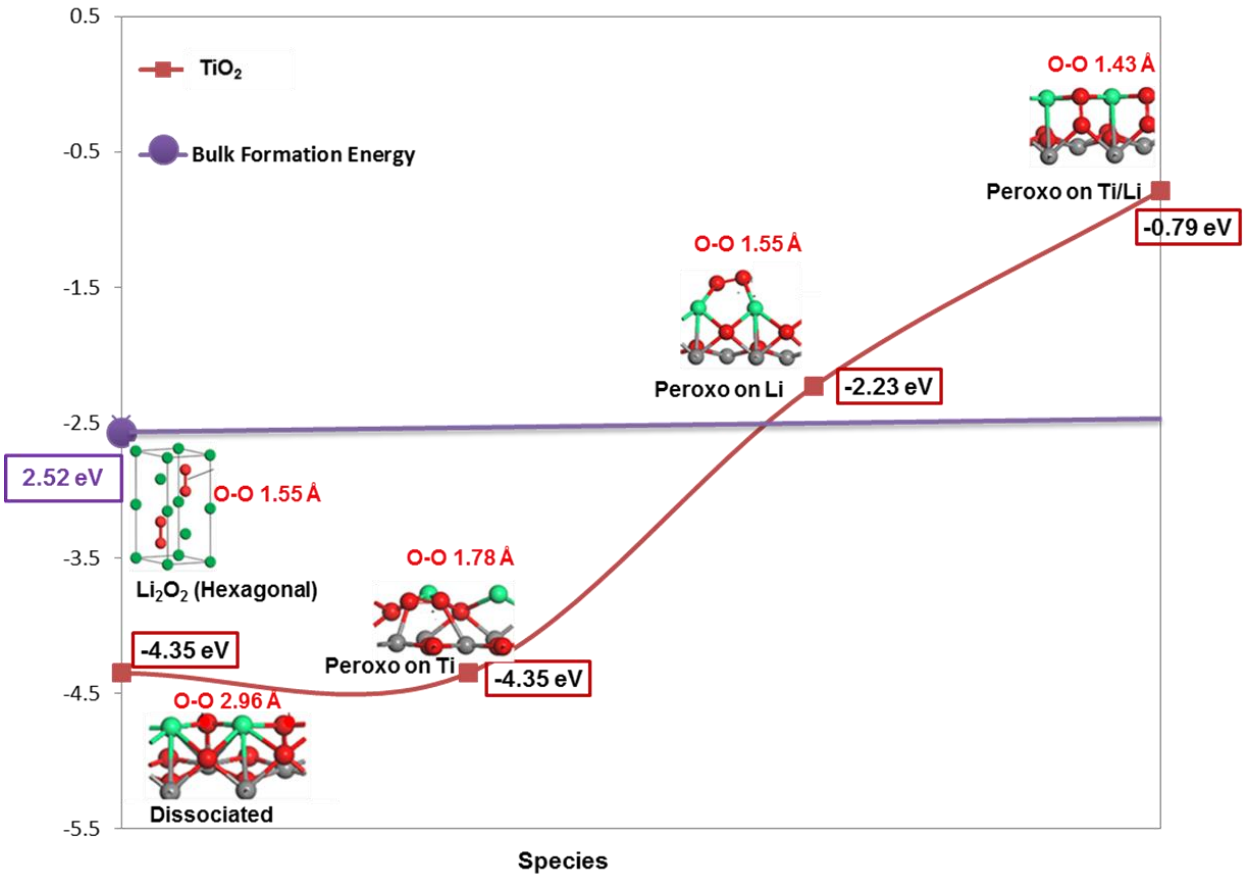

Figure 4.8: TiO_2 surface (110) adsorption and lithium peroxide bulk energetics.

This agrees with the experimental observation that Li_2O_2 is the main product of the cathode reaction in Li–air batteries (both in the presence and in the absence of TiO_2). When comparing the energy of formation to the most stable configuration of the surface lithium oxide in figure 4.3 (b) i) and ii) and figure 4.8 (dissociated and peroxo on Ti configuration), the formation energy of the bulk is higher by 1.83ev/Li. This implies that, for such configurations, the formation of Li_2O_2 will not be expedited since clusters are too stable and would stick to the TiO_2 surface. It can therefore be surmised that the initial reduction of oxygen in the cathode occurs more favorably via the peroxo on Li and peroxo on Ti/Li at the lithiated TiO_2 surface, forming the structures described in figure 4.3 (b) and figure 4.8, than via the formation of small unsupported Li_2O_2 clusters.

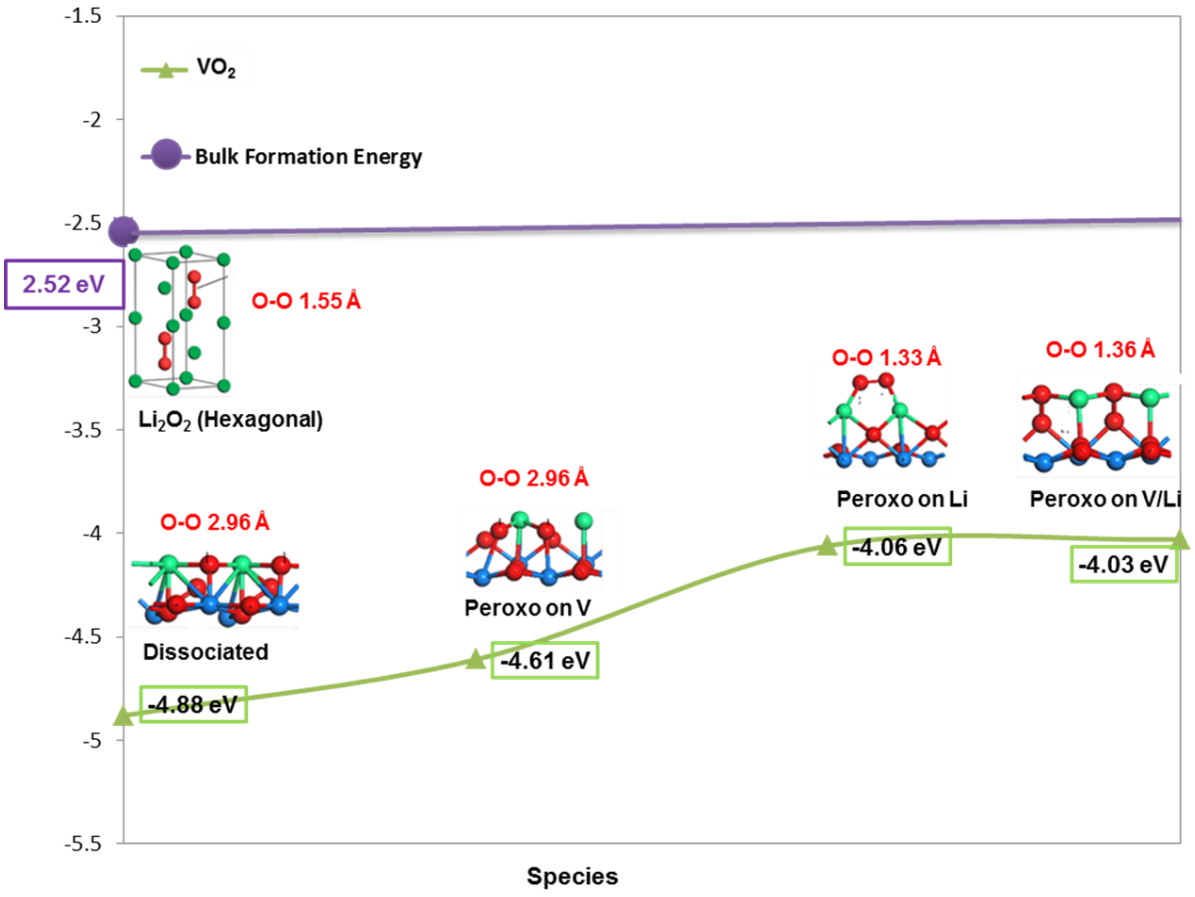

Figure 4.9: VO_2 surface (110) adsorption and lithium peroxide bulk energetics.

Lastly, on comparing the energy of formation of the bulk Li_2O_2, which is -2.52eV/Li and shown in figure 4.2 (b) and figure 4.9, and the energy of formation of the surface lithium oxide at VO_2 (110) figure 4.9 (dissociative, peroxo on V, peroxo on Li and peroxo on V/Li)], the energy of formation for the bulk is higher by approximately 2.4eV/Li in all stable configurations for oxygen adsorption on lithiated surfaces. This is almost twice the value of the formation energy of the bulk Li_2O_2 implying that in all such configurations, formation of Li_2O_2 will not be encouraged since the clusters are too stable and would stick to the VO_2 surface.

Although several studies have alluded to the effectiveness of transition metal oxide catalysts on the performance of Li-air batteries, the related energetics have not been adequately quantified. It has mainly been mentioned how the catalysts improve the formation and decomposition of Li_2O_2 during discharging and charging. The energetics calculated for configurations related to the three chosen rutile type metal oxides, i.e. MnO_2, TiO_2 and VO_2 as possible catalysts in the discharge process of Li-O_2 batteries have clearly depicted, that the MnO_2 could expedite nucleation and growth of the Li_2O_2 discharge product, across all configurations. It has further been shown that TiO_2 promotes nucleation for limited configurations, in particular peroxo on Li with O-O bondlength of 1.55 Å and peroxo on Ti/Li with the O-O bondlength of 1.43 Å, whereas the VO_2 does not appear to play any significant role in this process, for all configurations considered.

Indeed, in previous studies, manganese dioxides have been widely investigated as catalysts, among transition metal oxides, for the ORR/OER in non-aqueous lithium-oxygen batteries, due to the low cost, environmental friendliness, and easy preparation [74-76]. In particular, it was shown that nanostructured MnO_2 in different polymorphic states are able to catalyse the formation and decomposition of Li_2O_2 in

the cathode, thus decreasing the overpotentials required for the operation of the Li–air cell [170]. In that case, it was the surface rather than the bulk of the manganese oxide which controlled its function in the cathode, and therefore the lack of Li intercalation in bulk β- MnO_2 was not expected to limit its utilization. The current study has provided an explanation, based on the energetics, as to why the manganese dioxides are preferred, compared to other isostructural metal oxides. It has further enhanced, at a nanoscale, an understanding of processes on the surface of cathode catalysts that are key for improving the function of Li–air batteries [170].

The effectiveness of the MnO_2 as a catalyst in Li-O_2 batteries can further be enhanced by incorporating it into a bifunctional catalyst. Chen *et al*. reported a nanoporous gold supported MnO_2 electrode for non-aqueous lithium-oxygen batteries [171], and the results showed that the highly conductive gold substrate significantly enhanced the catalytic activities of MnO_2 for both OER and ORR. Other types of bifunctional catalysts which provide enhanced production of Li_2O_2 involve RuO_2/$NiCo_2O_4$ nanosheet composite [172]. The current study has, from energetics, provided mechanisms for identifying catalysts that are likely to be effective in operation of Li-O_2 batteries. Hence such an approach can also be extended to bi-functional catalysts, where the effectiveness of TiO_2 could further be explored and enhanced, even for configurations that appeared dormant or probe the usefulness of VO_2 and other established and potential metal oxide catalysts [173].

Chapter 5: Sodium and oxygen adsorption and co-adsorption on MO_2 surfaces

5.1 Introduction

In this chapter we discuss Na adsorption on the three metal oxides MO_2 (MnO_2, TiO_2 and VO_2) surfaces. It is important to understand charge transfer reactions that produce the potential difference in the battery from the Na adatom to the surface M (Mn, Ti and V) in order to have sodium-air batteries that are productive. Oxidation on the sodium adsorbed surfaces will be discussed as well where different and stable orientations will be studied, in order to observe the most stable orientation. We calculated the surface free energies of the most stable composition for the oxidation on the Na adsorbed surfaces of the metal oxides (MnO_2, TiO_2 and VO_2).

5.2 Charge transfer from sodium adatom to the surface metal (M) cation

Understanding the surface behaviour of Na-doped MO_2 is important in the context of MO_2-based Na–air batteries. We now consider the mode of the transfer of an electron from a Na adatom to a surface M cation using Bader analysis. The first step is to determine onto which surface site Na preferentially adsorbs. Different possible adsorption sites on the surface were systematically tested and the results are reported in Table 5.1. We find that Na adatoms are more stable in sites of lower oxygen coordination. The site with lowest adsorption energy (-2.08 eV) is where Na is singly coordinated, bonded to bridging oxygen atom (bb) for MnO_2 and (-3.36 eV) for VO_2 at high oxygen coordination. For TiO_2, the most stable Na orientation is where Na has high oxygen coordination, both bii and bbi equally (-2.03eV). Although the bb position can provide the most stable configuration, within a specific site, this

depends strongly on where the electron given up by sodium is initially and finally localised.

The presented orientations are stable ones and the unstable (relative to the adsorption energy landscape) are not shown in figure 5.1. In the case of sodium adsorption on VO_2, the Na atom moves closer to the surface cation, thus the adsorption energies for VO_2 are much more negative than in TiO_2 and MnO_2. The bb orientation is much more stable for MnO_2 and VO_2, thus sodium generally prefers to adsorb where it will be singly coordinated to two bridging oxygens whereas for TiO_2, Na prefers the high oxygen coordination for adsorption.

When the initial symmetry is broken the Na adatoms move away from these sites. Therefore the electron transfer from Na adatoms, in the bbi and bii sites, to the surface cations was examined. A Bader analysis shows that in all cases the adsorbed sodium picks a positive charge (~+0.9|e|), which shows that an electron has been donated to the surface. It is expected that the electron would go to the metal (Mn,Ti and V) cations, because the oxygen anions have a complete electron shell. Identifying which M cations were reduced, we look at the integration of the spin density over the metal Bader volumes, which give an indication of cation reduction than the charge density [165,166]. For the reduced M cation, an increase in the spin moment of approximately $0.89\mu_B$ is noticed.

The initial localisation was imposed by using a computational “trick” i.e. we substituted M by Fe in the site where localisation is required to take place. The fact that Fe is more stable in the 3+ oxidation state compared to that of 4+, the geometry relaxation results in structural deformation that favours the presence of a 3+ cation in that lattice site.

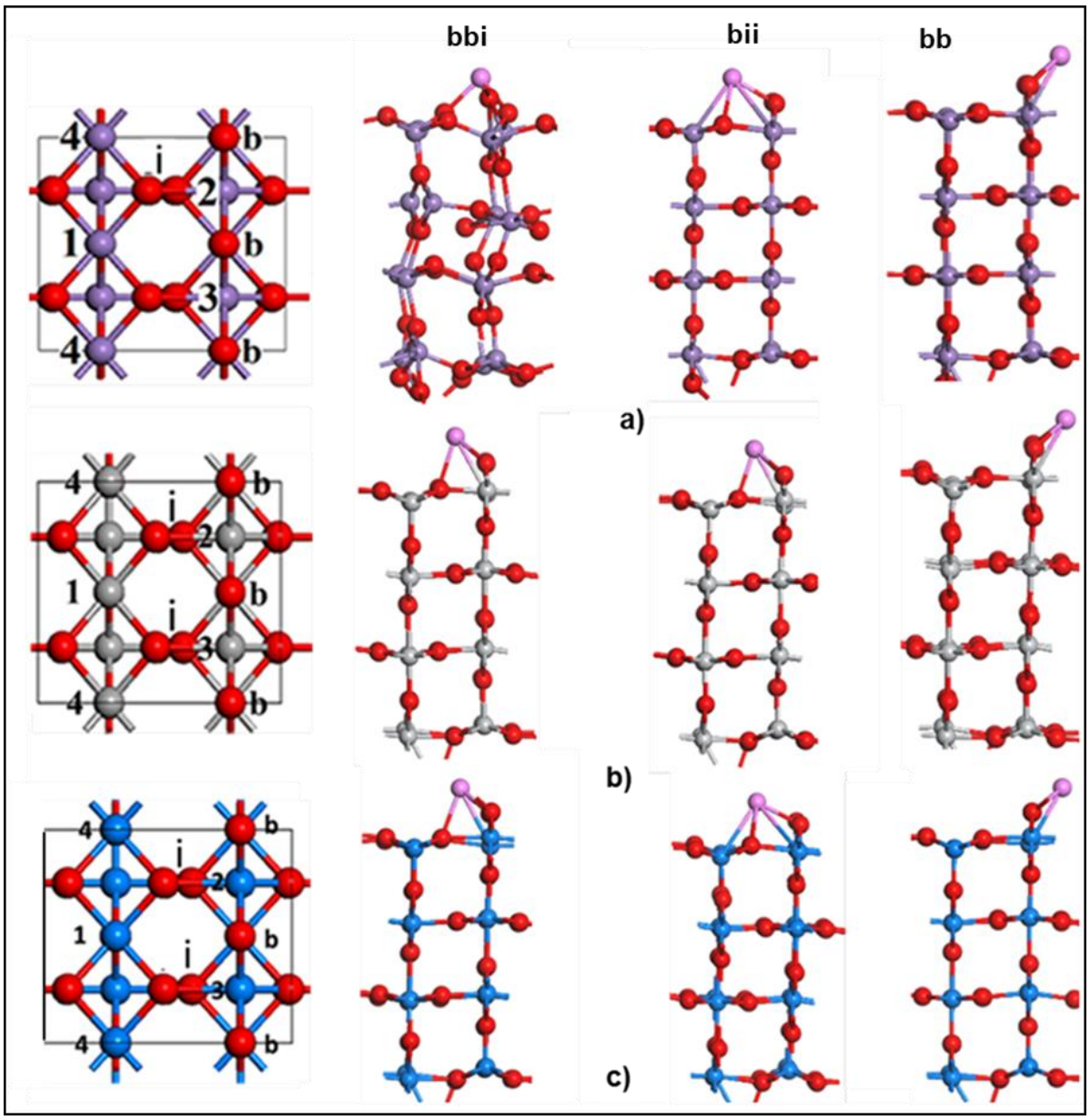

Figure 5.1: (Left to right) 'Bird's eye' view of stoichiometric (110) MO_2 surface with in-plane (i) and bridging (b) oxygens lettered and electron localisation sites numbered; sodium adsorption on relaxed (a) MnO_2, (b) TiO_2 and (c) VO_2 (110) surface.

Table 5. 1: Bader analysis for MO_2 surface with Li in the bbi position; O atoms are not considered.

Species	bbi (eV)	bbi μ ($_B$)	bbi (eV)	bbi (μ_B)
	Initial		Final	
Fe-M	5.348	3.466	5.137	-2.663
M	5.259	2.645	5.208	3.218
M	5.283	2.537	5.308	3.219
Na	0.134	-0.002	0.134	-0.002

Table 5. 2: Bader analysis for MO_2 surface with Li in the bii position; O atoms are not considered.

Species	bii (eV)	bii (μ_B)	bii (eV)	bii (μ_B)
	Initial		Final	
Fe-M	5.383	3.527	5.337	3.519
M	5.233	2.538	5.284	2.617
M	5.233	2.532	5.230	2.548
Na	0.139	-0.0005	0.142	-0.0005

Table 5. 3: Bader analysis for MO_2 surface with Li in the bb position; O atoms are not considered.

Species	bb (eV)	bb (μ_B)	bb (eV)	bb (μ_B)
	Initial		Final	
Fe-M	5.365	-2.645	5.362	3.498
M	5.206	3.521	5.207	2.629
M	5.206	3.521	5.207	2.629
Na	0.100	-0.001	0.100	-0.0007

Table 5.4: Adsorption energies for the MO_2 at different orientations.

Configuration	MnO_2 E_{ads} (eV)	TiO_2 E_{Ads} (eV)	VO_2 E_{Ads} (eV)
Bbi	-1.53	-2.03	-3.36
Bii	-1.94	-2.03	-3.28
Bb	-2.08	-1.99	-3.41

Table 5.5 Bond lengths for the three different stable modes of adsorption for MnO_2

Na adsorption site	d (Na-O_i) Å	d (Na-O_b) Å
Bbi	2.37	2.33
bii	2.12	2.37
Bb	-	2.25

Table 5.6: Bond length for the different modes of adsorption for TiO_2

Na adsorption site	d (Na-O_i) Å	d (Na-O_b) Å
Bbp	2.31	2.24
Bii	2.31	2.23
Bb	-	2.22

Table 5.7: Bond length for the different modes of adsorption for VO_2

Na adsorption site	d (Na-O_i) Å	d (Na-O_b) Å
Bbi	2.32	2.22
Bii	2.32	2.22
Bb	-	2.22

Again replacing Fe to original M, it tends to reduce preferably over those in other lattice positions. It is observed that when following the procedure of replacing M - Fe and Fe- M, the M (6-fold) cations are unstable for localisation of the extra electron, that is, the transferred electron always goes to the M (5-fold) cation at the surface, regardless of the initial localization. For a bii sodium adatom, there are three distinct possibilities for the localisation of the transferred electron. The localisation on the M (6-fold) cation is found to be unstable. Electron localisation on the two different M (5-fold) cations (relative to the Na position) leads to different adsorption energies: the electron localises on the M (5-fold) cation that is the next-nearest neighbour (nnn) to the Na adatom. This behaviour, which arises from the higher elastic energy in accommodating the distortions produced by both the adatom and the reduced cation in very close positions, is the opposite of what is expected in terms of pure electrostatics: if the Coulomb effect was dominant, the nearest M cation would be reduced, in order to decrease the M–Na repulsion. The non-Coulombic charge localisation effect has been found in other cases of charge transfer between adatoms and oxide surfaces [167]. Tables 5.1- 5.3 shows the changes in energy and charge localization when sodium is adsorbed on the surface, these tables only show the interaction of sodium with the surface metal. Furthermore, the bond length

($Na\text{-}O_i$ and $Na\text{-}O_b$) of the relaxed systems where sodium has occupied its favourite position on the metal oxide surface is shown in table 5.2 - 5.4.

5.3 Oxygen adsorption at the Na/MO_2 (110) surface

We consider the adsorption of oxygen (two O atoms per surface cell, Γ =2) on the Na/MO_2 (110) surface. In order to study the stability of Na–O–O species, which are known to be important in the Na–air battery, we also consider two sodium atoms per surface cell, assuming that they both occupy the stable bbi sites. It should be noted that since there are only two bbi sites at each surface in our simulation cell, this structure corresponds to full coverage of the bbi sites at the surface, that is, a monolayer of Na adatoms. Therefore, based on the results discussed above, all the M (5-fold) surface cations can be expected to be reduced before oxygen adsorption, which has been confirmed using Bader analysis.

We now examine the impact of the various metal oxide (MnO_2, TiO_2 and VO_2) catalysts on the formation of discharge products, namely NaO_2 and Na_2O_2, during the cycling of Na air batteries. Figure 5.2 shows structures of possible discharge products and their related O-O separations, i.e. bulk NaO_2 in pyrite (1.34 Å), marcasite (1.28 Å), Fm-3m polymorphs and the corresponding NaO_2 monomer (1.43 Å). Furthermore, the O-O bond lengths of the bulk (1.49 Å), P-62m and monomer (1.56 Å) Na_2O_2 are depicted.

A number of oxygen adsorption configurations have been explored, in some cases keeping the molecular bond between the two oxygen atoms, and in others assuming dissociative adsorption. Four different stable configurations have been found, which are indicated in figure 5.3.

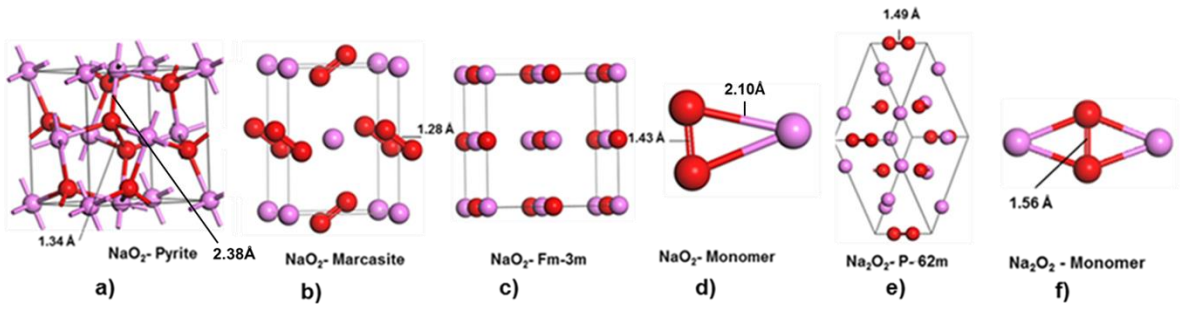

Figure 5.2: Discharge products in Na-air battery; structure of NaO_2 (a-d), pyrite, marcasite, Fm-3m and a monomer respectively; structure of Na_2O_2 (e &f) P-62m and its monomer respectively showing the relaxed O–O distances.

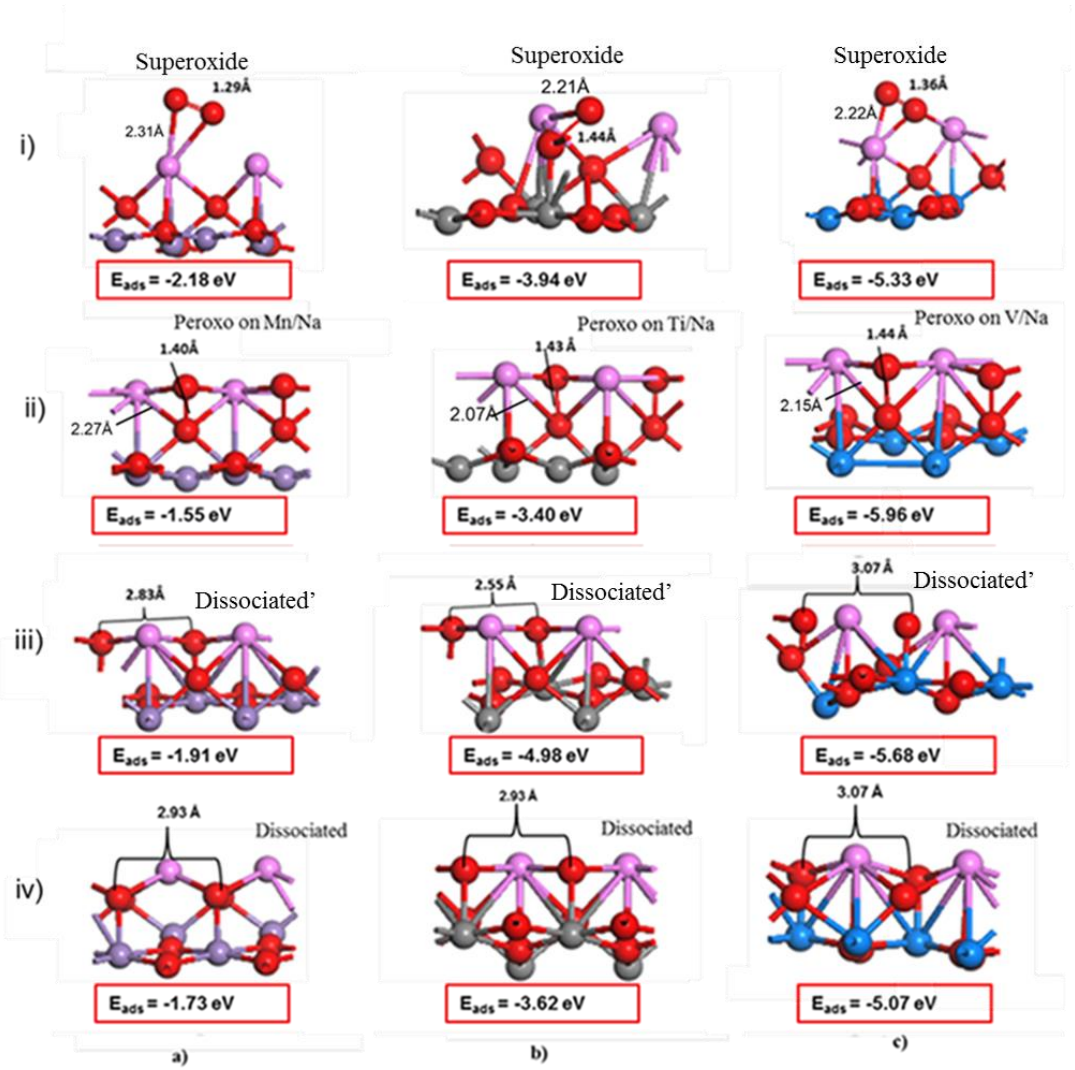

Figure 5.3: Stable adsorption configurations for two oxygen atoms at the (a) Li/MnO_2 (b) Na/TiO_2 and (c) Li/VO_2 (110) surface.

Figure 5.3 shows various configurations that can be adopted by Na-O_2 peroxos when oxygen is adsorbed on different sodiated metal oxide surfaces, i.e. the 110 surfaces of MnO_2, TiO_2 and VO_2.

The first considered configuration is where one oxygen atom is directly located on top of each Na as a stationary point, which is in fact unstable, since this arrangement subsequently relaxes (if the symmetry of the initial configuration is broken) to a peroxo where two oxygens are bonded to one Na atom, as in figure 5.3 (i). The oxygen adsorption energy in the superoxide, configuration is -2.19 eV/O_2, -3.94eV/O_2, and -5.33eV/O_2 for MnO_2, TiO_2 and VO_2 respectively as shown in table 5.5. The resulting O-O bond length of 1.29 Å associated with MnO_2 catalyst, is consistent with those of the bulk marcasite phase of NaO_2. Furthermore, this configuration is the most stable for all MnO_2 based catalysts. The NaO_2 O-O bond length of 1.44 Å induced by the TiO_2 catalyst is consistent with that of the NaO_2 (1.43 Å) monomer and is the second most stable configuration for TiO_2. However, the O-O bond length of NaO_2 where the VO_2 is the supporting catalyst compares well with the O-O bond length in the pyrite form of NaO_2 which is 1.34 Å and it is the one but least stable configuration.

The superoxide configuration is not the only one with stable adsorption configuration: a peroxo group perpendicular to the surface and binding to Na on one end and to M on the other end, as in figure 5.2(iv) (E_{ads}= -1.55 eV/O_2, -3.40eV/O_2, -5.96eV/O_2 for MnO_2, TiO_2 and VO_2 respectively), are stable for MnO_2, TiO_2 and VO_2. In the case of MnO_2 and TiO_2 catalysts such configuration is least stable, whereas for VO_2 it is the most stable arrangement. The molecular form of oxygen is maintained with the O-O bond length ranging from 1.40 Å to 1.44 Å, which is comparable to the O-O bond

length of 1.43 Å for the NaO_2 monomer. Such bond length is also closer to that of the bulk Na_2O_2, namely 1.49 Å.

Another configuration appears when locating oxygens above two previously unsaturated M cations (dissociated'), as in figure 5.3. iii). Upon relaxation the oxygens remain separated with bond lengths ranging from 2.55 to 3.07 Å, mainly suggesting a dissociated configuration, which is however, stable as shown by the adsorption energies (E_{ads}= -1.91 eV/O_2, -4.98eV/O_2, -5.68eV/O_2 for MnO_2, TiO_2 and VO_2 respectively). The cconfigurations in figure 5.3 iii) are the second most stable for MnO_2 and VO_2 but for TiO_2, it is the most stable. An additional stable dissociative configuration is noted in figure 5.3 iv) where there is an oxygen atom on the "bulk-like" positions on top of each of the M cations, but with additional bonds formed with the Na adatoms, as in figure 5.3. iv) (E_{ads} = -1.73 eV/O_2, -3.62eV/O_2 and -5.96eV/O_2). On the whole, this is the second least stable configuration in figure 5.2. The dissociation is further confirmed by large O-O separations ranging from 2.93 to 3.09 Å, across all metal oxides.

There is no trend in terms of the most stable surface, for MnO_2, the most stable configuration is the superoxide group on sodium which clearly shows or encourage the formation of NaO_2. The most stable configuration for the adsorption of oxygen on the Na-TiO_2 is the configuration with the dissociated' whilst the most stable configuration for the adsorption of oxygen on Na-VO_2 is the configuration with peroxo on the surface V and adsorbed Na. The adsorption energy for oxygen adsorption on Na-MO_2 is negative which suggests an exothermic reaction; implying that the reaction does not require external energy to occur and is spontaneous.

Table 5.8: Adsorption energies for oxidation of the Na-MO_2 (MnO_2, TiO_2 and VO_2)

Configuration	MnO_2 Ads Energy (eV)	TiO_2 Ads Energy (eV)	VO_2 Ads Energy (eV)
Dissociated	-1.73	-3.62	-5.07
Dissociated’	-1.91	-4.98	-5.68
Superoxide	-2.187	-3.94	-5.33
Peroxo on M/Na	-1.55	-3.40	-5.96

These results show that, due to the presence of cation sites amenable to oxidation, oxygen adsorption on the Na/MO_2 (110) surface is much more favourable than on the pure MnO_2 (110) surface. Figure 5.4 depicts that the range of chemical potentials at which oxygen adsorption (at a coverage of two O atoms per cell) is stable with respect to the non-oxidised surface, meaning that the Na/MnO_2 (110) surface will remain oxidised up to temperatures of ~1000 K at ambient oxygen pressure. It is observed that the peroxo on Na composition is relatively the most stable composition for the MnO_2 followed by another peroxo group which have a tendency of having a dissociated configuration. The dissociated, and peroxo on Mn/Na are the least stable configuration relative to other configurations but still stable compared to pure MnO_2 surface.

Figure 5.5 shows stability of Na-TiO_2 relative to a pure TiO_2 surface which extends to -0.2 eV which is 0.2 eV below the threshold in the surface without Na. The most stable configuration is the dissociated’ followed by the superoxide.

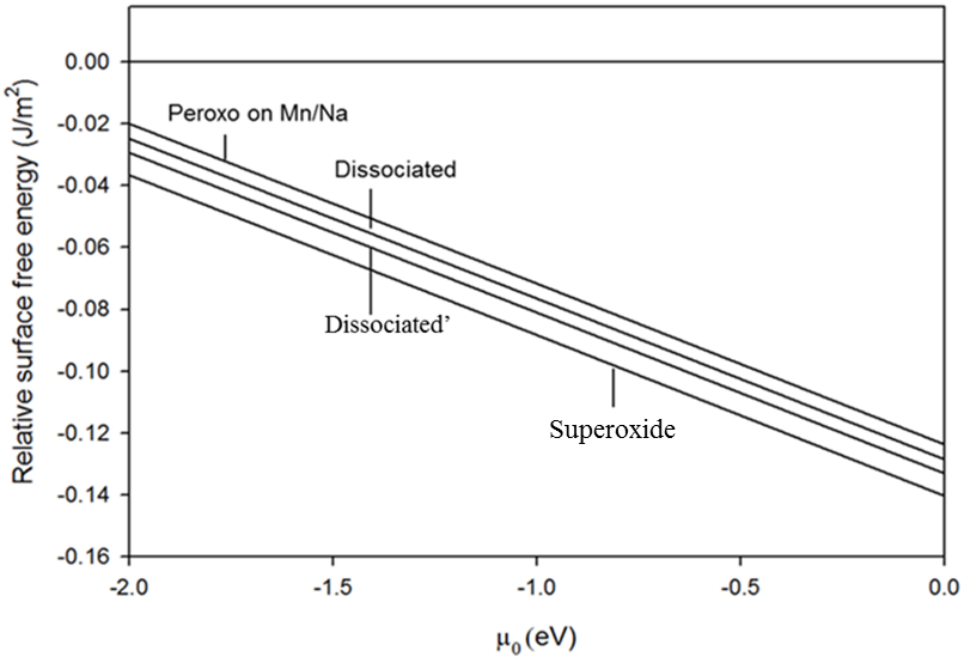

Figure 5.4: Surface free energies of the oxidised Na/MnO_2 (110) surfaces with respect to the non-oxidised termination.

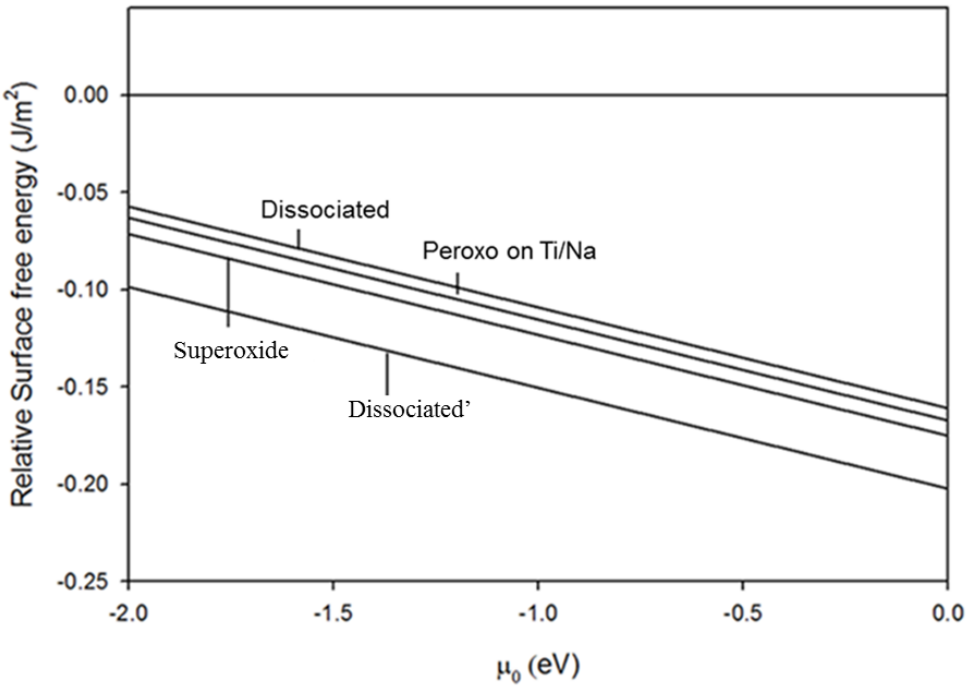

Figure 5.5: Surface free energies of the oxidised Na/TiO_2 (110) surfaces with respect to the non-oxidised termination.

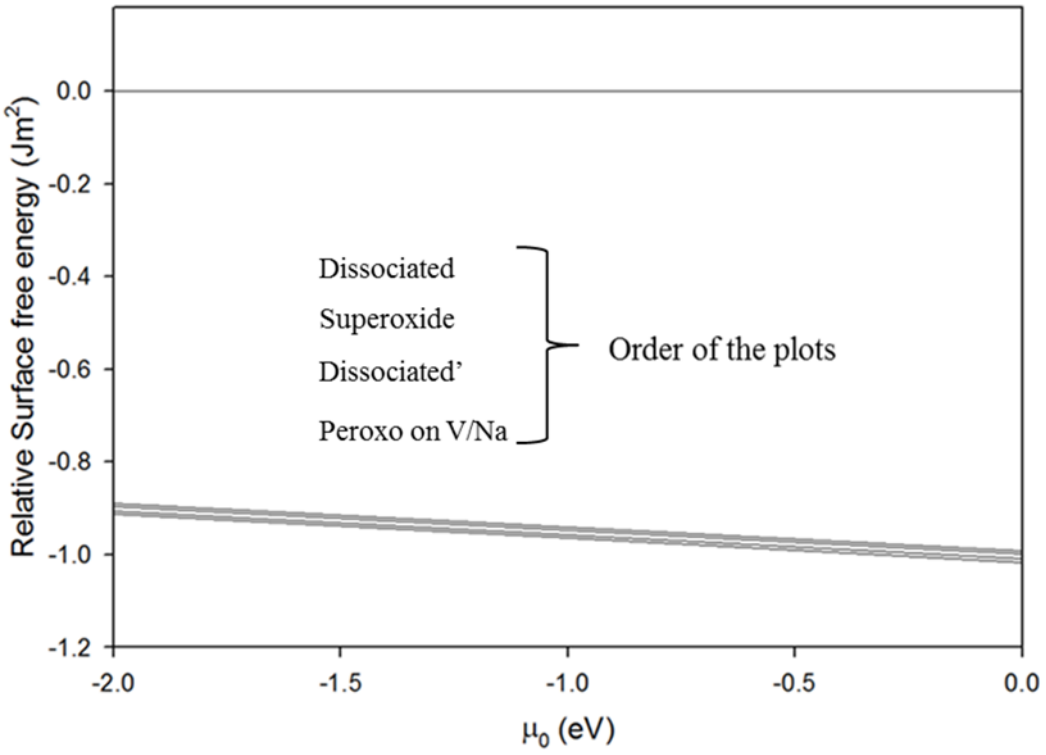

Figure 5.6: Surface free energies of the oxidised Na/VO_2 (110) surfaces with respect to the non-oxidised termination.

The dissociated and peroxo on Ti/Na are the least stable configurations relative to other configurations but still stable compared to pure TiO_2 surface which depicts similar tendencies as the MnO_2.

Oxidation on Na/VO_2 is also stable relative to the Na free surface which is shown in figure 5.5 which extends to -1eV which is 0.9 eV below the threshold of the Na free surfaces. According to the order of the plots it is observed that the most stable configuration is the peroxo on V/Na followed by the dissociated', whereas the superoxide and the dissociated are the least stable configurations.

All plots for different compositions seem to be most stable in all three metal oxides because the relative surface free energies are negative with a very slight increase in

the oxygen chemical potential. The order of stability on the plots is in agreement with the calculated adsorption energies of the oxygen adsorption on the Na-MO_2.

5.4 Effect of MO_2 in the cathode reaction in a Na–air battery

Na−air cells have emerged parallel to the study of Li−air cells an alternative, based on the substitution of lithium by sodium, in spite of their lower theoretical energy density, which can exhibit better reversibility and much lower overpotentials compared to lithium based cells [174,175]. During the battery discharge process, molecular oxygen is reduced in the cathode, in the presence of Na cations and electrons, forming sodium superoxide (NaO_2) particles:

$$O_2 + Na^+ + e^- \rightarrow NaO_2 \quad (5.1)$$

This is subsequently decomposed upon charging in the reverse reaction ($Na^+ + O_2 + e^- \leftrightarrow NaO_2$). Other less prevalent discharge products such as sodium peroxide (Na_2O_2) and peroxide dehydrate ($Na_2O_2 \cdot 2H_2O$) have been reported [176-178]. This is in contrast to nonaqueous Li−air cells, where Li_2O_2 was unequivocally identified as the final discharge.

The effects concerned with the MnO_2 (110) surface as a catalyst are summarized in figure 5.7. Firstly three bulk polymorphs, Fm-3m, marcasite and pyrite, of the Na-O_2 cell superoxide discharge product, NaO_2, are shown in Figure 5.2 and their respective formation energies are -2.14, -2.69 and -2.74 eV [179, 180] with corresponding O-O bond lengths of 3.80, 1.28 and 1.34 Å. A competing discharge product is the peroxo Na_2O_2 (symmetry P-62m) with a formation energy of -2.63 eV and related O-O bond length of 1.49 Å. Furthermore, it is apparent that energies of formation of bulk marcasite (-2.74 eV) and pyrite (-2.69 eV) NaO_2 are lower than adsorption energies of sodium oxides at the MnO_2 (110) surface for all

configurations, i.e. from the least stable (-1.55 eV) to the most stable (-2.18 eV) arrangements. In addition, the energy of the bulk P-62m peroxo Na_2O_2 is also lower than those of all MnO_2 surface catalysed products.

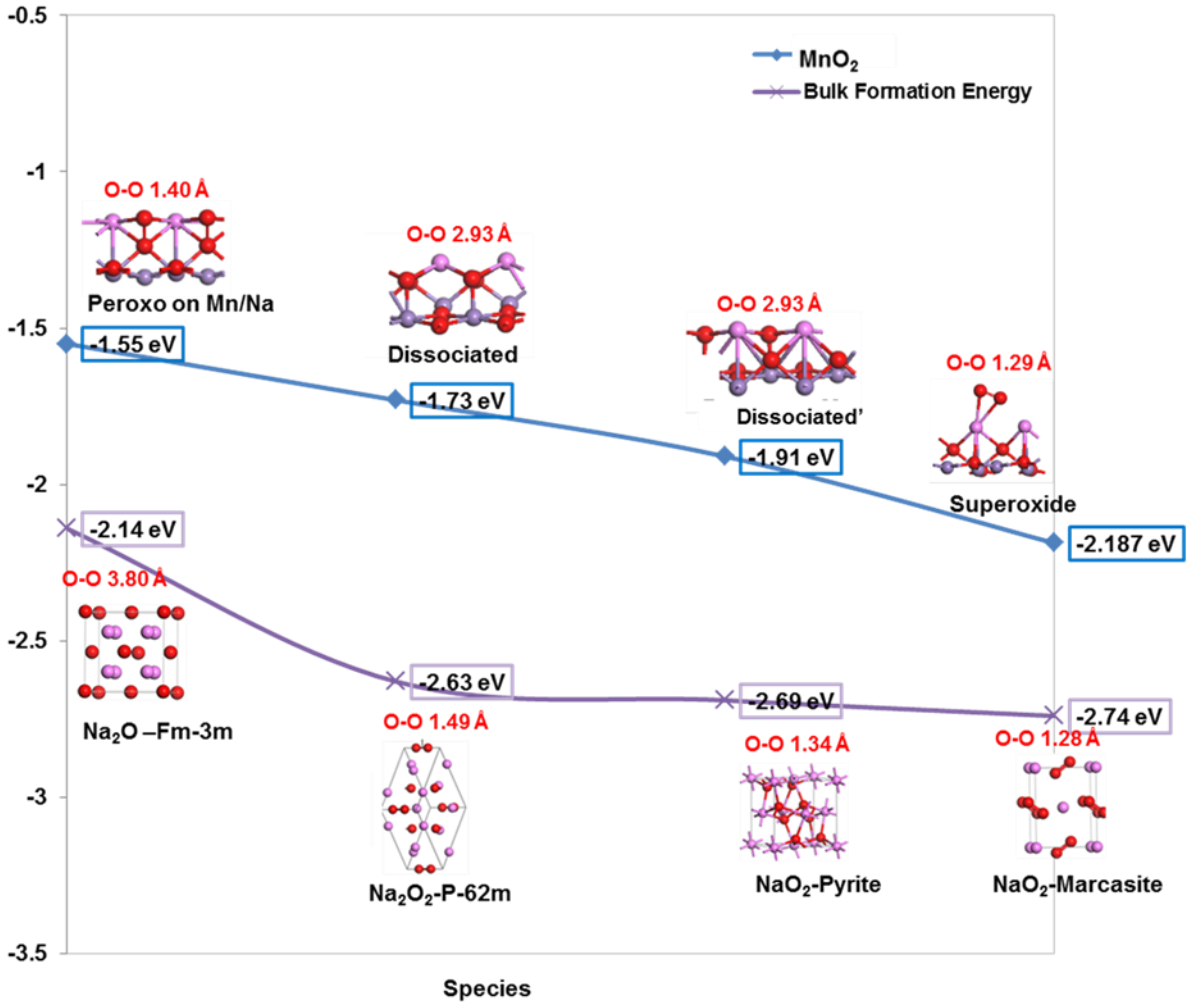

Figure 5.7: MnO_2 surface (110) adsorption and sodium oxide bulk energetics.

This agrees with the experimental observation that NaO_2 is the main product of the cathode reaction in Na–air batteries, accompanied by some Na_2O_2 (both in the presence and in the absence of MnO_2) [174]. Indeed, the O-O bond length of the most stable surface configuration (1.29 Å) is near equivalent to that of the marcasite (1.28 Å) and not adversely far from one of the pyrite (1.34 Å) phase. On the other

hand, the O-O bond length of the least stable configuration (1.40 Å) is 6% smaller to that of the bulk phase of the peroxo Na_2O_2. Formation of dissociated configurations, corresponding to large O-O separations, is also enhanced by the MnO_2 catalyst. All such evidence alludes to the MnO_2 catalyst as promoting nucleation and growth of NaO_2 and Na_2O_2 discharge products.

We now consider the TiO_2 (110) surface as a viable catalyst for the formation of NaO_2 products during discharge. A closer look at the energies of formation of bulk NaO_2 polymorphs and Na_2O_2 figure 5.7 and the energy of formation of the surface sodium oxide at TiO_2 (110) (peroxo on Ti/Na dissociated, dissociated' and superoxide), indicates that the former (bulk) is higher by 0.93eV/Na, 2.29ev/Na, 1.25eV/Na and 0.71eV/Na respectively in all stable configurations for oxygen adsorption on Na-TiO_2 surfaces. This implies that for such configurations, formation of NaO_2 and Na_2O_2 will not be encouraged since the clusters are too stable and would stick to the surface. The initial reduction of oxygen in the cathode occurs less favorably in all configurations i.e. peroxo on Ti/Na, dissociated and superoxide. Although the energetics do not show the benefit of the TiO_2 (110) surface as a catalyst in the formation of expected discharge products, their associated O-O bond lengths are closer to those of Na_2O_2 bulk and dissociated configurations.

Finally, a comparison of the energy of formation of bulk NaO_2 and Na_2O_2, shown in figure 5.9, and the energy of formation of the sodium oxides on VO_2(110) surface (dissociated, dissociated', superoxide and peroxo on V/Na) is informative.

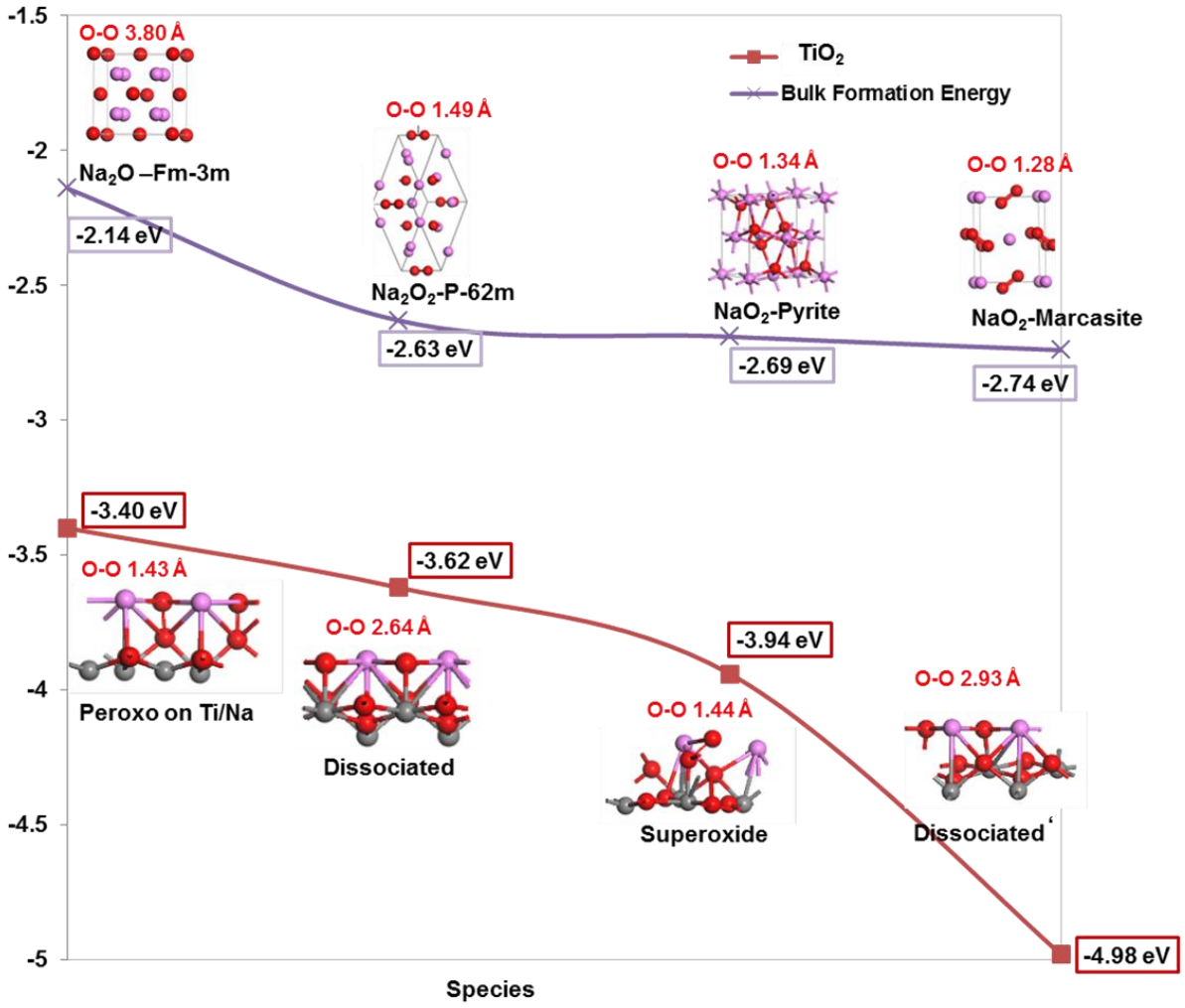

Figure 5.8: TiO_2 surface (110) adsorption and sodium oxide bulk energetics.

It indicates that the energy of formation for the bulk is higher compared to those of all stable sodium oxide configurations induced by the VO_2 (110) surfaces. This suggests that formation of NaO_2 and Na_2O_2 will not be enhanced by VO_2 (110) surface catalyst since the clusters are too stable and would stick to the surface.

Consequently, nucleation and growth of discharge products will not be enhanced by such metal oxide. However, the O-O bond lengths of generated sodium oxides, that are mediated by the catalysts, though not energetically feasible, are closer to those of NaO_2 pyrite (1.36 Å), Na_2O_2 (1.44 Å) and dissociated configurations (3.07 Å).

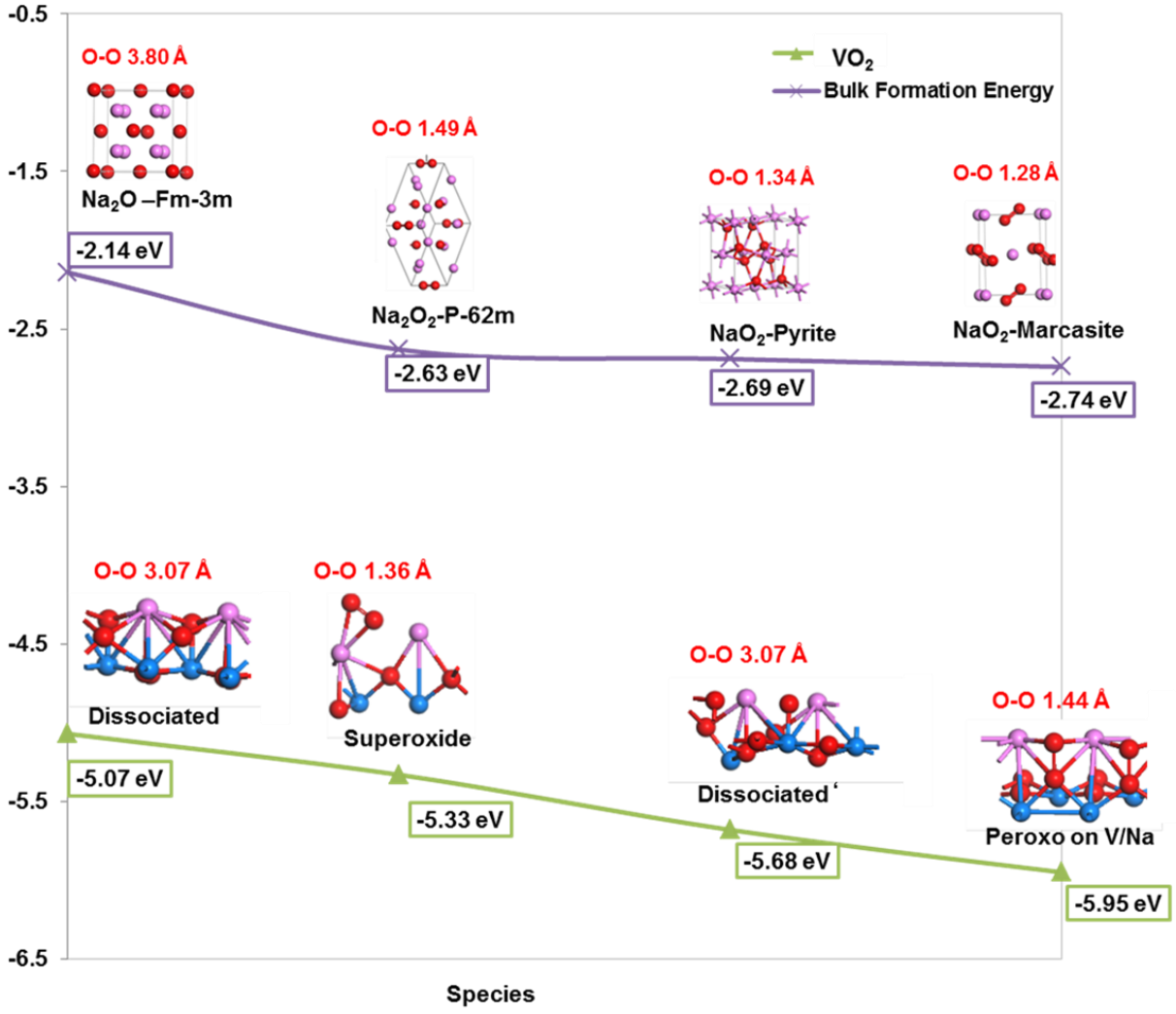

Figure 5.9: VO_2 surface (110) adsorption and sodium oxide bulk energetics

Similarly to rechargeable Li-O_2 batteries, recent studies have alluded to the importance of catalysts in enhancing performance of Na-O_2 batteries. Carbonaceous materials have been used to accelerate the sluggish behaviour of oxygen reduction reaction (ORR) and oxygen evolution reaction (OER) kinetics in rechargeable Na-O_2 [181,182]. Although transition metal oxides catalysts have been employed extensively in Li-O_2 batteries [51-56], owing advantages of low cost, high abundance and environmentally benign considerable catalytic activity in both aqueous and aprotic electrolyte, their use in Na-O_2 batteries is limited.

It has, however, been clearly shown that porous micro-nanostructured $CaMnO_3$ electrode, is an efficient electrocatalyst in Na-O_2 batteries [97], and delivers a high rate capacity and enhanced cyclability. In addition, a composite of $NiCo_2O_4$ nanosheets/Ni foam, as a carbon-free and binder free electrode for Na–air, has been identified as a high efficient electrode for nonaqueous Na–air cells. The nanosheets of the discharge products, composed of Na_2O_2 and Na_2CO_3, were observed after the discharging in sodium–air battery [183]. Similarly, our current study has demonstrated that MnO_2, as a catalyst, promotes nucleation and growth of both Na_2O and Na_2O_2. On the contrary, other metal oxides such as TiO_2 and VO_2 do not depict this catalytic effect towards the formation of discharge products in Na-O_2 batteries.

It is further interesting to discuss the current results in the light of computations reported by Ceder *et al* (2014), which were carried out in the absence of catalysts. They showed that while sodium peroxide (Na_2O_2) is the stable bulk phase of Na in an oxygen environment at standard conditions, sodium superoxide (NaO_2) is considerably more stable at the nanoscale regime. Hence, the superoxide requires much lower nucleation energy than the peroxide, explaining why it can be observed as the discharge product in some Na–O_2 batteries. Our study proposes that the presence of catalysts, such as MnO_2 (110) surface, would further lower the nucleation energy for the superoxides and peroxides, and enhance their growth, whereas the TiO_2 and VO_2 would not be effective.

Chapter 6: Conclusions and Recommendations

6.1 Conclusion

Batteries with new chemistries, often called beyond lithium-ion batteries, have long been proposed to achieve higher energy density and longer cycle life. Metal - air batteries such as Li-air have been extensively studied, owing to their high specific capacity and interest in Na-air is now emerging. The current study is providing a better understanding of the catalytic activity of MnO_2 and similarly rutile typed TiO_2 and VO_2 for the oxygen reduction and oxygen evolution reactions in both Li-air and Na-air batteries, using density functional methods.

The surface calculations, together with all corrections and redox properties for this study were performed using DFT methods within generalized gradient approximation embodied in the VASP code. In view of strong electron correlation in MnO_2 and TiO_2 the Hubbard U parameter was included in all calculations together with the spin polarization. The surface calculations for VO_2 were successfully performed using the generalized gradient approximation (GGA) in the form of the Perdew-Burke-Ernzerhof (PBE) exchange-correlation functional and were not spin polarized.

The equilibrium morphology of MO_2 (R) has been found to be acicular, laterally confined by the (110) planes. When doing surface calculations for the lower Miller indices for the metal oxides, it is found that the most stable surface is the (110) surface, which agrees with experiments.

The main conclusions of our study of the redox behavior of the pure and lithiated (110) surface of rutile-structured MO_2 are as follows:

(a) The stoichiometric MnO_2 (110) surface is very stable under reducing conditions, and can be expected to resist significant reduction under most temperatures and

oxygen partial pressures of interest. The adsorption of oxygen, on the other hand, is relatively favourable at low to ambient temperatures and high partial pressures of oxygen. This adsorption mainly occurs in the form of peroxo species bridging between two surface Mn cations.

TiO_2 (110) surfaces are relatively stable under reducing conditions; the surfaces that form a peroxo group are stable compared to the unstable titanyl group. Adsorption also occurs mainly in the form of the mono-nuclear peroxo species where oxygen bonds with one Ti cation. This configuration also has an angle of 66.2^0, which oxygen molecule prefers to orientate itself on the surface of TiO_2. The oxygen molecule is not adsorbed on the surface TiO_2 but rather floats. The adsorption energies obtained are positive, hence suggesting that the reaction is non-spontaneous and energy is needed for oxygen molecule to adsorb on the surface. For the oxidising conditions, the surfaces are unstable and have a positive vacancy formation.

The VO_2 (110) surface can be expected to be oxidised under ambient conditions, and even under strongly reducing conditions, with excess oxygen forming surface vanadyl groups. Peroxo species are comparatively much less stable. On the other hand, reduction of surfaces is thermodynamically very unfavourable, and oxygen vacancies are in fact easier to form in the bulk than on the surface. VO_2 surface will be stable against oxidation for oxygen chemical potential in the region where bulk VO_2 is stable. However, it is found that much of the surface excess oxygen can actually survive these very reducing conditions.

The major difference between MnO_2 and TiO_2 (110) surfaces is observed in surface free energies as a function of chemical potential, for the most stable oxygen

composition. In the most stable bridging peroxo composition for MnO_2 surface, the graph cuts the zero line for oxygen chemical potential at ~ -0.5 eV. For the mononuclear composition, which is most stable in oxygen adsorption for TiO_2; its graph cuts 0 eV oxygen chemical potential at 0 eV. In the case of the vanadyl composition, which is most stable for VO_2 oxygen adsorption, the graph cuts the zero line of oxygen chemical potential at ~ -1.5 eV

(b) The preferred site for the Li adsorption is one where the adatom is tri-coordinated to one in-plane and two bridging oxygen atoms. Charge transferred from the Li always localizes on the coordinatively unsaturated (5-fold) M (Mn, Ti and V) surface cations, irrespective of the Li adsorption site.

(c) Oxygen adsorption is stabilised by the presence of Li on the surface. The most stable adsorption mode is dissociative, where oxygen atoms saturate the coordination of Mn surface cations, and at the same time bind to the Li adatoms. Adsorption of oxygen on lithiated TiO_2 surface is relatively stable for the dissociated composition but for VO_2 the lithiated surface without oxygen is more stable than that of the oxygen on the lithiated surface. From the surface free energy versus oxygen chemical potential graph, it is clear that MnO_2 is more preferable than TiO_2 and VO_2 in the application for catalyst in Li air batteries. Surface free energies of the different compositions for MnO_2 surface are most stable, TiO_2 is then the least stable and VO_2 surface gives the most unstable surface free energy.

(d) The formation of the surface lithium peroxide is energetically more favourable than the formation of gas-phase lithium peroxide (Li_2O_2) monomers, but less favourable than the formation of Li_2O_2 bulk, which suggests that the presence of β-

MnO_2 in the cathode of a Li air battery lowers the energy for the initial reduction of oxygen.

The formation of lithium peroxide supported by the surface catalyst is energetically more favourable compared to the formation of gas-phase lithium peroxide (Li_2O_2) monomers, but less favourable than the formation of Li_2O_2 bulk in (peroxo on Li and peroxo on Ti/Li), which suggests that the presence of β-TiO_2 in the cathode of a Li air battery lowers the energy for the initial reduction of oxygen.

In the case of VO_2 surface as support, the formation of Li_2O_2 Is energetically more favourable than the formation of gas-phase lithium peroxide (Li_2O_2) monomers, but still more favourable than the formation of Li_2O_2 bulk, which suggests that the presence of β-VO_2 in the cathode of a Li air battery increases the energy for the initial reduction of oxygen which makes VO_2 an undesirable catalyst candidate.

The formation of the surface sodium oxide (NaO_2) is energetically more favourable than the formation of gas-phase sodium superoxide (NaO_2) monomers, but less favourable than the formation of NaO_2 bulk, which suggests that the presence of β-MnO_2 in the cathode of a Na-air battery lowers the energy for the initial reduction of oxygen. In the presence of TiO_2 and VO_2, the formation of the surface NaO_2 is more favourable than the monomer and NaO_2 bulk which implies that the discharge products will stick to the surface.

The stable configurations observed when adsorbing oxygen on Li-MnO_2 encourages the growth of Li_2O_2 which is reported to be the most stable product in Li-air battery. However, the least stable configurations (TiO_2 and VO_2) encourage the formation of other unstable discharge products such as LiO_2 and Li_2O_2. The most stable configuration when adsorbing oxygen on Na-MO_2 was observed as on Na-MnO_2; it

stimulates the growth of NaO_2 which is the most stable discharge product in Na air battery. Other metal oxide (TiO_2 and VO_2) seems to promote formation of both Na_2O_2 which is the least stable discharge product and NaO_2.

Predicted bond O-O lengths provide valuable insights on types of products found in Li-air batteries. The calculated O-O bond lengths of discharge products, particularly the Li_2O_2, mediated by the metal oxide surface catalyst (MnO_2, TiO_2 and VO_2), are near equivalent to those of their bulk and monomer structures. It can also be concluded, from the calculations, that Li_2O_2 is not the only product formed; there is a trace of LiO_2, though less prevalent, which is confirmed by the calculated bond length similar to that of the LiO_2 monomer.

The current calculations have also indicated that the metal oxide catalysts (MnO_2, TiO_2 and VO_2) support the formation of NaO_2 in Na- air batteries, which is the most stable discharge product. This was confirmed by the magnitudes of the O-O bond lengths of some catalyst mediated clusters (NaO_2), which are consistent with those measured experimentally in the bulk NaO_2 polymorphs (such as the pyrite and marcasite) and those of NaO_2 monomer as deduced from calculations. Thus far predicted O-O bond lengths, in the catalyst mediated clusters, that are comparable to Na_2O_2 discharge products are associated with TiO_2 and VO_2 catalysts which tend not to expedite nucleation and growth of all mentioned products.

It can therefore generally be surmised from the current study that MnO_2 catalytic effect is strong in both Li-O_2 and Na-O_2 batteries; TiO_2 is partly valuable for Li-O_2 and dormant for Na-O_2; VO_2 is dormant for both Li-O_2 and Na-O_2 batteries. Generally, adsorption energies of all metal oxide surface mediated discharge products explored in the current study range from -1.55 to -5.96 eV, which is within

acceptable limits of chemisorption processes, where the latter enthalpies of adsorption extend from 80 to 800 kJ/mol, also designated as -0.829 to -8.286 eV. It is also of significance that catalyst metal oxide mediated O-O bond lengths are consistent with those of the bulk and monomer Li_2O_2 (1.55 Å), NaO_2 polymorphs and Na_2O_2 bond lengths, (1.29 – 1.49 Å). Induced bond lengths related to dissociated configurations are depicted by significant oxygen separations, such as 2.9 Å, in both Li-O_2 and Na-O_2 batteries.

6.2 Recommendation

- Carry out calculations on the density of states and the band-structure associated with various adsorptions on oxygen adsorbed surfaces, the metal (Li/Na) on the clean surfaces and the adsorption oxygen on the Li/Na-MO_2.
- The effect of varying the Hubbard U parameter for MnO_2 and TiO_2 will also be explored.
- Furthermore exploration of other metal oxides as catalysts in metal air batteries can be pursued; a study of mixed metal oxides and combinations of metal oxides with precious metals could shed valuable insights.

References

[1] M. Armand and J.M. Tarascon Nature. (2008). *Nature , 451*, 652.

[2] M. Park, H. Sun, H. Lee, J. Lee and J. Cho. (2012). *Adv. Energy Mater. , 2*, 780.

[3] Y.X. Yin, S. X. (2013). *Angew. Chem. Int. Ed , 52*, 13186.

[4] K.D. Rogers. (1993). *Powder Diffr , 8*, 240.

[5] T. Hahn. (1989). *International tables of crystallography, volume A space group symmetry* (Vol. 2nd revised edition).

[6] S.C. Abrahams and J.L. Bernstein. (1971). *J. Chem. Phys. , 55*, 3206.

[7] Y. Murakami, H. Kawada, H. Kawata, M. Tanaka, T. Arima, Y. Moritomo and Y. Tokura. (1998). *Phys. Rev. Lett. 80 , 80*, 1932.

[8] C. Greenwood, N. Norman and A. Earnshaw. (1997). *Chemistry of the Elements.* Oxford.

[9] L.A.H. MacLean and F.L. Tyle. (1996). *J. Solid State Chem. , 123*, 150.

[10] A.R. West, P.B. (1983). *J. Sol. State Chem. , 50*, 235.

[11] M. M. Thackeray. (1997). *Prog. Solid State Chem. , 25*, 1.

[12] Y. Xia, K. Tatsumi, T. Fujieda, P.P. Prosini and T. Sakai. (2000). *J. Electrochem. Soc. , 147*, 2050-2056.

[13] A.R. Bruce and P.G. Armstrong. (1996). *Nature , 381*, 499-500.

[14] F. Cheng, J. Zhao, W. Song, C. Li, H. Ma, J. Chen and P. Shen. (2006). *Inorg. Chem. , 45*, 2038-2044.

[15] F. Jiao and P.G. Bruce. (2007). *Adv. Mater. , 19*, 657.

[16] G.A.E. Oxford and A.M. Chaka. (2011). *J. Phys. Chem. , 115*, 16992.

[17] D.B. Loomer, T.A. Al, L. Weaver and S. Cogswel. (2007). *Am. Mineral , 92*, 72.

[18] Z. Dohnalek, J. Kim, O. Bondarchuk, J.M. White and B. D. Kay. (2006). *J. Phys. Chem. B , 110*, 6229.

[19] M.A. Henderson, W.S. Epling, C.L. Perkins, C.H.F. Peden and U. Diebold. (1999). *J. Phys. Chem. B , 103*, 5328.

[20] D. Pillay and G.S. Hwang. (2006). *J. Chem. Phys. , 125*, 144706.

[21] D. Pillay, Y. Wang and G.S. Hwang. (2006). *J. Am. Chem. Soc. , 128*, 14000.

[22] G. Kimmel and N. Petrik . *Phys. Rev. Lett. , 100*, 196102.

[23] J. Morin. (1959). *Phys. Rev. Lett. , 3*, 34.

[24] R.M. Wentzcovitch, W.W. Schulz, and P.B. Allen. (1994). *Phys. Rev. Lett. , 72*, 3389.

[25] J.M. Tomczak, F. Aryasetiawan, and S. Biermann. (208). *Phys. Rev. B , 78*, 115103.

[26] V. Eyert. (2002). *Ann. Phys. , 11*, 650.

[27] A. Tanaka. (2003). *J. Phys. Soc. Jap. , 72*, 2433.

[28] C.T. Campell. (1997). *Surf. Sci. Rep , 27*, 1.

[29] D.A. Bonnel. (1998). *Prog. Surf. Sci. , 57*, 109.

[30] R.J. Lad. (1995). *Surf. Rev. Lett. , 2*, 109.

[31] S. Chretien and H.J. Metiu. (2008). *Chem. Phys. , 129*, 074705.

[32] K. Kinoshita. (1990). *J. Electrochem. Soc. , 137*, 845.

[33] K.M. Abraham, C. O. Laoire, (2010). *The Electrochem. Society 217th Meeting Abs. 0745* , 1.

[34] C.M. Ó'Laoire. (2010). *Thesis.* Northeastern University, 400 Huntington Avenue Boston, MA 02115, United States.

[35] K.M. Abraham and Z.A.Jiang. (1996). *Electrohemical Sci. Technol. , 143*, 1.

[36] S.S. Zhang, D. Foster and J. Read . (2010). *J. Power Sources , 195*, 1235.

[37] C.O. Laoire, S. Mukerjee, K.M. Abraham, E.J. Plichta and M. Hendrickson. (2009). *J. Phys. Chem. C , 113*, 20127.

[38] T. Ogasawara, A. Débart, M. Holzapfel, P. Novák and P.G.Bruce. (2006). *J. Am. Chem. Soc. , 128*, 1390.

[39] G. Girishkumar, B. McCloskey, A.C. Luntz, S. Swanson and W. Wilcke. (2010). *J. Phys. Chem. Lett. , 1*, 2193.

[40]] J. Yi, K. Liao, C. Zhang, T. Zhang, F. Li and H. Zhou. (2015). *ACS Appl. Mater. Interfac. , 7*, 10823.

[41] W. Zhou, H. Zhang, H. Nie, Y. Ma, Y. Zhang and H. Zhang. (2015). *ACS Appl. Mater. Interfac. , 7*, 3389.

[42] K. Sakaushi, T. Fellinger and M. Antonietti. (2015). *Chem. Sus. Chem. , 8*, 1156.

[43] J. Xie, X. Yao, Q. Cheng, I.P. Madden, P. Dornath, C. Chang, W. Fan and D. Wang. (2015). *Angew. Chem.-Int.Ed. , 54*, 4299.

[44] M. Lee, Y. Hwang, K. Yun and Y. Chung. (2015). *J. Power Sour. , 288*, 296.

[45] E. Yilmaz, C. Yogi, K. Yamanaka, T. Ohta and H.R. Byon. (2013). *Nano Lett. , 13*, 4679.

[46] K. Liao, T. Zhang, Y. Wang, F. Li, Z. Jian, H. Yu and H. Zhou. (2015). *Chem. Sus. Chem. , 8*, 1429.

[47] P. Bhattacharya, E.N. Nasybulin, M.H. Engelhard, L. Kovarik, M.E. Bowden, X.S. Li, D.J. Gaspar, W. Xu and J. Zhang. (2014). *Adv. Funct. Mater. , 24*, 7510.

[48] Y. Lei, J. Lu, X. Luo, T. Wu, P. Du, X. Zhang, Y. Ren, J. Wen, D.J. Miller, J.T. Miller, Y. Sun, J.W. Elam and K. Amine. (2013). *Nano Lett. , 13*, 4183.

[49] C. Xu, B.M. Gallant, P.U. Wunderlich, T. Lohmann and J.R. Greer. (2015). *ACS Nano , 9*, 5876.

[50] J. Zhang, D. Li, Y. Zhu, M. Chen, M. An, P. Yang and P. Wang. (2015). *Electrochim. Acta , 151*, 415.

[51] X. Lin, Y. Shang, L. Li and A. Yu. (2015). *ACS Sustain.Chem. Eng , 3*, 903.

[52] S. Jee, W. Choi, C.H. Ahn, G. Yang, H.K. Cho, J. Lee and C. Yu. (2015). *J. Mater. Chem. A , 3*, 13767.

[53] G. Zhao, Z. Xu and K. Sun. (2013). *J. Mater. Chem. A , 1*, 12862.

[54] H. Geaney and C. O'Dwyer. (2015). *Phys. Chem. Chem. Phys. , 17*, 6748.

[55] X. Hu, F. Cheng, X. Han, T. Zhang and J. Chen. (2015). *Small , 11*, 809.

[56] S. Chen, G. Liu, H. Yadegari, H. Wang and S.Z. Qiao. (2015). *J. Mater. Chem. A , 3*, 2559.

[57]] F. Li, D. Tang, Y. Chen, D. Golberg, H. Kitaura, T. Zhang, A. Yamada and H. Zhou. (2013). *Nano Lett. , 13*, 4702.

[58]] K. Liao, X. Wang, Y. Sun, D. Tang, M. Han, P. He, X. Jiang, T. Zhang and H. Zhou. (2015). *Energy Environ. Sci. , 8*, 1992.

[59] F. Li, D. Tang, Z. Jian, D. Liu, D. Golberg, A. Yamada and H. Zhou. (2014). *Adv. Mater , 26*, 4659.

[60] B.D. McCloskey, R. Scheffler, A. Speidel, D.S. Bethune, R.M. Shelby and A.C. Luntz. (2011). *J. Am. Chem. Soc. , 133*, 18038.

[61] J. Lu, J.B. Park, Y.K. Sun, F. Wu, and K. Amine. (2014). *Chem. Rev. , 114*, 5611.

[62] L.J. Bruce and P.G. Hardwick. (2012). *Current Opin. Sol. State. Mater. Sci. , 16*, 178.

[63] F.S. Gittleson,R.C. Sekol, G. Doubek, M. Linardi and A.D. Taylor. (2014). *Phys. Chem. Chem. Phys. , 16*, 3230.

[64] R. Black, B. Adams and L.F. Nazar. (2012). *Adv. Energy Mater. , 2*, 801.

[65] R. Cao, J.S. Lee, M. Liu and J. Cho. (2012). *Adv. Energy Mater , 2*, 816.

[66] Q. Li, R. Cao, J. Cho, and G. Wu. (2014). *Phys. Chem. Chem. Phys. , 16*, 13568.

[67] W.H. Ryu, F.S. Gittleson, J. Li, X. Tong, and A. D. Taylor. (2013). *Nano. Lett. , 13*, 4190.

[68] X. Lin, Y. Shang, T. Huang and A. Yu. (2014). *Nanoscale , 6*, 9043.

[69] R.S. Kalubarme, C.H. Ahn and C.J. Park. (2013). *Scripta Mater. , 78*, 619.

[70] B.M. Gallant, R.R. Mitchell, D.G. Kwabi, J. Zhou, L. Zuin, C.V. Thompson and Y. Shao-Horn. (2012). *J. Phys. Chem. C , 116*, 20800.

[71] B.D. McCloskey, A. Speidel, R. Scheffler, D.C. Miller, V. Viswanathan, J.S. Hummelshoj, J.K. Norskov and A.C. Luntz. (2012). *J. Phys. Chem. Lett. , 3*, 997.

[72] E.N. Nasybulin, W. Xu, B.L. Mehdi, E. Thomsen, M.H. Engelhard, R.C. Masse, P. Bhattacharya, M. Gu, W. Bennett, Z. Nie, C. Wang, N.D. Browning and J. Zhang. (2014). *ACS Appl. Mater. Interfac. , 6*, 1414.

[73] G. Girishkumar, B. McCloskey, A. C. Luntz, S. Swanson, and W. Wilcke. (2010). *J. Phys. Chem. Lett. , 1*, 2193.

[74] Y. Hu, T. Zhang, F. Cheng, Q. Zhao and X. Han. (2015). *J. Chen, Angew. Chem. Int. Ed. , 54*, 4338.

[75] S. Liu, G. Wang, F. Tu, J. Xie, H.Y. Yang, S. Zhang, T. Zhu, G. Cao and X. Zhao. (2015). *Nanoscale , 7*, 9589.

[76] Z.H. Wei, P. Tan, L. An, T.S.and Zhao. (2014). *Appl. Energy , 130*, 134.

[77] V. Neburchilov,H.J. Wang, J.J. Martin and W.A. Qu. (2010). *J. Power Sources , 195*, 1271.

[78] D. Mei, X. Yuan, Z. Ma, P. Wei, X. Yu, J. Yang and Z. Ma. (2016). *ACS Appl. Mater, Interface , 8 (20)*, 12804.

[79] K. Song, J. Jung, Y. Heo, Y.C. Lee, K. Cho and Y. Kang. (2013). *Phys. Chem. Chem. Phys. , 15*, 20075.

[80] X. Hu, X. Han, Y. Hu and F. Cheng. (2014). *J. Chen, Nanoscale , 6*, 3522.

[81] M. Augustin, O. Yezerska, D. Fenske, I. Bardenhagen, A. Westphal, M. Knipper, T. Plaggenborg, J. Kolny-Olesiak and J. Parisi. (2015). *Electrochem. Acta , 158*, 383.

[82] T.K. Kim, W. Chen and C. Wang. (2011). *J. Power Sources , 196*, 8742.

[83] Y. Xiao, C. Hu, L. Qu, C. Hu and M. Cao. (2013). *European J. , 19*, 14271.

[84] H.S. Jadhav, R.S. Kalubarme, A.H. Jahdav and J.G. Seo. (2014). *J. Electrochem. Soc. , 161*, A2188.

[85] Y. Liang, H. Wang, J. Zhou, Y. Li, J. Wang, T. Regier and H. Dai. (2012). *J. Am. Chem. Soc. , 134*, 3517.

[86] L. Wang, X. Zhao, Y.H. Lu, M.W. Xu, D.W. Zhang, R.S. Ruoff, K.J. Stevenson and J.B. Goodenough. (2011). *J. Electrochem. Soc. , 158*, A1379.

[87] W.M. Liu, T.T Gao, Y. Yang, Q. Sun and Z.W.A. Fu. (2013). *Phys. Chem. Chem. Phys. , 15*, 15806.

[88] H. Wang, Y. Yang, Y. Liang, G. Zheng, Y. Li, Y. Cui and H. Dai. (2012). *Environ. Sci. , 5*, 7931.

[89] B.D. Adams, C. Radtke, R. Black, M.L. Trudeau, K. Zaghib and L. Nazar. (2013). *Energy Environ. Sci. , 6*, 1772.

[90] B.D. McCloskey, D.S. Bethune, R.M. Shelby, G. Girishkumar and A.C. Luntz. (2011). *J. Phys. Chem. Lett. , 2*, 1161.

[91] M.M. Ottakam Thotiyl, S.A. Freunberger, Z. Peng, P.G. Bruce. (2013). *J. Am. Chem. Soc.* , 494.

[92] S.Y. Kang, Y. Mo, S.P. Ong and G. Ceder. (2014). *Nano Lett. , 14*, 1016.

[93] Q. Sun, Y. Yang and Z.W. Fu. (2012). *Electrochem. Commun. , 16*, 22.

[94] W. Liu, Q. Sun, Y. Yang, J.Y. Xie and Z.W. Fu. (2013). *Chem. Commun. , 49*, 1951.

[95] P. Hartmann, C.L. Bender, J. Sann and A.K. Dürr. (2013). *Phys. Chem. Chem. Phys. , 15*, 11672.

[96] B.D. McCloskey, J.G. (2014). *J. Phys. Chem. Lett. , 5*, 12.

[97] Y. Hu, X. Han, Q. Zhao, J. Du, F. Cheng and J. Chen . (2015). *J. Mater. Chem. A , 3*, 3320.

[98] S.N. Altunata and R.W Field. (2003). *Phys. Rev A , 67*, 022507.

[99] M. Mueller,. 1ed. Kluwer Academic. (2002). *Fundamentals of Quantum Chemistry: Molecular Spectroscopy and Modern Electronic Structure Computations* (1 ed.). New York, Boston, Dordrecht, London, Moscow.

[100] P. Hohenberg, and W. Kohn. (1964). *Phys. Rev. , 136* , 871.

[101] R.A. Evarestov. (2007). Quantum Chemistry of Solids, The LCAO First Principles Treatment of Crystals.

[102] http://en.wikipedia.org/wiki/Density_functional_theory. (2011, October 28).

[103] W. Kohn, and L.J. Sham. (1965). *Phys. Rev. , 140*, 1133.

[104] L.J. Sham, and W. Kohn. (1966). *Phys. Rev. , 145*, 561.

[105] D.C. Langreth, and J.P. Perdew. (1975). *Sol. State Comm. , 17*, 1425.

[106] O. Gunnarsson, and B.I. Lundqvist. (1976). *Phys. Rev. B , 13*, 4274.

[107] E. Wimmer, and A.J. Freeman. (2000). *In Electronic Structure (Handbook of Surface Science)* (Vol. 2).

[108] D.J.W. Geldart, and M. Rasolt. (1976). *Phys. Rev. B , 13*, 1477.

[109] G.P. Robert, and Y. Weitao. (1994). *Density-Functional Theory of Atoms and Molecules.* Oxford: Oxford University Press.

[110] P.A.M. Dirac. (1930). *Note on Exchange Phenomena in the Thomas-Fermi Atom* (Vol. 26). Proc. Cambridge Phil. Roy. Soc.

[111] R.M. Dreizler, and E.K.U. Gross. (1990). *Density Functional Theory.* Berlin: Springer-Verlag.

[112] R.G. Parr, and W. Yang . (1989). *Density Functional Theory of Atoms and Molecules.* New York: Oxford.

[113] S.H. Vosko, L. Wilk, and M. Nusair. (1980). *J. Phys. , 58*, 1200.

[114] J.P. Perdew, and A. Zunger. (1981). *Phys. Rev. B , 23*, 5048.

[115] G. Kresse and D. Joubert. (1999). *Phys. Rev. B , 59*, 1758.

[116] J.P. Perdew. (1991). *Phys. Rev. B , 172*, 6.

[117] A. St-Amant, W.D. Cornell, P.A. Kollman, and T.A. Halgren. (1995). *J. Comput. Chem.* , 1483.

[118] J.P. Perdew, J.A. Chevary, S.H. Vosko, K.A. Jackson, M.R. Pederson, D.J. Singh, and C. Fiolhais. (1992). *Phys. Rev. B , 46*, 6671.

[119] K. Burke, J. P. Perdew, and M. Levy, In Modern Density Functional Theory: A Tool for Chemistry, J. M. Seminario and P. Politzer. (1995). *Eds. Elsevier, Amsterdam* .

[120] A.D. Becke. (1988). *Phys. Rev. A , 38*, 3100.

[121] J.P.Perdew. (1986). *Phys. Rev. B , 33*, 8824.

[122] J.P.Perdew, and Y. Wang. (1986). *Phys. Rev. B , 33*, 8800.

[123] J.P. Perdew, P. Ziesche and H. Eschrig. (1991). *In Electronic Structure of Solids.* Berlin: Akademie Verlag.

[124] M.C. Payne, M.P. Teter, D.C. Allan, T.A. Arias, and J.D. Joannopoulos. (1992). *Rev. Mod. Phys. , 64*, 1045.

[125] N.W Ashcroft, and N.D. Mermin, . (1976). *Solid State Physics On Introductory Concepts.* Philadelphia: Saunders College Publishing.

[126] J.S. Blakemore. (1985). *Solid State Physics* (2nd ed ed.). Cambridge: Cambrige University Press.

[127] J. C.Phillips, and L. Kleinman. (1959). *Phys. Rev. , 116*, 287.

[128] M.L. Cohen, and V. Heine. (1970). *Sol. State Phys. , 24*, 37.

[129] H. Hans. (1935). *J. Chem. Phys. , 3* (ISSN 0021-9606), 61.

[130] W.E. Pickett. (1989). *Comp. Phys. Rep. , 9*, 197.

[131] H. Volker. (1970). *The Pseudopotential Concept, Solid State Physics* (Vol. 24). (Academic Press).

[132] D. Brust, and B. Alder. (1968). *The Pseudopotential Method and the Single-Particle Electronic Excitation Spectra of Crystals, Methods in Computational Physics* (Vol. 8). (Academic Press).

[133] W.A. Harrison. (1966). *Pseudopotentials in the Theory of Metals, Frontiers in Physic.* University of Virginia.

[134] Meyer, B. (2006). *Computational Nanoscience , 31*, 71.

[135] D.R. Hamann, M. Schluter, and C. Chiang. (1979). *Phys. Rev. Lett. , 43*, 1494.

[136] P.E. Blöchl. (1994). *Phys. Rev. , 50*, 17953.

[137] D. Vanderbilt. (1990). *Phys. Rev. B , 41*, 7892.

[138] G. Kresse, M. Marsman and J. Furthmuller. (2009). *VASP the GUIDE, Computational Physics.*

[139] G.Kresse and J. Futhmuller. (1996). *Phys. Rev , 54*, 1169.

[140] G. Kresse and J. Furthmuller. (1996). *Comput. Mater. Sci , 6*, 15.

[141] J. P Perdew, K. Burke and M. Ernzwerhof. (1996). *Phys. Rev. Lett. , 77*, 3868.

[142] X. G. Wang, W. Weiss, M. Shaikhutdinov, M. Ritter, F. Petersen, R. Wagner, R. Schlogl, and M. Scheffler. (1998). *Phys. Rev. Lett. , 81*, 1038.

[143] M. W. J. Chase. (1998). *NIST-JANAF Thermochemical Tables* (4th ed ed.). New York: American Institute of Physics.

[144] T. A. Mellan and R. Grau-Crespo. (2012). *J. Chem. Phys. , 137*, 154706.

[145] R. Binions, C. Piccirillo, R. G. Palgrave, and I. P. Parkin. (2008). *Chem. Vap. Deposition , 14*, 33.

[146] H. Perron, C. Domain, J. Roques, R. Drot, E. Simoni and H. Catalette. (2007). *Theor. Chem. Acc. , 117*, 570.

[147] R. R. Maphanga, S.C. Parker and P.E. Ngoepe. (2009). *Surf. Sci. , 603*, 3184.

[148] R. Lindsay, A. Wander, A. Ernst, B. Montanari, G. Thornton, and N.M. Harrison. (2005). *Phys Rev Lett , 94*.

[149] C. Di Valentin, R. Ferullo, Binda, and G. Pacchioni. (2006). *Surf. Sci. , 600*, 1147.

[150] L. Wang, T. Maxisch, and G. Ceder. (2006). *Phys. Rev. B , 73*, 195107.

[151] G.G. Charette and S.N. Flengas. (1968). *J. Electrochem. Soc. , 115*, 796.

[152] J. Stringer. (1965). *J. Less-Common Met. , 8*, 1.

[153] G. L. Humphrey. (1951). *J. Am. Chem. Soc. , 73*, 1590.

[154] B. Tang, G. Wang, L. Zhuo and J. Ge. (2006). *Nanotechnology , 17*, 947.

[155] M. Iwamoto, H. Furukawa, K. Matsukami, T. Takenaka, and S. Kagawa. (1983). *J. Am. Chem. Soc. , 105*, 3719.

[156] P. Scheiber, A. Riss, M. Schmid, P. Varga and U. Diebold. (2010). *Phys. Rev. Lett.* , 105.

[157] A. Vijay, G. Mills, and H. Metiu. (2003). *J. Chem. Phys. , 118*, 6536.

[158] J. Oviedo, M. A. S. Miguel, and J. F. Sanz. (2004). *J. Chem. Phys. , 121*, 7427.

[159] T. P. Kiejna and A. Pabisiak. (2007). *Solid State Commun. , 144*, 324.

[160] D. Pillay and G. S. J. Hwang 2006, 125, 144706. *Chem. Phys. , 125*, 144706.

[161] X. Wu, X.; A. Selloni, M. Lazzeri and S. Nayak. (2003). *Phys. Rev. B , 68*, 241402.

[162] X. Y. Wu, A. Selloni and S. K. J. Nayak . (2004). *Chem. Phys. , 120*, 4512.

[163] A. Tilocca and A. Selloni. (2005). *Chem. Phys. Chem. , 6*, 1911.

[164] S. Tan, S, Y. Ji, Y. Zhao, A. Zhao, B. Wang, J. Yang and J. Hou. (2011). *J. Am. Chem. Soc. , 133*, 2002.

[165] M. M. Branda, N. J.-C. (2009). *J. Chem. Phys. , 131*, 094702.

[166] N. C. Hernandez, R. Grau Crespo, N. H. de Leeuw and J. F. Sanz. (2009). *Phys. Chem. Chem. Phys. , 11*, 5246.

[167] S. Ramchandra, R.S. Kalubarme, S. Harsharaj, Jadhav, D. T. Ngo, G. Park, J.G. Fisher,Y. Choi, W.Ryu and C.J. Park. (2015). *Simple synthesis og highly catalytic carbon-free MnCo2O4 @ Ni as an oxygen electrode for rechargeable Li-O2 batteries with long-term stability.* Nature .

[168] L. G. Cota and P. de la Mora. (2005). *Acta Crystallogr., Sect. B: Struct. Sci. , 61*, 133.

[169] A. Debart, A. J. Paterson, J. Bao and P. G. Bruce,. (2008). *Angew. Chem. , 120*, 4597.

[170] Y. Shao, S. Park, J. Xiao, J.-G. Zhang, Y. Wang and J. Liu. (2012). *ACS Catal. , 2*, 844.

[171] L.Y. Chen, X.W. Guo, J.H. Han, P. Liu, X.D. Xu, A. Hirata, M.W. Chen. (2015). *J. Mater.Chem. A , 3*, 3620.

[172] L. Zou, Y. Jiang, B. Chi and J. Cheng. (2017). *Electrochem Soc Meeting , Abs 514.*, 213.

[173] Z. Ma, X. Yuan, L. Li, Z.-F. Ma, D.P. Wilkinson, L. Zhang and J. Zhang. (2015). *Energy Env Sci. , 8*, 2144.

[174] E. Peled, D. Golodnitsky, H. Mazor, M. Goor and A. Avshalomov. (2011). *J. Power Sources , 196*, 6835.

[175] P. Hartmann, C. L. Bender, M. Vračar, A. K. Dürr, A. Garsuch, J. Janek and P. A. Adelhelm. (2012). *Nat. Mater. , 12*, 228.

[176] Y. Li, H. Yadegari, X. Li, M. N. Banis and X. Sun. (2013). *Chem. Commun.(Cambridge, U.K) , 49*, 11731.

[177] J. Kim, H.-D.Lim, H. Gwon and K. Kang. (2013). *Phys. Chem. Chem. Phys. , 15*, 3623.

[178] Z. Jian,Y. Chen, F. Li, T. Zhang, C. Liu and H. Zhou. (2014). *J. Power Sources , 251*, 466.

[179] W. Liu,Q. Sun,Y. Yang,J. –Y. Xie and Z. –W. Fu. (2013). *Chem. Commun. , 49*, 1951.

[180] S-Y. Kang, Y. Mo, P. Ong and G. Ceder. (2014). *Nano Lett. , 14*, 1016.

[181] Q. Sun, Y. Yang and Z. W. Fu. (2012). *Electrochem. Commun. , 16*, 22.

[182] J. Kim, H. D. (2013). *Phys. Chem. Chem. Phys. , 15*, 3623.

[183] P. Hartmann, M. Heinemann, C. L. Bender, K. Graf, R-P Baumann, P. Adelhelm, C. Heiliger and J. Janek. (2015). *Phys. Chem. C , 119*, 22778.

[184] A. Debart, A. J. Paterson, J. Bao and P. G. Bruce. (2008). *Angew.Chem. , 120*, 4597.

Appendix

Papers presented at conferences

1. K.P Maenetja *et al.*, Oxygen reduction on pyrolusite MnO_2 and rutile TiO_2 (110) surfaces. Presented at the South African Institute Of Physics (SAIP) 55th Annual Conference held at St George Hotel hosted by University Of South Africa (UNISA) on July 2011.
2. K.P Maenetja *et al*., Oxidation of (110) surface of pyrolusite MnO_2 and rutile TiO_2. Presented at the Centre for High Performance Computing (CHPC) Annual Meeting held at the Council of Scientific and Industrial Research (CSIR) on December 2011.
3. K.P Maenetja *et al*., Density functional theory study of (110) β-MnO_2 surface. Presented at the Faculty of Science and Agriculture Postgraduate Research Day held at Bolivia lodge on October 2012.
4. K.P Maenetja *et al*. Redox Properties of (110) β-MnO_2 surface (Catalyst in Li-air Batteries). Presented at the ASSAf Young Scientists Conference held at International convention centre (CSIR), Pretoria on October 2012.
5. K. P Maenetja *et al*. DFT+U study of Li adsorption on (110) β-MnO_2 surface. Presented at the South African Institute of Physics held at Richards Bay hosted by University of Zulu land on July 2013.
6. K.P Maenetja *et al*. Density Functional Theory Study of Lithiated β-MnO_2 (110) Surface used in Li-air batteries. Presented at Bolivia Lodge hosted by University of Limpopo, Faculty of Science and Agriculture on September 2013.

7. K. P Maenetja *et al*. Density Functional Theory Study of Lithiated β-MnO_2 (110) Surface. Presented at the Cape Town International Conversion Centre hosted by CHPC on December 2013.
8. K. P Maenetja *et al*. Computational study of (110) β-TiO_2 surface. Presented at South African Institute of Physics hosted by University of Johannesburg on July 2014.
9. K. P Maenetja *et al*. Redox Properties Study of (110) β-TiO_2 surface. Presented at Bolivia Lodge hosted by University of Limpopo, Faculty of Science and Agriculture on October 2014.
10. K. P Maenetja *et al*. Why MnO_2 is preferred over TiO_2 in Li-air batteries. Presented at Kruger national Park, Mpumalanga hosted by CHPC on December 2014.
11. K. P Maenetja *et al*. Computational study of (110) β-MnO_2 and β-TiO_2 surfaces. Presented at South African Institute of Physics hosted by Nelson Mandela Metropolitan University and co- hosted by Rhodes University on July 2015.
12. K. P Maenetja *et al*. Comparison of β-MnO_2 and β-TiO_2 (110) surfaces as catalysts in li-air batteries. Presented at Bolivia Lodge hosted by University of Limpopo, Faculty of Science and Agriculture on October 2015.
13. K. P Maenetja *et al*. Computer simulation β-MnO_2 and β-TiO_2 (110) surfaces as catalyst in Li-air batteries. Presented at Hyatt Regency Hotel in Rosebank, Johannesburg hosted by DST-Howard university advance-it women in STEM conference on October 2015.
14. K. P Maenetja *et al*. Density functional theory study of stability of rutile MnO_2, TiO_2 and VO_2. Presented at the Centre for High Performance Computing at

the Council for Scientific and Industrial Research (CSIR) hosted by Centre for High Performance Computing (CHPC) on December 2015.

15. K. P Maenetja *et al*. First principle study of stability of rutile MnO_2, TiO_2 and VO_2. Presented at South African Institute of Physics hosted by University of Cape Town on July 2016.
16. K. P Maenetja *et al*. First principle study of the catalyst used in li-air battery. Presented at Bolivia Lodge hosted by University of Limpopo, Faculty of Science and Agriculture on October 2016.
17. K. P Maenetja *et al*. The effect of a catalyst in the cathode reaction in li-air battery. Presented at East London ICC hosted by CHPC, on December 2016.